Multi-layer carbon fibre reinforced plastic characterization and reconstruction using eddy current pulsed thermography

Qiuji Yi

Doctor of Philosophy

School of Electrical and Electronic Engineering

Date of submission:

16/04/2021

This page is intentionally left blank.

CERTIFICATE OF ORIGINALITY

This is to certify that the thesis entitled 'Multi-layer carbon fibre reinforced plastic characterisation and reconstruction using eddy current pulsed thermography' and the work presented has been generated by me as my own original research. I confirm that:

- This work has been done for a research degree at Newcastle University;
- Where I have cited from the work of others, the source is always given;
- I have acknowledged all main sources of help;
- Parts of this work have been published, and these publications are listed in the List of Publication pages. All the relevant papers are properly cited in the thesis.

Qiuji Yi
……………………………………….(Signed)

16/04/2021
……………………………………….(Date)

This page is intentionally left blank

.

Abstract

Carbon fibre composite materials are widely used in high-value, high-profit applications, such as aerospace manufacturing and shipbuilding – due to their low density, high mechanical strength, and flexibility. Existing NDT techniques such as eddy current testing suffers from electrical anisotropy in CFRP (carbon fibre reinforced plastics). Ultrasonic is limited by substantial attenuation of signal caused by the multi-layer structure. The eddy current pulsed thermography has previously been applied for composites NDE (non-destructive evaluation)such as impact damage, which has the ability for quick and accurate QNDE(quantitative non-destructive evaluation) inspection but can be challenging for detection and evaluation of sub-surface defects, e.g., delamination and debonding in multiple layer structures. Developing QNDE solutions using eddy current thermography for addressing subsurface defects evaluation in multi-layer and anisotropic CFRP is urgently required.

This thesis proposes the application of eddy current pulsed thermography (ECPT) and ECPuCT (eddy current pulse compression thermography) for tackling the challenges of anisotropic properties and the multi-layer structure of CFRP using feature-based and reconstruction-based QNDE and material characterisation. The major merit for eddy current heating CFRP is the volumetric heating nature enabling subsurface defect detectability. Therefore, the thesis proposes the investigation of different ECPT and their features for QNDE of various defects, including delamination and debonding.

Based on the proposed systems and QNDE approach, three case studies are implemented for <u>delamination QNDE</u>, <u>debonding QNDE</u>, <u>conductivity estimation and orientation inverse reconstruction</u> using the two different ECPT systems and features, e.g., **a pulse compression approach to increase the capability of the current ECPT system**, **the feature-based QNDE approach for defect detection and quantification**, and **reconstruction-based approach for conductivity estimation and inversion.** The three case studies include 1) investigation of delamination with different depths in terms of delamination location, and depth quantification using K-PCA, proposed temporal feature-crossing point feature and ECPuCT system; 2) investigation of debonding with different electrical and thermal properties in terms of non-uniform heating pattern removal and properties QNDE using PLS approaches, impulse response based features

and ECPuCT system; 3) investigation of electrical and conductivity estimation, layer orientation reconstruction using ECPT system and designed reconstruction algorithms.

The significant contributions of the thesis are concluded as follows: 1) the use of pulse compression approach for eddy current pulsed thermography system by modulating the excitation signal to increase the SNR of transient response, leading to the world's first ECPuCT system; 2) proposal and systematic investigation of new features for the impulse response of ECPuCT system including the crossing point for quantifying the defect depth, which is related with the time of flight of thermal wave, kernel PCA which is capable of extracting defective signature for the location of the defect, 3) proposal of two-step inversion approach for parameter estimation and reconstruction as a complementary approach for global parameters QNDE. Step 1: electrical, thermal conductivity estimation using different stages of transient response. Step 2: layer orientation inversion reconstruction approach for multi-layer CFRP.

The thesis concludes that the proposed pulse compression approach enables the subsurface defect detectability of delamination with various depths and debonding with different electrical and thermal properties. The feature-based K-PCA and PLST approaches can well extract the defect transient and spatial pattern in the impulse response of ECPuCT in terms of defect location. The temporal features of the impulse response, including crossing point and impulse response's derivatives, can illustrate the time of flight of thermal wave and the multi-physics interaction between Joule heating and thermal diffusion for depth QNDE. The forward reconstruction-based calculations of FEM can help estimate the electrical and thermal conductivity of CFRP and reconstruct layer information at different depths. It is found that the feature-based approach is computationally inexpensive but less accurate, while reconstruction approaches can provide more accurate QNDE but require more effort. These two proposed QNDE approaches are complementary in terms of local defect QNDE and global parameters QNDE.

In the future, the current work can be improved by developing the framework of multiple features' selection, fusion, and decision making for QNDE of CFRP under complex scenarios and reconstructing the defective profile in the multi-layer structure..

Acknowledgements

I would like to send my sincere gratitude to my supervisors, Professor Gui Yun Tian and Dr. Rajesh Tiwari, for their patient guidance and support for my PhD work. Professor Gui Yun Tian, who leads me into the field of electromagnetic non-destructive testing and evaluation, faithfully guided and trained me to be a professional academic researcher. We spend lots of time brainstorming ideas, discussing the outcome of my work, and outlining the future path when the work is finished. Without three years' training and guidance, the completion of my PhD study would not have been possible.

Thanks also go to all the group members, Dr. Junzhen Zhu, Dr Kongjing Li, Dr Ruslee Sutthaweekul, Dr. Chaoqing Tang, Dr. Xiaotian Chen, Dr. Denis Ona, Mr. Yachao, Ran, Mr. Adi Marindra and Mr Lawal Daura. Also, thanks to research colleagues in the NDTonAIR project, Dr. Hamed Malekmohammadi, Dr Stefano Stefano Laureti, and Mr. Abdoulaye Ba. I am grateful for the suggestion and help from all the academics as follows, Professor Marco Ricci, Professor Bin Gao, Professor Feng Liu, Dr Shang Gao, Professor Yifei Gao. I extend my appreciation to all the staff and technicians, especially Mr Paul Killan, from Newcastle University, for their professional support.

Ultimately, I voice a special note of gratitude to my wife, Jing Chu, and my parents. Their love, encouragement, and support have been far more significant than I can now express in words.

List of Publications

Journal Papers

1. **Yi Q**, Tian G, Malekmohammadi H, Zhu J, Laureti S, Ricci M. New features for delamination depth evaluation in carbon fibre reinforced plastic materials using eddy current pulse-compression thermography. NDT & E International. 2019;102:264-73.

2. **Yi Q**, Tian G, Yilmaz B, Malekmohammadi H, Laureti S, Ricci M, et al. Evaluation of debonding in CFRP-epoxy adhesive single-lap joints using eddy current pulse-compression thermography. Composites Part B: Engineering. 2019;178:107461.

3. **Yi Q**, Malekmohammadi H, Tian GY, Laureti S, Ricci M. Quantitative Evaluation of Crack Depths on Thin Aluminum Plate Using Eddy Current Pulse-Compression Thermography. IEEE Transactions on Industrial Informatics. 2019;16:3963-73.

4. **Yi Q**, Tian GY, Laureti S, Ricci M. Inverse reconstruction of fibre orientation in Multilayer CFRP using forward FEM and eddy current pulsed thermography(NDT&E international: minor revision).

5. X. Lu, **Q. Yi*** and G. Y. Tian, "A comparison of feature extraction techniques for delamination of CFRP using Eddy current pulse-compression thermography," in IEEE Sensors Journal, doi: 10.1109/JSEN.2020.2993154.(corresponding author)

Conference Papers

1. **Yi Q**, Tian G, Chebbi H, Prémel D. Investigation of layer interface model of multi-layer structure using semi-analytical and FEM analysis for eddy current pulsed thermography. 2020 IEEE International Instrumentation and Measurement Technology Conference (I2MTC): IEEE; 2020. p. 1-5.

2. **Yi Q**, Marindra AMJ, Zhu J, Ba A. Detection of Unknown Defects in CFRP Using Eddy Current Pulsed Thermography and Microwave NDT. 2019.

3. **Yi Q**, Tian G, Zhu J, Laureti S, Malekmohammadi H, Ricci M. Quantitative evaluation of delamination depth in CFRP based on pulse compression eddy current pulse thermography.

4. Malekmohammadi H, Laureti S, Ricci M, **Yi Q**, Zhu J, Tian GY. An Experimental Comparison of LED and Eddy Current Pulse-Compression Thermography on an Impact Damage CFRP Benchmark Sample. 2018 IEEE Far East NDT New Technology & Application Forum (FENDT): IEEE; 2018. p. 13-7.
5. Ba A, Bui H-K, Berthiau G, **Yi Q**, Zhu J, Tian GY. Eddy-Current Pulsed Thermography for the Detection of Impact Damage on CFRP. 2019.

Table of contents

Abbreviations

AE	Acoustic Emission
APST	Absolute Peak Slope Time
AT	Active Thermography
ANN	Artificial Neural Network
BVID	Barely Invisible Impact Damage
CFRP	Carbon Fibre Reinforced Plastics
CT	Computed Tomography
ECPT	Eddy Current Pulsed Thermography
ECPuCT	Eddy Current Pulse Compression Thermography
FBH	Flat Bottom Hole
FEM	Finite Element Modelling
HOS	High Order Statistics
ICA	Independent Component Analysis
IRT	Infrared Thermography
K-PCA	Kernel Principal Component Analysis
LITP	Lock-in Thermographic Phase
LST	Laser Thermography Testing
MORWG	Microwave Open-Ended Wave Guide
NDT&E	Non-destructive Testing and Evaluation
OT	Optical Thermography
PLS	Partial Least Square
PuC	Pulse Compression
PCA	Principal Component Analysis

QNDE	Quantitative Non-destructive Evaluation
ROI	Region of Interest
RTM	Resin Transfer Moulding
SNR	Signal Noise Ratio
SUT	Sample Under Test
SVD	Singular Value Decomposition
TCA	Thermographic Cluster Analysis
TSR	Thermographic Signal Reconstruction
VI	Visual Inspection

List of Figures

List of Tables

Chapter 1 Introduction

In this chapter, the background of electromagnetic non-destructive testing for multi-layer CFRP is presented. The challenges and motivation of developing eddy current pulse thermography and pulse compression thermography for quantitative evaluation of CFRP are illustrated. The aim and objectives of the study are addressed based on the identified challenges. Additionally, the overall methodology of eddy current pulsed thermography and the framework of the feature-based and model-based QNDE approach is briefly introduced. The arrangement of each chapter is also given at the end.

1.1 Background

Carbon fibre reinforced plastics (CFRP) materials have become increasingly popular among conventional well studied engineered materials due to advanced properties that they present: high strength to weight ratio, resistance to corrosion, thermal expansion, and fatigue[1, 2]. The above characteristics have led to the large increase of industrial applications of such composites to the development of wind turbines, aircraft fuselage, and sports equipment. However, Due to the lack of appropriate NDT&E applications of CFRP when it began to be massively produced and used in the early 21st century, the undetected defects of aerospace components pose a threat to aircraft structural integrity. Unlike aircraft made of metal, load capabilities, damage tolerance, and reparability of composites made aircraft are not thoroughly investigated in terms of different NDT&E techniques. Therefore, investigating the defects by non-destructive testing is crucial to improve the durability, reliability of new generation aeroplanes.

The massive applications of composites of aeroplanes in the industry such as Boeing 787 promote the need for fast, straightforward visualisation of structural information in the components. Besides, the characterisation of fibre orientation which affects the compressive strength is urgently required for composites laminates during the manufacturing process. The defect detection includes the location and sizing of delamination, and debonding is also one of the critical requirement. Based on the requirement, a significant number of NDT&E techniques are used in the composite NDT field, including electromagnetic testing such as eddy current, magnetic flux leakage, microwave NDT, passive and active thermography testing and ultrasound testing such as phased array and guided wave[3].

In recent years, the multi-physics based eddy current pulsed thermography imaging technique was proposed. By combing the detection and evaluation of electromagnetic, thermal field/waves in one single test, the detecting sensibility/efficiency is increased compared with traditional NDT&E. Compared with conventional eddy current testing or active thermography testing, one significant benefit of utilizing an eddy current as a heating source is the volumetric nature for composites due to its low electrical conductivity. Thus, the failures and defects inside the structure can be interacted directed directly with the eddy current, which increases the sensitivity and detectability for the subsurface defect. All these benefits of ECPT for composites NDT&E enables it the potential as an excellent quantitative non-destructive testing approach for CFRP.

Thus, by the proposed techniques, the thesis has developed and investigated a framework including using pulse compression for increasing its detectability and sensitivity, which has been validated on benchmark sample, proposing a feature-based QNDE approach for defect location and quantification, and proposing a reconstruction-based inversion approach, which plays an essential role for multi-parameter defect evaluation.

1.2 NDTonAIR project

My PhD study is funded under the action: H2020-MSCA-ITN-2016-GRANT 722134[4]. The project from Innovative Training Network aims to train the future generation of scientists with the background of theoretical and experimental skills, capable of developing their research and entrepreneurial activities in the field of NDT and SHM

The "NDTonAIR" project has 15 early-stage researchers (ESRs) for NDT&E, SHM of aerospace components, which include eddy current, phased array, guided wave, thermography for inspection of the structural integrity of aircraft. The ESR 7(the author) researches the sub-project multiple layer composite modelling and characterisation using pulsed eddy current and eddy current pulsed thermography at Newcastle University.

In this project, the ESRs have the opportunity to join the training event every three months for understanding the state-of-art of NDT and SHM for composites and discussing each other's progress for possible collaboration within the network. Additionally, the ESRs can travel and visit in the secondment period in other institutes for using the equipment and benchmark samples. With this opportunity, different techniques, including experimental system and processing algorithms, can be validated by different groups in the consortium, which effectively and efficiently promotes the development of NDT&E of CFRP. The network provides an excellent chance for PhD students to start their academic careers.

1.3 Aim and Objectives

The eddy current pulsed thermography is promising due to its multi-physics volumetric heating nature, and the broad application of composites leads to the urgent need for NDT&E of the material. However, the anisotropy in the multi-layer structure presents challenges in simulation/experiment/QNDE, which hinders the application of ECPT in terms of QNDE. To tackle with these challenges, this project aims at:

- Undertaking the review of state of the art NDT&E techniques including ultrasound, active thermography, microwave opened waveguide, eddy current, and eddy current pulsed thermography for NDT&E of CFRP. (Review)
- Designing and implementing eddy current pulse compression to thermography to improve the sensitivity and detectability of the ECPT system and preparing the benchmark samples through networking by communicating with the consortium under the NDTonAIR project. (System and Sample)
- Designing the feature extraction approach method for addressing the challenges of non-uniform heating pattern and depth quantification in the ECPT and ECPuCT system. (Feature-based QNDE)
- Designing and developing a reconstruction-based inversion approach for CFRP electrical and thermal conductivity estimation and parameter inversion. (Reconstruction-based QNDE)
- Investigating the proposed ECPuCT system and feature-based approach for debonding and delamination QNDE in multi-layer CFRP (Case study)
- Investigating the proposed reconstruction approach on unidirectional CFRP for estimating the conductivity and reconstructing the layer orientation (Case study)

1.4 Overall Research Methodology

To achieve the aims mentioned above, the work implements the strategy from numerical modelling, experiment, and post-processing techniques, including the feature-based and model-based approach to tackle the challenges of multi-layer, multi-physics, and anisotropy issue of CFRP, of which the process is shown in Figure 1-1

The numerical modelling approach involves the 3-D induction heating simulation model of a multi-layer anisotropic composite material. The real geometry of multi-layer composite materials with an equivalent anisotropic individual layer is considered. A global equivalent model is then introduced to consider the different fibres' orientations. The model is established to investigate the electromagnetic and thermal behaviour of multi-layer CFRP influenced by fibre orientation.

In order to improve the detectability of the ECPT system and cope with this problem of signal-to-noise ratio, this thesis proposes the eddy current pulse-compression thermography (ECPuCT), combining the Barker code modulated eddy current excitation and pulse-compression technique to enhance the capability of characterising defects on carbon fibre reinforced plastic materials.

Based on the model and system proposed above, the development of post-processing techniques includes feature-based and model-based techniques. The feature-based approach includes Kernel Principal Component analysis proposed for defect pattern enhancement and location, PLS(partial least squares), which is used for minimizing the non-uniform heating pattern of thermal images, skewness which is used to quantify the transient impulse response for defect depth QNDE. However, feature-based approaches have limitations when a multi-parameter requirement is required or there is a limited number of samples for calibration of the relationship between features and defect parameters. As for the model-based approach, the comprehensive profile reconstruction of CFRP properties in terms of conductivity tensor and fibre orientation is implemented by optimisation between the forward model and experimental data.

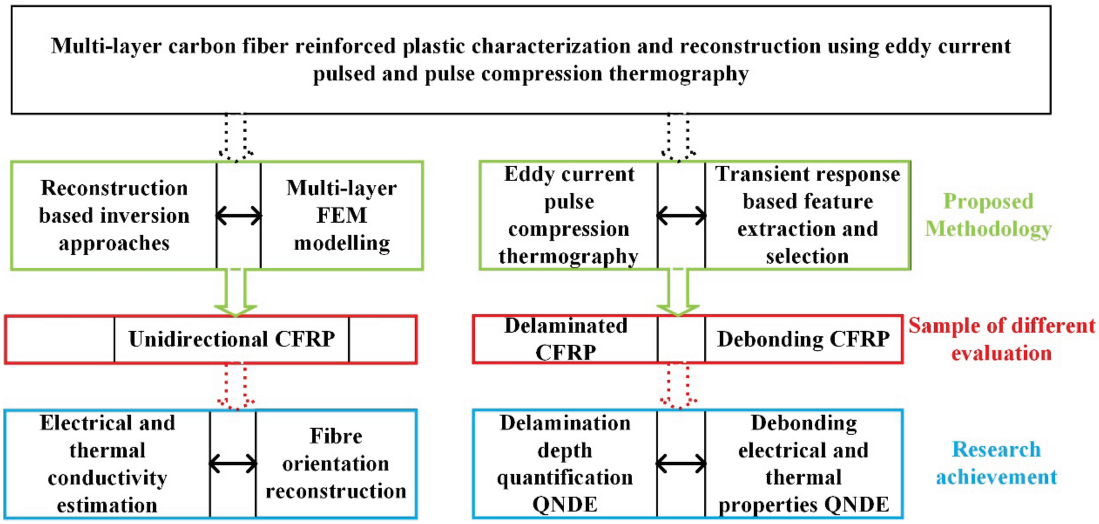

Figure 1-1 Diagram of the overall system

1.6 Thesis layout

In this thesis, the introduction of the background and the general arrangement of the thesis is presented in chapter 1.

Chapter 2 reviews the state-of-art of electromagnetic non-destructive testing for CFRP, including the pros and cons of each technique, especially the progress and current research gaps of eddy current stimulated thermography for CFRP NDT&E.

Chapter 3 introduces the theoretical background, including the multi-physics theory of the ECPT system for CFRP, the finite element modelling of the multi-layer structure, the pulse compression setup for the ECPT system, as well as feature extraction techniques used in this work.

Chapter 4 presents the feature-based case study of CFRP delamination depth QNDE, where the pulse compression technique is used to improve the SNR of transient response, kernel principal component analysis is applied for the location of the defect and crossing point feature as well as skewness feature are proposed for the depth quantification.

Chapter 5 presents the feature-based case study of CFRP debonding, where inclusions of different electrical and thermal properties at the same depth are quantified using sliding K-PCA and spatial kurtosis approach.

Chapter 6 introduces the model-based case study for CFRP electrical and thermal conductivity estimation and fibre orientation reconstruction using optimisation between forward calculation and experimental data. The model-based approach is validated and compared with a feature-based random transform technique.

Chapter 7 summarizes the conclusion of CFRP QNDE using feature-based and model-based techniques and presents the vision of future work.

1.7 Chapter summary

This chapter briefly introduces the background of electromagnetic non-destructive testing for CFRP. Additionally, the challenges and motivation of developing and improving eddy current pulse thermography by pulse compression, FEM modelling, feature-based approach, and model-based approach are illustrated. The aim and objectives of the study are addressed. The overall methodology of eddy current pulsed thermography and the framework of the feature-based and model-based QNDE approach is briefly introduced in Figure 1-1.

The next chapter reviews the state-of-art of electromagnetic non-destructive testing for composites, especially multi-layer CFRP.

Chapter 2 Literature review

There exists a wide range of NDT&E techniques for QNDE of CFRP. The traditional NDT methods, including eddy current, magnetic flux leakage, microwave NDT, passive and active thermography testing and ultrasound testing such as phased array and guided wave, each have their pros and cons. In this chapter, to have a comprehensive understanding of the state-of-art for composites and identify the challenges of these techniques, chapter 2 introduces the current application in aerospace in section 2.1. CFRP defects and the challenges for them to be detected are introduced in section 2.2. The electromagnetic NDT&E techniques, as well as their limitations, are identified in section 2.3. Section 2.4 summarises the challenges of current NDT&E techniques.

2.1 CFRPs and the applications in aerospace

The carbon fibre reinforced polymer (CFRPs) are used mostly in various applications in the aerospace industry[5, 6]. In the aerospace industry, due to the outstanding properties of CFRP, such as high-strength-ratio and the reasonable resistance for corrosion, fatigue and thermal, CFRPs are widely used, and it is worth noting that a gradual replacement of metal components by the development of CFRPs has increased in recent years [7].

Generally, the CFRPs are used extensively in wings, fuselage sections (such as the undercarriage and rear end of fuselage), tail surfaces, and doors[8-10]. For instance, Airbus 320 consists of components made from CFRPs for enhancing the structural integrity of its fin and tailplane, which results in 800 kg weight saving compared to the equivalent in aluminium. Another example is that the A380's airframe consists of more than 20% CFRPs usage. The latest example is the Boeing 787, which utilizes much greater use of CFRPs usage than any commercial aeroplane. The half airframe of Boeing 787 is formed by carbon fibre reinforced plastic and other composites, which leads to weight savings on average of 20% compared to aluminium aircraft [11].

Besides the weight-saving advantage of CFRP formed structure, they also have the following merits:

1) The structures can be moulded to deliver higher strength at a much lower weight, which is crucial for the commercial aeroplane.

2) The mechanical properties to enhance the strength to a certain direction can be designed by tailoring 'lay-up' design in terms of changing tapering thicknesses of reinforcing and fibre orientation.

3) The material of carbon fibre and epoxy leads to outstanding thermal stability, which is important the ensure the security of aircraft since the variation of altitude leads to a drastic change in temperature.

4) The issue of fatigue/corrosion problems happened a lot in metal structures are minimized

2.2 Defects in CFRPs

According to the merits mentioned in section 2.1, the aerospace industry regards the CFRPs as the main material for modern civilian and military aircraft. However, the manufacturing procedures, including compression moulding, liquid moulding, injection moulding [12], as well as the operation in a harsh environment, can generate defects in the matrix, fibre, and interface, which heavily reduces the mechanical properties of in-service aerospace structures, and if left without detection can cause catastrophic failure. In this section, different defects of CFRPs are introduced for highlighting the challenges of applying NDT&E for QNDE.

2.2.1 Fibre defects

In CFRPs, the fibre defects refer to fibre misalignment, waviness, and broken fibres. The deviations caused by misalignment and waviness can reduce mechanical properties, specifically the compression strength and stiffness, which result in reductions in limit load and ultimate load capability during its service [13]. The effect of fibre waviness in unidirectional CFRPs, where fibres have the same direction in the sample, showed that the stiffness and strength reduced drastically due to fibre waviness under axial compression[14]. According to Ref. [15], the misalignment of fibre waviness with 15° can cause a 50% reduction of compressive strength in the multi-layer structure. A study has been conducted in terms of stress analysis in experimental indicated that the interlaminar shear stress caused by fibre waviness is responsible for delamination and subsequent failure, such as debonding, which is shown in Figure 2-1 [16]. The fibre defects can be characterised by various NDT&Es. X-ray is one of the effective methods for fibre defects, such as fibre waviness detection. Multiple filed images have been extracted to characterise the fibre orientation by using CT images[17]. The UT methods, using TEM (total focusing method)and air couple ultrasound for detecting the in-plane waviness of CFRP[18]. The UT methods can be challenging due to the attenuation of the signal caused by the multi-layer structure. The eddy current testing, as an alternative approach, can provide non-contact measurement, can be applied for characterising the subsurface fibre distribution using high frequency ranging to 10 MHz[19]. However, this ECT based NDT can suffer from the electrical anisotropy of the material, which reduces its capability.

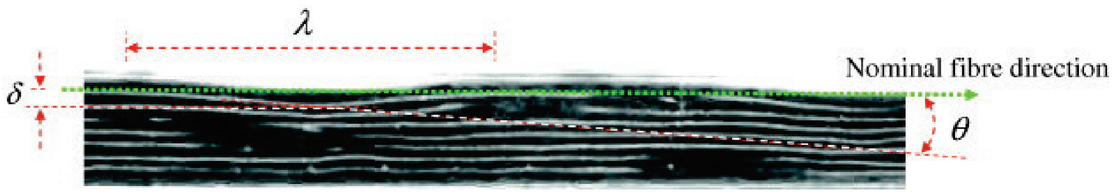

Figure 2-1 out-of-plane waviness in a Resin Transfer Moulding (RTM) [16]

2.2.2 Delamination

Delamination is the most common defects in CFRPs., shown in Figure 2-2, which can propagate throughout the composite structure during its service under repeated loading, causing failure of the whole structure if left undetected[20]. The delamination usually initiates and grows between the different plies of composite material at the layer interface, causing reductions in in-plane strength and stiffness. In previous research, delamination failures are characterised as three different modes: opening (Mode I); tearing-shear (Mode II); or sliding-shear(Mode III). In this thesis, delamination serves as one case study for the proposed eddy current pulse compression system for evaluating the system's depth quantification ability using the proposed crossing point feature.

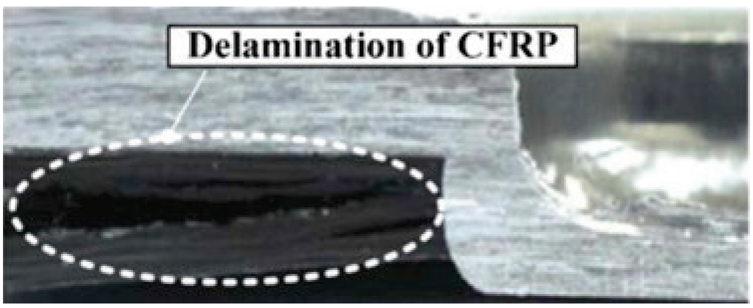

Figure 2-2 Delamination in a composite material[21]

2.2.3 Debonding

Debonding is defined as the loss of adhesion between reinforcement (particle or fibre) and matrix. In CFRP specifically, debonding refers to the phenomenon that no adhesive force is adhering to an adherend or substrate layer at the bonded line or interfaces in the CFRP structure[22]. Debonding happens if the physical, chemical or mechanical forces that hold the bond together are broken, especially during manufacturing [23]. The difference between debonding and delamination is that the delamination can cause separation of the layers of the laminate, while debonding refers to the adhering force at the bonding interface breaks down, which can be challenging to be detected by ultrasound NDT[24]. The difference is highlighted in Figure *2-3*. In this thesis, the debonding serves as one case study for evaluating and validating the proposed system's ability for multi-physics quantification in terms of electrical and thermal conductivity.

Figure 2-3 CFRP debonding

2.2.4 Impact damage

Impact damage can happen when dropped tools, hard landings, hail, bird strikes, and stone impacts on take-off, landing to the CFRP structure[25]. Subsurface damage caused by different impact mentioned above is known as barely visible impact damage (BVID)[26]. Subsurface BVID can cause multiple failures such as delamination[27], fibre rupture [28] also internal matrix crack. The impact damage can be left without detected for long periods, which can lead to catastrophic failure when the defects propagate to the whole structure. The eddy current pulsed thermography has been applied for the evaluation of BVID in [29], of which the results 10 J BVID are shown in Figure 2-4 and Figure 2-5.

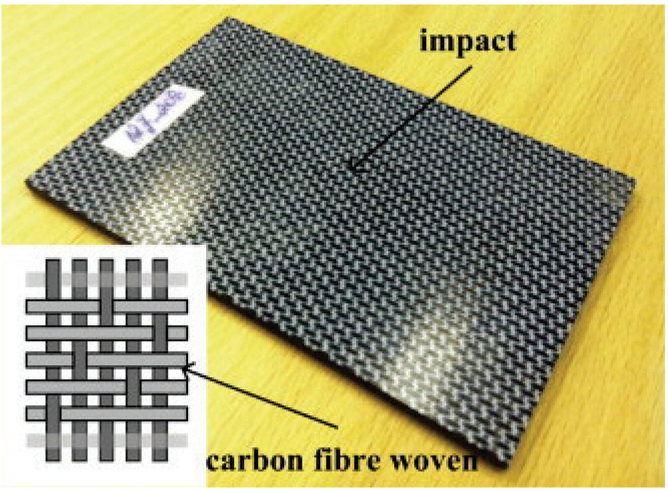

Figure 2-4 Barevely invisible impact damage[29]

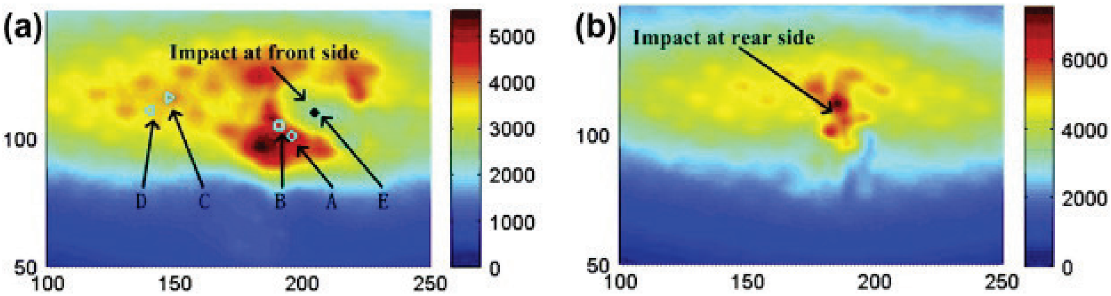

Figure 2-5 Thermal images of 10J BVID detected by ECPT[29]

2.2.5 Damage evolution of defects in CFRP

The damage and failures are not separated in the life cycle of CFRP structure, of which the damage evolution scenario during a lifetime can be categorized and composed of three main stages [30] shown in Figure 2-6. The categorized strategy is based on the material's normalized stiffness evolution kinetics[31]. The first stage is developed during the first 5% of the structure's serving life and is featured by a rapid decrease in the stiffness, of which the failures can be matrix cracks and debonding in the fibre scale. The second stage is a steady process with a slower damage evolution, of which the failures can be debonding and delamination in the ply scale. The third stage is featured by prompt reduction of normalized stiffness leading to failure and breaking down of the structure, which can be cracked through multiple plies [32].

Based on the literature review of defects in CFRP, the next few sections in Chapter II aim to conduct a thorough investigation of NDT&E for multi-layer CFRP, including ultrasonic testing, thermographic testing, infrared thermography testing, electromagnetic testing and so on[13]. Next few sections reviews NDT methods for composite evaluation, followed by categorizing them and discussing their advantages and disadvantages in order to understand the state-of-art applications and identify challenges in this field.

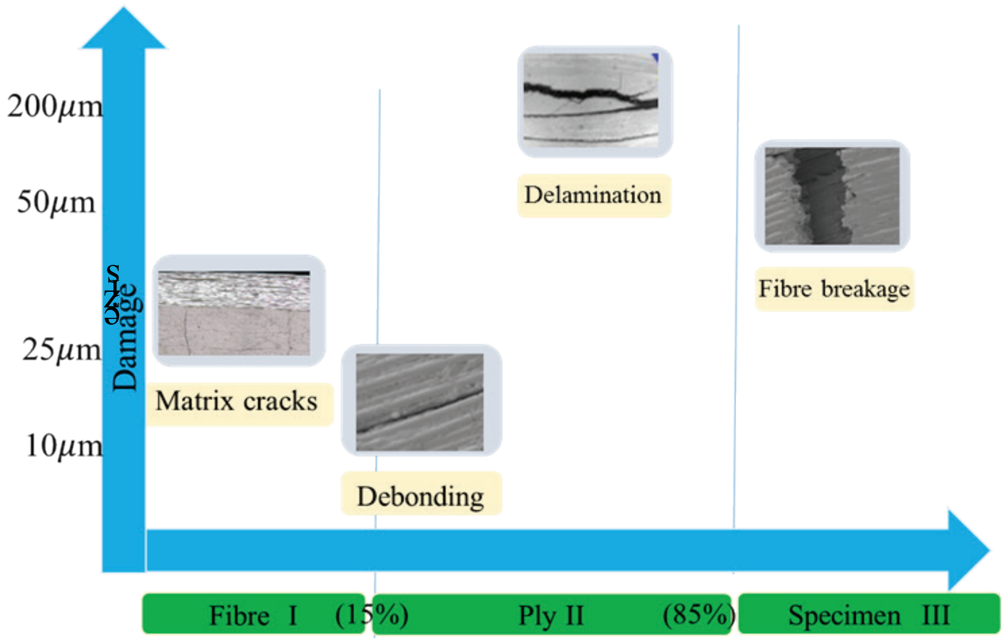

Figure 2-6 Evolving process of CFRP defects

2.3 Ultrasound NDT&E for CFRP

Ultrasonic testing (UT) is an NDT technique measuring the reflection and transmission of ultrasound waves in CFRPs. The frequency of the UT technique ranges from 20 kHz to 1 GHz in different applications [33]. In the UT testing, three types of elastic waves can be generated by the PZT sensor (piezoelectric), which are longitudinal, transversal, and Rayleigh waves[34]. Generally, the UT based QNDE can be A-scan, which is to measure the amplitude-time information of UT signal, the B-scan which is to conduct a line scan forming the amplitude image, the C-scan, which is a bi-direction scan to obtain the 2D image and the D-scan, which consist of the time of flight and a C-scan[35]. In the following sub-sections, the state-of-art techniques, including phased array and guided wave, are introduced.

2.3.1 Phased arrays

The UT based techniques have unique advantages for testing thick section CFRP components. In Ref.[36, 37], the phased array is applied for a 50 mm thick CFRP component with 0.5 MHz. The sweep frequency-based excitation, which is to apply a specific spectrum, for example, in Ref. [38], the excitation from 0.4 to 1.0 MHz, was used for a 25.4-mm-thick component using a matrix array transducer. The combination of the phased-array technique with TEM(total focusing method) was developed for the characterisation of defects with 16 mm depth in the CFRP component [39]. The limitation of UT based techniques, including phased array, is the requirement of a coupling agent for enhancing the effectiveness and efficiency of the PZT sensor, which can lead to contaminations if not correctly operated. Thus, the air-coupled ultrasound technique is developed for the non-contact measurement scenario. But the limitations of air-coupled ultrasound are that only lower frequencies(50 kHz to 0.8 MHz) can be used, leading to less sensitivity of detection compared with high-frequency excitation.[40]. As for the relevant work of air-couple ultrasound, in Ref. [40], the spectral transmission analysis of such technique in CFRP is conducted with a different thickness between 1mmm and 51 mm. In Ref.[36], an 80% reduction of amplitude in the transmission signal is discovered between 1mmm and 51 mm. In addition to the traditional multi-layer structure evaluated by phased array, the sandwich structure, which contains a low-density foam core with 50 mm thickness, is also investigated[36, 41]. In Ref.[42], embedded defective inclusion with different shapes and sizes are quantitatively investigated using the phased array. The results indicate that the high attenuation and distortion caused by the heterogeneous structure hinders the further application of such techniques. In Ref.[43], the phased array is applied for QNDE of the distribution of the voids on the surface of CFRP. In Ref. [44], the barely invisible impact damage is detected using an immersion phased array. The results indicate a 65-75% reduction of the overall loading capacity of the component resulting from the low-velocity impact. Based on the mentioned literature review, the limitations of phased arrays detecting CFRPs are:

(1) The phased array is capable of locating embedded defects in the composite laminates. However, the quantification of the shape and size were hindered by the attenuation and distortion caused by the inhomogeneity of the structure, which is illustrated in Ref.[42] and Figure 2-7.
(2) The propagation of longitudinal and transversal waves and Rayleigh waves depend heavily on the elastic properties of the material, which is influenced by the anisotropy of CFRP, making the evaluation of reflective waves difficult.

(3) The heterogeneous structure of CFRP makes it difficult for the high-frequency elastic wave to propagate into the thick section of the component, which affects the resolution and sensitivity of defect reconstruction.

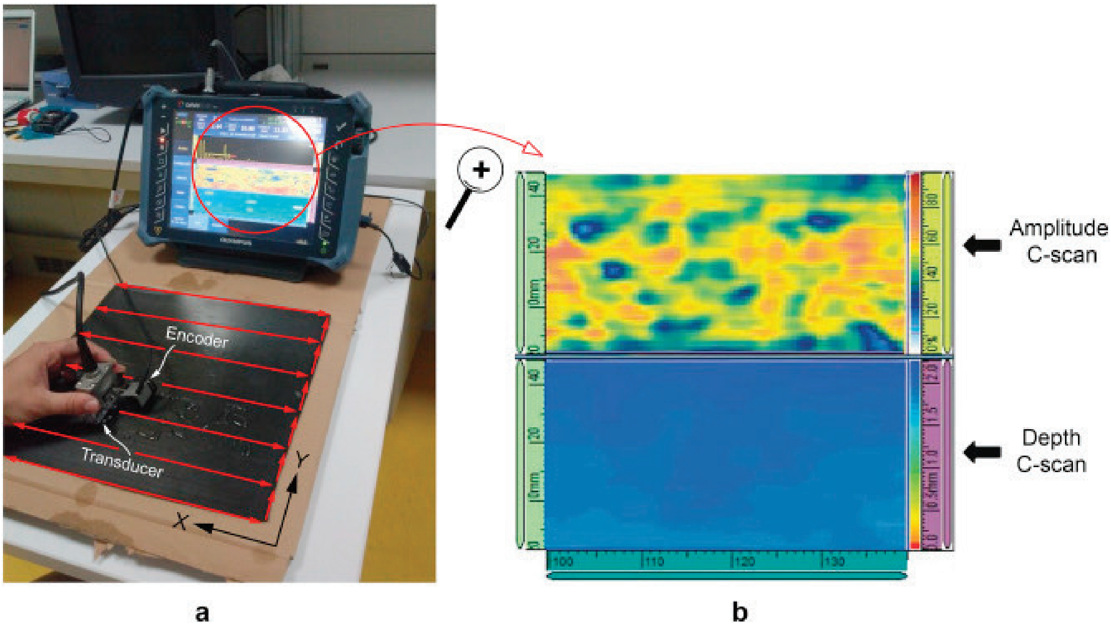

Figure 2-7 Experimental set-up of phased array ultrasonic testing[42]

(a) Olympus Omniscan MX2 and phased-array transducer with coupled encoder. (b) Ultrasonic C-scan images of amplitude and depth distributions of an undamaged CFRP laminate without artificial inclusions.

2.3.2 Guided wave

The guided wave technique is proposed to use the piezoelectric transducers to excite elastic waves confined by the boundaries or at the interfaces of a multi-layer structure, of which the principle is shown in Figure 2-8. The guided wave can travel a long distance with minor signal attenuation and high sensitivity to small structural damages[45]. Thin composite materials can be characterised using guided waves[46]. Guided waves are used for debonding detection, shown in Figure 2-9, properties QNDE, such as sample thickness characterisation[47], and estimation of the elastic constants[48]. For the guided wave technique, the symmetric fundamental mode can be used to characterise mechanical properties, such as elastic modulus, which is adequate to detect the variation of the material stiffness caused by failures[49]. In addition, the antisymmetric fundamental mode is established to detect delamination and cracks in the transverse direction in CFRP[50]. In Ref. [51], delamination with millimetre size was detected using B-scan by guided waves in a T-beam CFRP component. Besides, guided waves were also used in situ SHM approach for biaxial fatigue monitoring of CFRP [52]. During the in-situ test, guided waves can be used monitoring of the elastic properties, indicating the fatigue evolution of the material [53]. Based on the above literature review, the limitations of guided wave detecting composites are:

1) The heterogeneous structure, anisotropy properties of CFRP brings challenges for definitions of boundaries, thus increasing the complexity of guided wave propagation calculation.
2) Since guided wave can be excited with multi-modes, which are mixed in the response, it is challenging to excite pure mode, SH0, for minimizing interference mode[54].

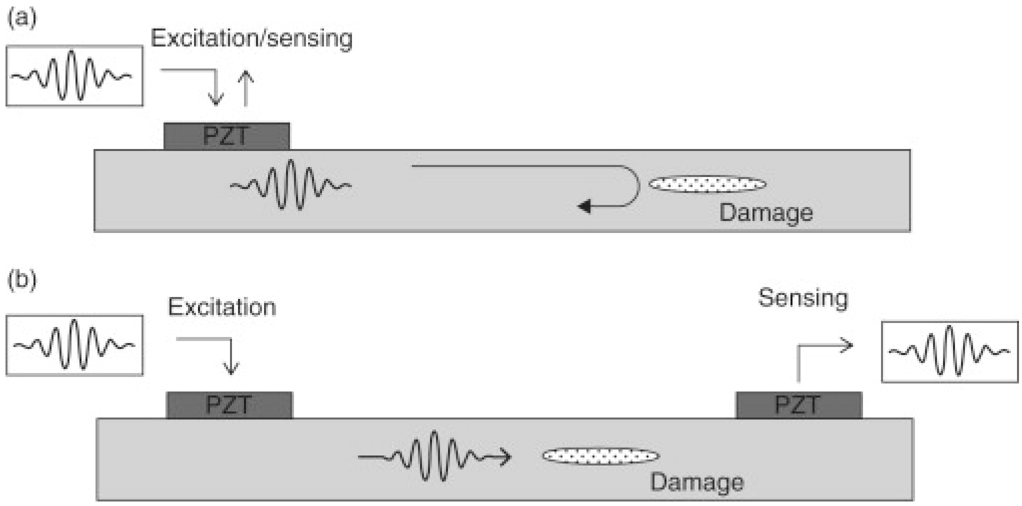

Figure 2-8 principles of different modes for guided wave measurements[55]

(a) pulse-echo mode and (b) pitch-catch mode.

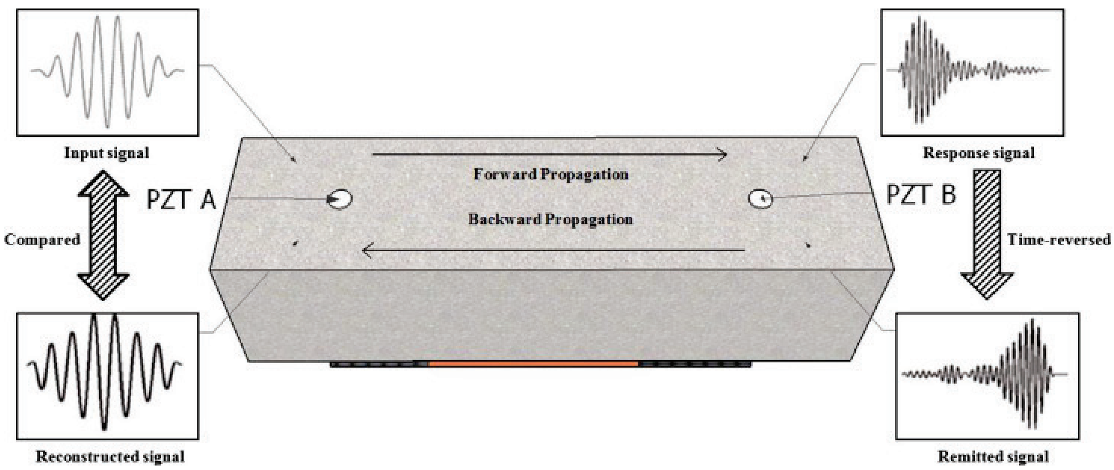

Figure 2-9 Ultrasonic guided waves for QNDE of debonding between concrete beams and carbon fibre reinforced polymer (CFRP) overlay[56]

2.4 Acoustic emission

The acoustic emission (AE) has been regarded as one of the NDT&E technique to detect and assess the possible failures in CFRP components[57]. The AE is based on the principle(shown in Figure 2-10) that the transient elastic wave of the specific material can be related to the evolution process of defects when there is stress applied to it, which propagates from the source to be detected by piezoelectric sensors. By using different features (e.g., signal amplitude, cumulative count and energy, duration, and the frequency information), various work has been conducted to achieve the structural health monitoring of damage inside composite materials[58-61]. These features can be applied for characterising the fatigue limit, of which the difference is less than the waller fatigue limit (5%) [62].

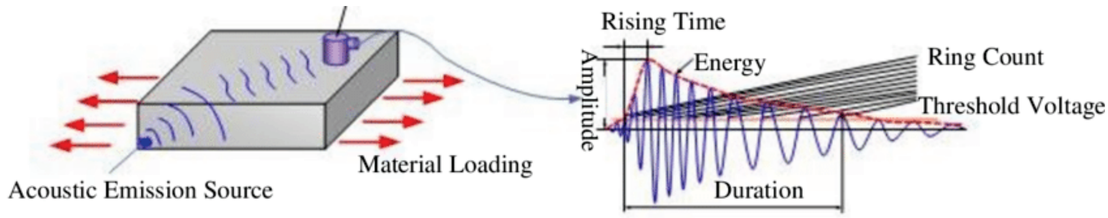

Figure 2-10 Principal of AE for detecting defects[63]

In the NDE of AE for composites, it is challenging to quantify the defect parameters due to the various experimental setups, including the frequency band, the characteristics of the preamplifier, and the threshold set in the acquisition process for denoising[64]. Besides, the range of AE amplitudes matched with different damage mechanisms is not fully investigated and can lead to overlapping issues. It is discovered that the most energetic response is from delamination and fibre fracture, while matrix crack is related to the weakest response[65].

In order to overcome these challenges, the solution is to use other AE parameters to enhance the damage analysis complementarily. The principal component analysis (PCA) is applied for damage detection on metallic and composites material[66]. The PCA enables the extraction of critical parameters to avoid redundancy. The artificial intelligence approach, the neural network method, is used for defect identification and classification [67]. In order to obtain higher accuracy of the feature extraction, it is necessary to train the neural network with data of the benchmark sample. The unsupervised approaches K-means are also used to classify different defects[68]. In

Ref.[69], it is shown that the damage accumulation leads to strong waveform distortion during cyclic loading of polymer composites compared with that recorded during static testing, resulting in changes in AE characteristics. Therefore, the effectiveness of the damage mechanism classification in the AE cannot be guaranteed. To increase the classification accuracy under the abovementioned conditions, a robust adaptive recognition algorithm is used[70]. In Ref.[71], the time-frequency analysis is applied to characterise the signal variation over time. It is proved to be a promising tool for transient signal analysis. In Ref. [72], the time-frequency analysis is used in combination with an AI approach(neural network) to classify six different levels of CFRP/GFRP under fatigue loading.

The AE technique is also capable of triangulating and locating the source of the emission through the sensor network. Since the establishment of sensor networks (more than three sensors are required) requires relatively large space, the experiment is mainly performed on large composite panels[73]. In Ref.[74], the CFRP laminate board with broken fibres and two artificially created delamination was applied for the tensile test(shown in Figure 2-11). During the test, the defects are perpendicular to the loading direction of the stress, the location of the AE events was successful, but the signal amplitude is not at the same level of fibre breakage in previous tests[74]. Thus, the limitation of the AE is the sufficient identification of AE events related to the damage mechanism when the anisotropy of the material induces a large amount of noise. It is capable of real-time monitoring in terms of detection, and location but this NDT technique is still qualitative and cannot provide quantitative evaluation defect information (e.g., size, depth)[75].

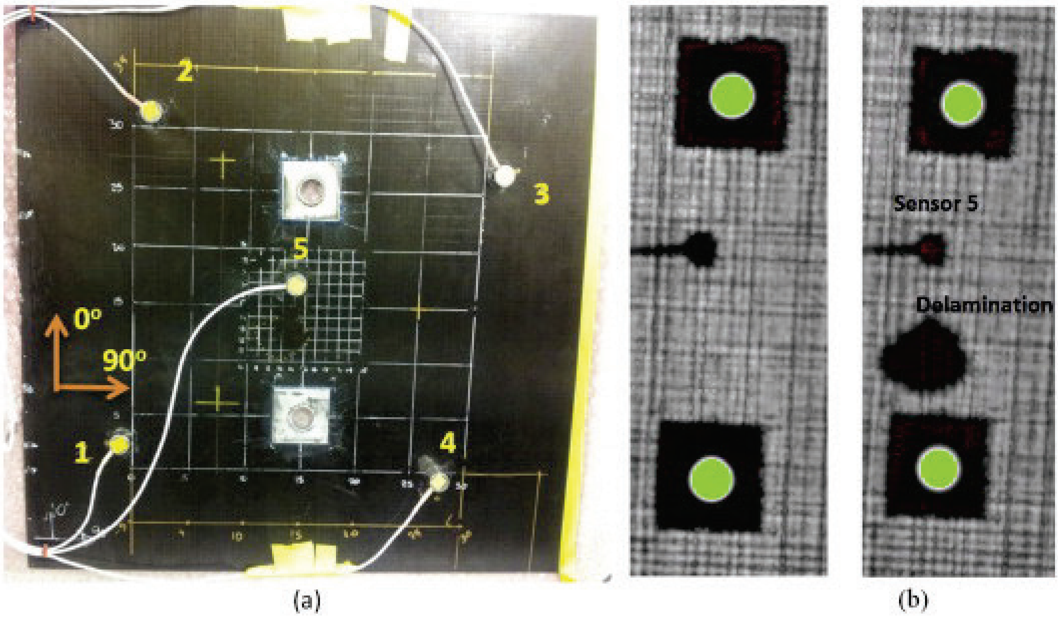

Figure 2-11 The acoustic emission for detecting delamination and fibre breakage in large-scale composites[74]

(a) Test specimen configuration (b) C-scan images before and after impact.

2.5 X-ray radiography and computed tomography

2.5.1 X-ray radiography

Radiography can utilize a ray for scanning the structure of certain material. In Ref. [76], the X-ray Radiography is applied to discover macroscale and mesoscale damage in the CFRP component (e.g., delamination, see Figure 2-12). In Ref [77], it enables the detection of cracks in a composite plane, which has a transverse direction to the X-ray beam. Low voltage radiography can be employed for thin components (less than 5 mm), whereas gamma-rays radiography is more established in the case of NDE for thicker components [78] if the defects that are propagated to the material's surface, the detection of such defects (e.g., matrix splitting) in the microscale could be enhanced by employing a dye penetrant. In Ref. [79], the initiation and propagation of matrix cracking in CFRP laminates due to the tensile loading were successfully observed. In Ref. [80], the X-ray radiography is applied for tracking the evolution of failures in bonding joints in CFRP components.

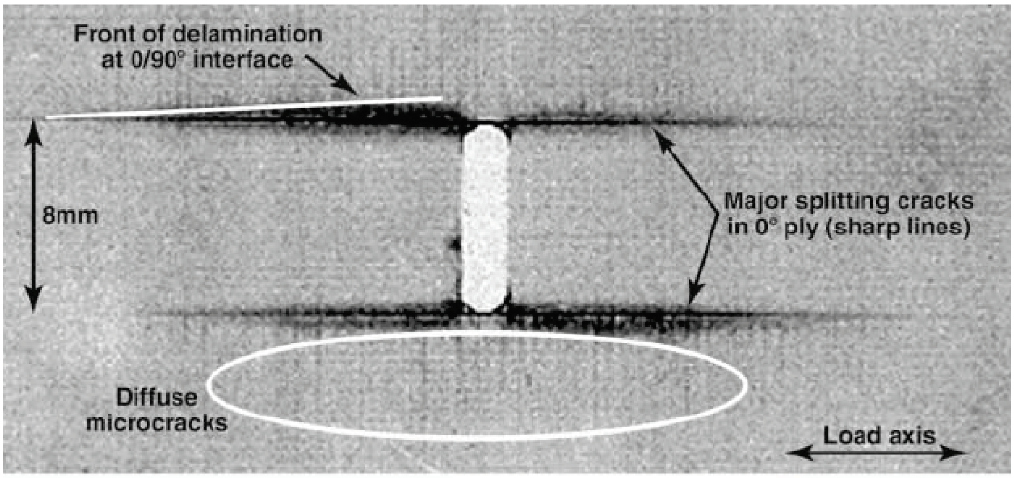

Figure 2-12 X-ray radiography for revealing the delamination and diffuse microcracks in CFRP[76]

2.5.2 X-ray computed tomography

The X-ray tomography (X-ray CT) is conducted by computing a collection of radiographs that are controlled by rotating the specimen with a calculated angular step[81]. The output data is called voxels with 3D dimensions that are coded in grey levels[82]. The grey level data are related to the linear attenuation coefficients of the material. Material with elements of high atomic numbers is the most absorbent, and material with a low density (e.g., air)is the least absorbent[35]. If the material and defects have different linear attenuation coefficients, the detection of such failure is possible.

The X-ray CT technique can offer both qualitative and qualitative evaluation for a comprehensive understanding of the damage mechanism. In recent years, lab-based equipment is designed to reconstruct and evaluate the 3D profile of heterogeneous structure in composites with reasonable resolution in micrometre[83]. The post-processing tools, including the thresholding[84], binarization[85], and 3D segmentation[86], were applied for the detection of voids and cracks in the composites laminate. The current challenge of maintaining reasonable resolutions is the compromise between the source energy and the required field of view in the voxel size[87]. The resolution is crucial for differentiating between artefacts and damage voids in composites [88].

There is a considerable amount of progress of X-ray CT for composites NDT in recent despite the fact that the fibres and matrix have the same level of atomic numbers[88].

To overcome the issue, one of the options is to use dye penetration to enhance the absorbance contrast if the cracks are propagated to the surface[89]. The alternate solution is to use synchrotron radiation computed tomography with the implementation of phase-contrast reconstruction[90]. The system can achieve the one μm voxel size. In Ref.[91], the fibre breakage evolving process is investigated using synchrotron radiation computed tomography system.

The X-ray CT was well established for the QNDE of semi-structural composites like GFRP(glass-fibre-reinforced polymers)[92]. In Ref.[93], the ex-situ diagnoses of defect initiation and propagation in GFRP was conducted for different fatigue cycles using X-ray CT. In Ref. [94], the complementary study was conducted for the detection of macro-void, and the results indicate that the failure initiates at the fibre with high local density in the GFRP component. In Ref.[95], the in-situ synchrotron radiation system with 0.7 μm voxel size was applied for GFRP under the tensile test(see Figure *2-13*). They discovered that the interfacial debonding initiates along with the fibre direction. But this spatial resolution(0.7 μm voxel size)wasn't enough to discover failure initiation (e.g. matrix crack)[96].

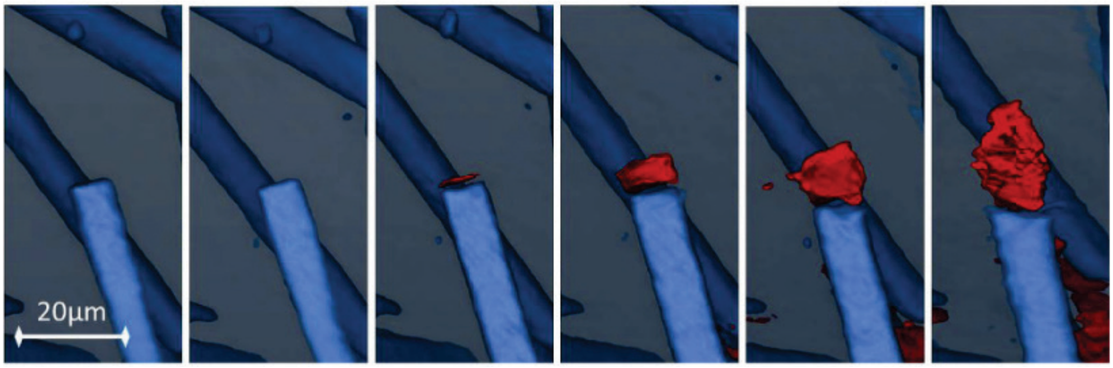

Figure 2-13 Growing fibre breakage detected by X-ray CT under tensile test[95]

Besides, X-ray CT is also developed rapidly for 3D woven composites. In Ref. [97], the lapse-time was applied for tracking the damage evolution under different fatigue cycles. Ex-situ tests were conducted to reconstruct the damage profile at different levels[98]. It was found that the transverse cracks initiation seemed at 0.1% of its service life. After that, the cracks start to increase with steady speed. A stabilization of cracks at around 60% of its service life was detected together with debonding[97].

The 3D reconstruction of and imaging techniques play an essential role in X-ray CT QNDE. The 3D images with high fidelity can help to investigate the initialization, progression of the failures using human observations[99]. In this field, different approaches are applied to investigate the mechanical behaviour of the CFRP components. Figure 2-14 presents the various approaches for modelling assisted X-ray CT[88]. The modelling using 3D images is to build FE(finite element) based on the image of composite constituents of different scales and investigating virtual experiments using the numerical model for predicting the mechanical behaviour. In Ref. [100], the 3D X-ray images were converted into a meshed profile in the FE model. However, the process for converting the CT images to FE geometry entities is sometimes challenging in terms of single fibre extraction for microscale modelling due to the low contrast between fibre and matrix.

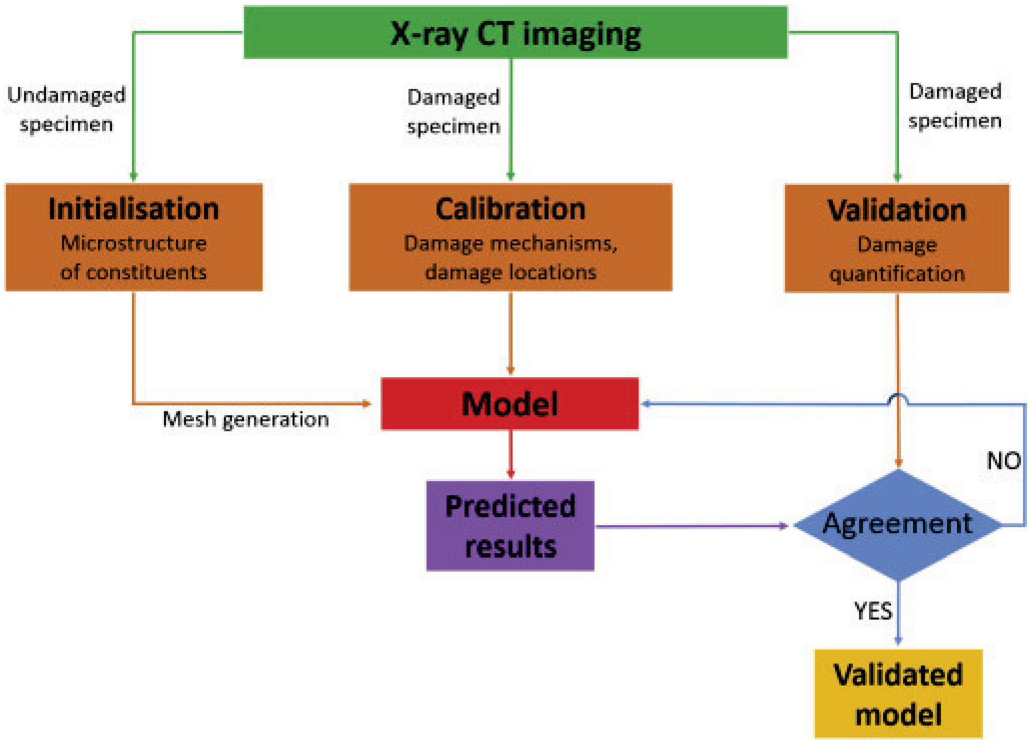

Figure 2-14 Model assisted X-ray CT imaging for composites QNDE[88]

The review of state of the art for composites NDT&E using X-ray radiography and computed tomography indicates its capability to comprehensively evaluate the structure and thus observing its life-cycle failure mechanism. What's more, the X-Ray NDT&E enables the capability to understand the progression of defects in certain volumes with correlations to evaluating strain localization in the in-depth direction [101].

However, the challenges are still requiring a further solution. For instance, the life-cycle monitoring of failure progression requires both reasonable spatial and temporal resolutions. The high cost of X-ray test operation (experimental and post-processing tools) and dataset with high dimensions make the QNDE challenging and impractical for industrial applications[102].

2.6 Active thermography

The active thermography requires thermal excitation by using, for example, pulsed or continuous lamps, acoustic vibration of the structure (vibrothermography) using a high-power ultrasonic source [103, 104]. In AT, the thermal pattern of different material excited by the heating source is captured by the IR camera to provide information on possible discontinuity on the surface or in the subsurface. The signature of the defect is generated by the difference in the thermal diffusion rate between the sound areas and defective areas[105]. With this advantage, the active thermography is promising for the NDT&E of composite compared with X-ray CT or UT due to its competitive cost and fast scanning time[106].

2.6.1 Thermography NDT systems

Optical-based thermography is the most common AT techniques. Based on different excitation, the optical-based thermography can be divided into the pulse, lock-in, long pulse, step heating, and frequency modulated thermography, shown in Figure 2-15. Pulse thermography has been applied to detect two types of defects, which are defects with millimetre size and barely invisible impact damage(BVID)[107, 108]. In Ref.[109], the thermo-mechanical properties are characterised in CFRP. In Ref. [110], the correlation is established between the applied stress and the cooling speed of the sample with flash lamp excitation. The pulsed phased thermography, which is to extract thermal images at different phases through Fourier transform, is also proposed for the evaluation of the CFRP component[111]. In Ref. [112], the pulsed phase thermography is applied to visualize the matrix cracks in a GFRP. In Ref. [113], the porosity in the composites is evaluated with the evolution process of thermal diffusivity at different fatigue cycling, and the results indicate that the thermal diffusivity is inverse proportional to the porosity. As for the conventional post-processing tools, the Fourier transform, wavelet decomposition, and image processing techniques, including 2D wavelets, PCA, and ICA, is used for cracks and delamination detection [114, 115].

The lock-in thermography, which is to excite a sinusoidally modulated heating source, has the advantage of being less influenced by the variations of surface emissivity[116]. Defects detection, such as porosity, has been applied with lock-in thermography for its detection[117]. In Ref. [118], the skin-to-core debonding in the honey-comb structure are investigated using LIT techniques with the analysis of phase change on the surface thermal pattern. In Ref. [119], the LIT approach was compared with other NDE approaches, including shearography, thermionics, and UT techniques, which indicated the full field capability of LIT. In Ref. [120], the impact damage with different materials, such as carbon fibre rain-enforced, glass fibre rain-enforced, is applied with LIT to defect failures like fibre breakage and delamination.

The laser-spot thermography, compared with optical-based thermography, is more adapted to defect cracks or failures in planes perpendicular to the surface[121]. The inspection of the sample using laser spot thermography is scanning a line or a point at a fixed speed. In Ref. [122, 123], the sub-surface defects(Telfon) in the composites honey-comb structure are detected using laser-induced thermography, which has good agreement with UT C-scan images, which is illustrated in Figure 2-16. The flying laser spot thermography is employed to detect and assess the orientation of CFRP[124]. The automation and non-contact capability of laser thermography make it quite promising for high-end aerospace applications.

The author is well aware of the massive amounts of AT techniques for CFRP QNDE. However, since the thesis mainly focuses on eddy current pulsed thermography, the detailed and comprehensive review of AT for CFRP can be found in Ref.[125]. Based on the above literature review, the challenges for detecting the composites are:

(1) In-depth characterisation is still limited. Depending on the sinus frequency, sub-surface (no deeper than 3.5 mm) millimetres size defects become visible.
(2) Anisotropic material properties tend to generate un-uniform heating, which decreases the SNR in the thermal picture.
(3) Thermography NDT techniques are advanced with the development of deep learning and machine learning techniques in recent years. The post-processing techniques for thermograms are enabling the automatic detection and evaluation of defects and failures in the near future[126].

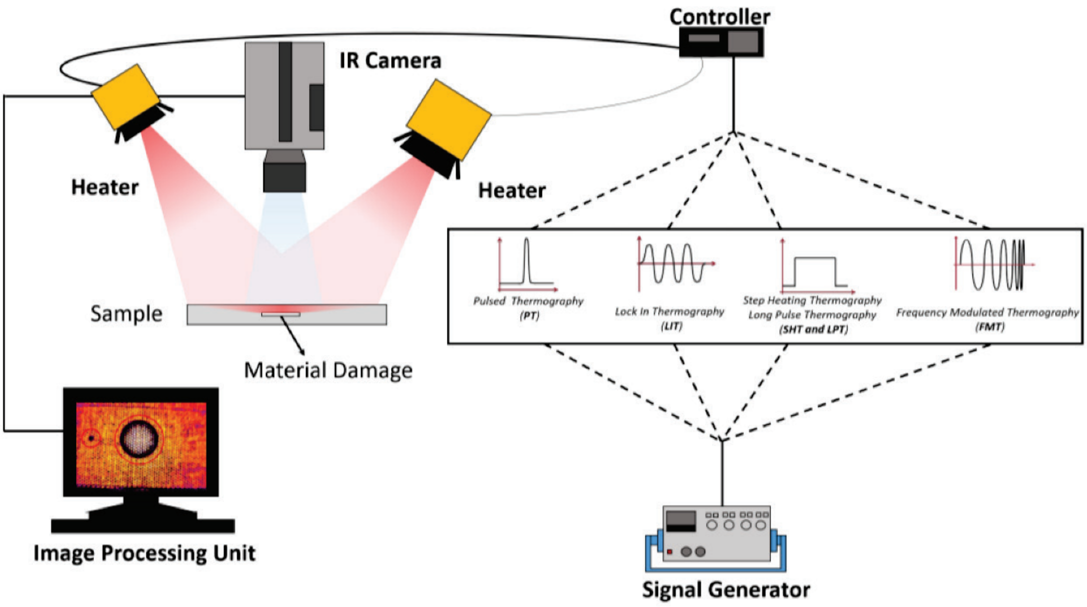

Figure 2-15 Optical based thermography with various excitations[125]

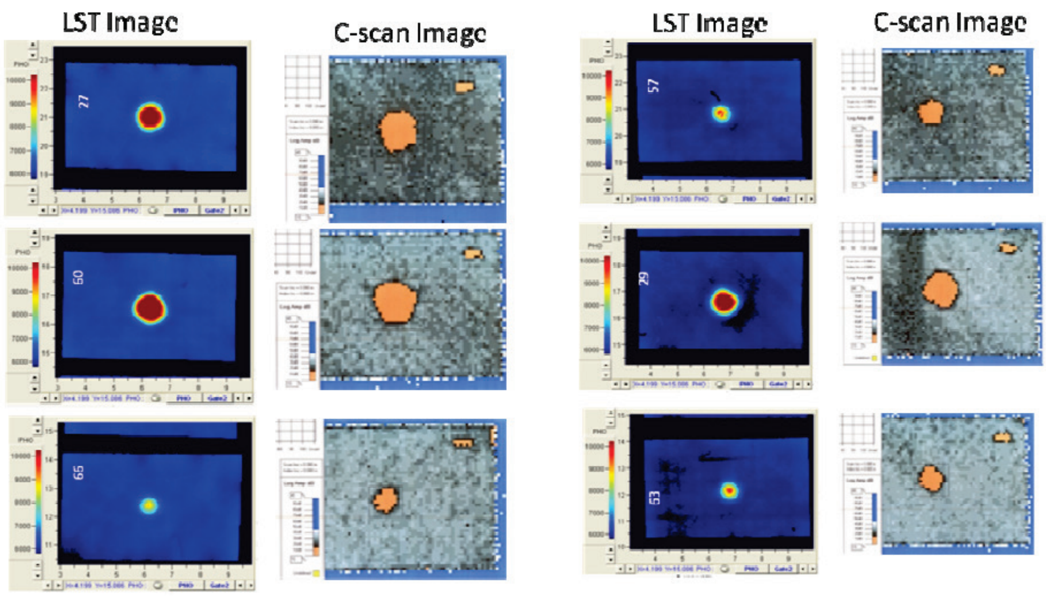

Figure 2-16 Comparison between LST images and C-scan images for delamination detection[122]

2.6.2 Thermography post-processing methods

The thermography post-processing methods are essential for extracting the quick change in the transient response for characterising the difference between defect and sound areas. In this section, the state-of-art post-processing tools are reviewed and introduced

2.6.2.1 Thermal signal reconstruction (TSR)

The thermal signal reconstruction (TSR) is to use derivatives of logarithmic temperature in the cooling stage of transient response. The approach is to apply the polynomial model to fit the logarithmic decay. It is observed that in Figure 2-17, the defect-free sample has a straight slope, while for samples with defects, the diversion from the sound sample's response can be considered with defect presence[127]. However, fitting using 3 to 5 orders of polynomial fitting can be influenced by the *Runge effect,* which is defined as unsolicited noise during thermography testing. The temperature contrast function is applied to tackle the issue by using the derivatives of the contrast function[128]. Various features in the TSR, including normalized temperature contrast, t_{PCT} (time of peak contrast), t'_{max} time of temperature first derivative reaching maximum value and t_{PSDT} (the peak-second derivative time of logarithmic temperature) were explored for characterising subsurface defects[129]. The normalized temperature contrast is shown in Figure *2-17*(a). It is reported that the normalized temperature contrast is not sufficient for providing the information of defect appearance over time[130]. Thus the feature illustrates t_{PCT} (time of peak contrast) is presented in Figure *2-17*(b). In Ref. [127], the two features including the t_{PCT} and t_{PSDT} are reported to be investigated for sample with FBH(flat bottom hole) and two-layer model. It is proved that the t_{PSDT} shows better accuracy for evaluating the depth. Additionally, the t_{PSDT} using the second derivative peak can serve as the reference for better fit of the polynomial model[131].

Another type of feature which is derivative of the logarithm temperature function, which is further implemented as t'_{max} and t'_{min}. The t'_{max} and t'_{min} are defined as time to reach its minimum and maximum values in the logarithm temperature function. It is discovered that the features can characterise the lateral diffusion of heat transfer due to finite lateral extension caused by the buried defect[132]. The features can be adapted to quantify the dimension parameters of the defects with the small aspect ratio D/d, where D is the defect diameter, and the d is defect depth.

There are still issues with the application of TSR on thermal NDT data for CFRP. Firstly, the thickness of the CFRP laminate cannot be considered as a semi-infinite case. It can be solved by comparing the data of temperature over time between defect and non-defect area[133]. Additionally, it is discussed that due to the multi-layer structure of the CFRP(see Figure 2-18), the thermal response has more rebonds on the interface, which is challenging to be interpreted by the TSR method[134].

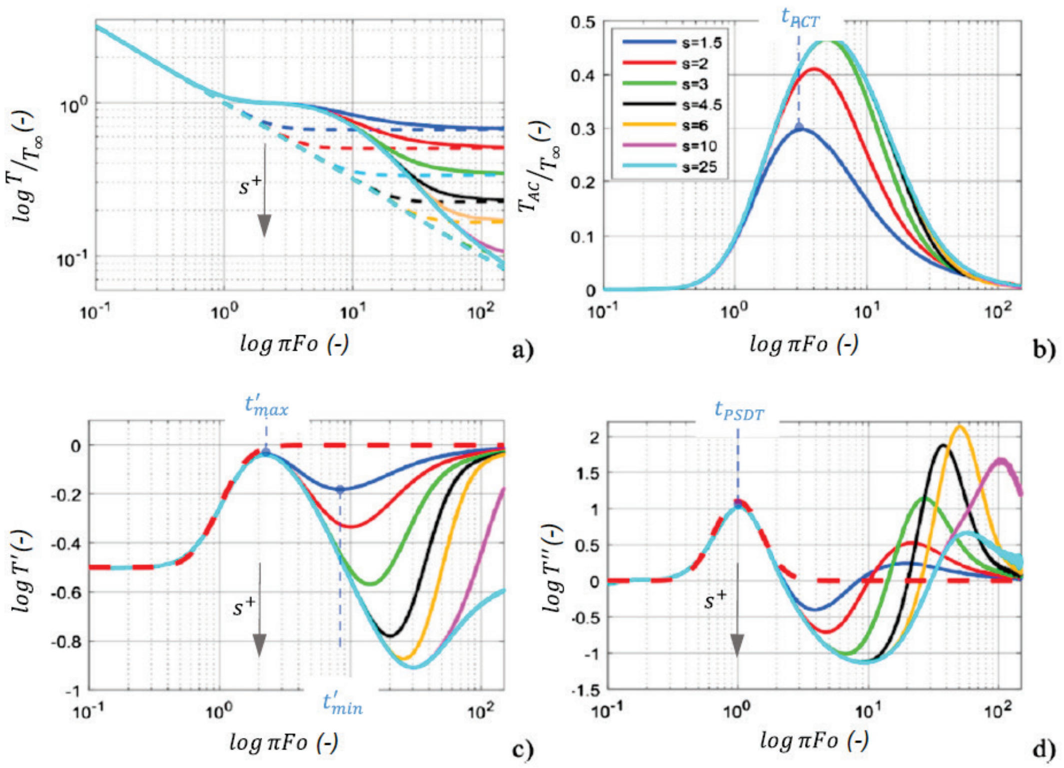

Figure 2-17 Illustration of various TSR features

(a) normalized temperature contrast (b)t_{PCT} time of peak contrast (c) t'_{max} time of temperature first derivative reaching maximum values (d) t_{PSDT} the peak-second derivative time of logarithmic temperature[126]

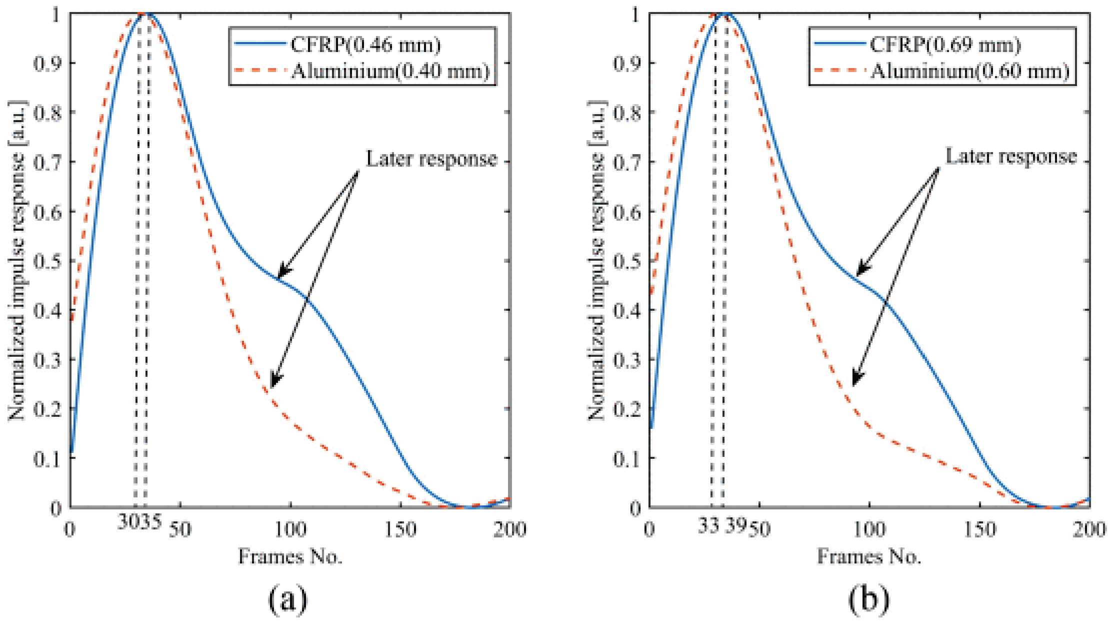

Figure 2-18 Comparison of a normalized impulse response of subsurface defects between CFRP and Aluminium

(a) CFRP sample with a defect depth of 0.46 mm and an aluminium sample with a defect depth of 0.40 mm. (b) CFRP sample with a defect depth of 0.69 mm and an aluminium sample with defect depth of 0.60 mm[134].

2.6.2.2 Statistics based features

The statistical methods for thermal data post-processing are also implemented massively in the field due to their simplicity and ability to extract high-order signatures. These methods mainly rely on the mathematical presentation of the thermal data resulting in the unclear physical interpretation of the results[135].

The absolute peak-slope time (APST) is primarily implemented by extracting an inflexion feature on the first derivative of transient response by multiplying the cooling stage response time-powered by 0.5 [136]. This method is based on the principle that the time of flight of thermal waves can be correlated with the calculation of cooling state response. The feature has the merit of being reference-independent but suffers from noise, which has similar characteristics as derivative-based features[137]. The Least-Square Fitting (LSF) methods are to fit the transient response with different fitting models so that the coefficients of the model can be used to interpret the signatures of the defect[138]. Compared with derivative and APST, due to the fitting process, the Least-Square Fitting is more robust to the noise but lack reasonable sensitivity[139].

In recent years, the high order statistics (HOS) feature extraction methods were designed to enhance defect detectability, especially the subsurface defects[140, 141]. In Ref. [142], the 3rd order approach (skewness) is applied in the ECPT system, where the author has summarized the contribution of the heating and cooling stage, respectively, to enhance the capability of the feature(see *Figure 2-19*). The 4th order (Kurtosis) feature is also applied in the ECPT system to demonstrate its robustness to non-uniform heating patterns for defect angles characterisation[143].

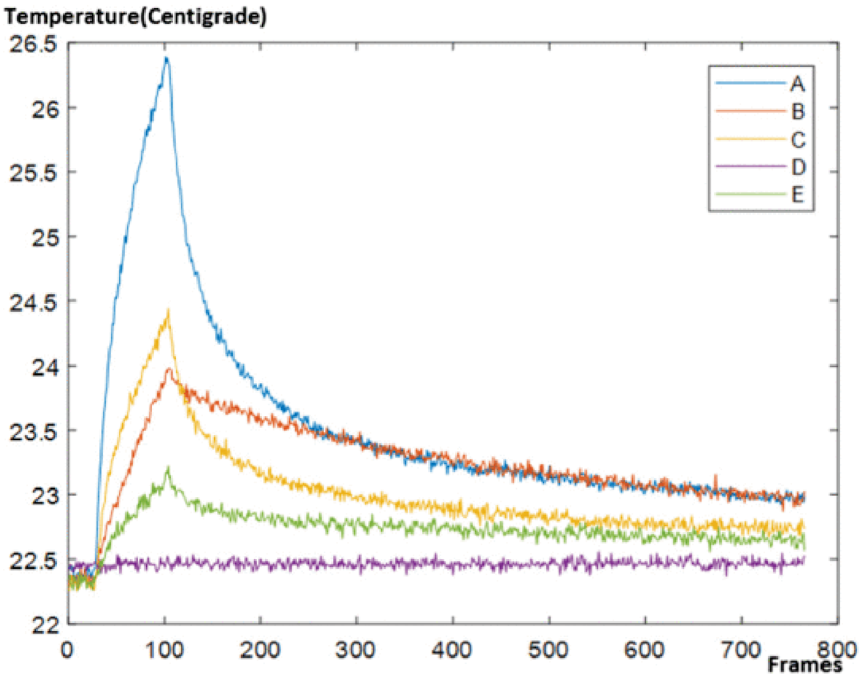

Figure 2-19 Skewness features for the thermal transient response on selected points[142].

2.6.2.3 Matrix factorization and decomposition-based feature extraction

The thermal data can be considered as a 3D matrix with its spatial, temporal, and thermal information. Thus these 3D matrix, or tensor, can be decomposed into a product of matrices through matrix factorization techniques, with each decomposed matrix characterising the signature of the data in a certain dimension[144]. The matrix decomposition is usually implemented by singular value decomposition (SVD). In Ref.[145], the PCA(principal component analysis) is applied to decompose the 2D raster data, with each row denotes all pixels from a single image. Different rows correspond to image at different times. Therefore, each column represents the transient response of individual pixels. By obtaining the eigenvalues and their corresponding eigenvectors with the same dimension of transient response through using SVD, the 2D raster reshaped matrix is decomposed into the so-called empirical orthogonal functions [146, 147]. In this case, different eigenvectors represent the transient response with its specific physics meaning. For instance, the first component with the largest eigenvalue is considered as the thermal signature from the sound area(background), while the second or third component can be related to the defective signature[148, 149]. Thus, by obtaining the defective signature and projecting the 2D raster data to this dimension, the 2D image with an enhanced signature from the defect is obtained(see Figure 2-20)[150]. Besides, the PCA approach can also help compress and reduce the dimension of the 3D thermal data for AI-based classification, e.g., Neural Network, CNN(Convolutional neural network)[151], and ANN(Artificial Neural Networks) [152]. Additionally, the ICA approach (Independent Component Analysis) is also integrated to serve as a complementary approach for quantifying defects with different parameters, e.g., the characterisation of impact damages of BVID(barely invisible impact damage) with different energy in composite[147, 153, 154]. The difference between ICA and PCA approach is that the decomposed components in PCA are empirically orthogonal, while the transformed data in ICA are independent of each other. In Ref. [155], it is concluded that in only the first three or four of components are contributing to the defect location, while in the ICA based approach can extract components with an equal contribution for multi-parameters characterisation, e.g., multi-defects, multi-layers and etc.

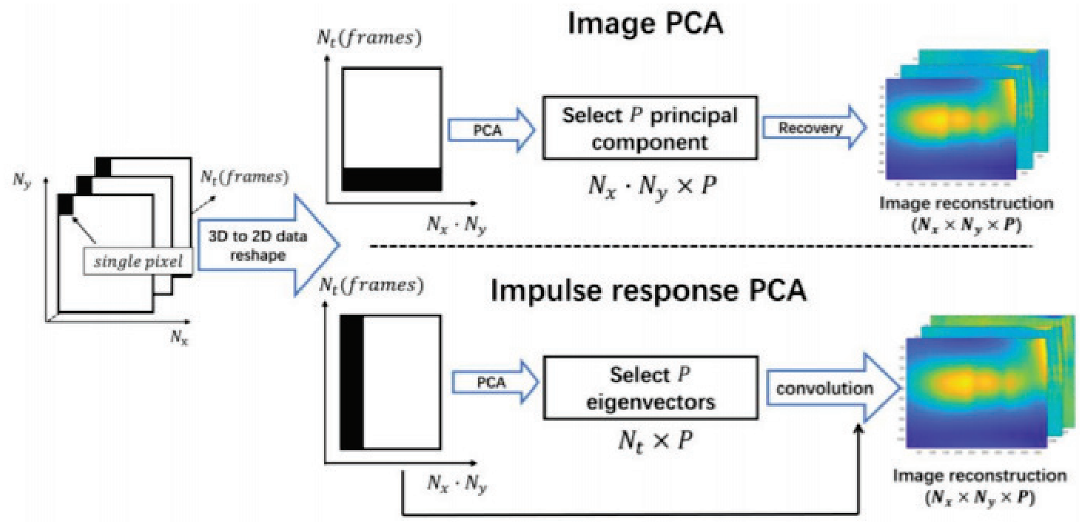

Figure 2-20 Mathematical presentation of PCA approaches for thermal NDE[150]

The latest development for matrix factorization approaches for thermal NDE is the application of kernel PCA[156], kernel ICA[157], and sparse decomposition[158] for tackling different scenarios. The kernel function is usually for non-linear data linearization. By mapping the thermal data to kernel space[159], it is possible to enhance the sensitivity of the thermal NDE approach on multi-layer and heterogeneous structure[134].

To summarize, the matrix decomposition approaches are efficient for extracting the defect signature when the dimension of the data is large and require extra efforts for selecting the high-SNR image[160]. However, these approaches also require a high level of expertise for designing proper kernel function and selecting relevant principal components for further feature extraction.

2.6.2.4 Machining learning and artificial intelligence for thermal NDT

In recent years, the progression of computer vision also enabled the development of the processing of thermal image and video. The machine vision provides the possibility for automatic detection of the classification of the defect and its parameters, respectively[161].

Machine learning can deal with multi-parametric QNDE problem. In this way, the manual selection of the features and extra efforts for guiding programming can be avoided. In Ref. [162], the ANN is applied to exploit the benefits of characterising the sub-surface flaws. In Ref. [163], the partial least square techniques were applied for removing of non-uniform heating pattern, which results in the high SNR of the thermal images. In Ref. [164], the thermal diffusion in the lateral dimension is considered using the spatial relationship between pixels; the local region segmentation algorithm is then proposed for the detection of the defects. In Ref. [165], the manifold learning algorithm is applied together with isometric feature mapping methods for segmenting the defective regions and non-defective regions for thermal data. In Ref. [166], the author proposed the entropy maximization technique applied to the 2-D grayscale histogram to achieve thermal image segmentation. In Ref. [167], the author developed the regional growth technique for thermal data processing, which has been applied successfully on the CFRP component. In Ref. [168, 169], the cluster-based method is also applied to the detection of defects. To increase the capability of cluster-based methods, Ref. [169] has conducted the analysis using the thermographic cluster analysis (TCA) method and combined it with the hyper-image segmentation for automatically detecting and segmenting the defect profile. In Ref. [170], the visual geometry group-Unet is applied to the 3D thermal data for cross-learning and segmentation of flat bottom holes of different sizes for automatic detection, which is shown in Figure 2-21.

The current limitations of the machine learning approach still exist. For unsupervised learning methods (e.g., Cluster, K-means, Gaussian mixture), the issue is the lack of robustness to complex interference(e.g., texture profile, edge effect)[124]. For supervised learning, it is still not practical for industrial applications compared with unsupervised learning due to a lack of large amounts of benchmark data[160].

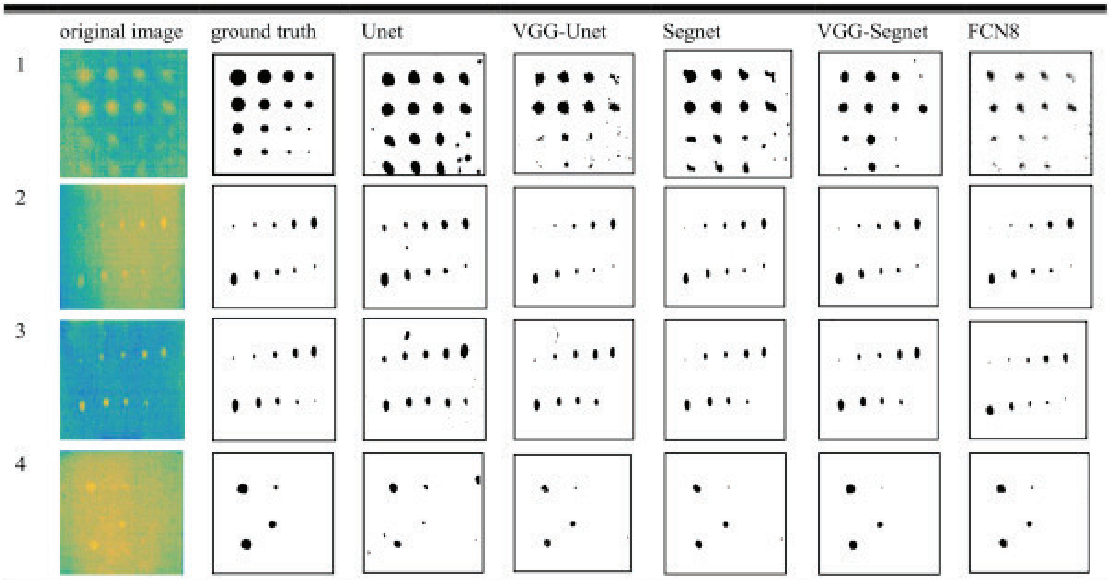

Figure 2-21 Image segmentation of flat bottom holes in CFRP using various deep learning structures[170]

2.6.2.5 Thermography reconstruction approach

Thermography reconstruction can serve as an 'ultra' solution for comprehensively evaluating the profile of the defect. The thermography reconstruction is an inverse ill-posed problem[171]. To implement the optimisation between the forward calculation and experimental data, both the forward model(either analytical or numerical) and the inversion strategy are required[170].

A flaw shape reconstruction algorithm was suggested for pulsed thermography using on the interpretation of contrast derivative between experimental data and simulated data [172]. One drawback of these direct methods is that 2D/3D heat transfer is not considered. An alternative solution for the problem is to consider the 2D/3D heat equation as a nonlinear ill-posed problem [173]. In Ref. [174], the author developed an inversion solution for the reconstruction of hidden corrosion using pulsed thermography techniques. It is reported that the two drawbacks of puled thermography exist for thermography reconstruction. Firstly, the temporal resolution is limited by the fact that early-stage response is required for defect detection to avoid further lateral diffusion. The second limitation is the nature of the ill-posed problem that variation of the starting points can cause a huge difference in contrast to the true profile[126]. Optimisation methods, e.g., least-squares [175], gradient search [176], Levenberg–Marquardt [171], can minimize the computed data with the experimental data through iterative calculation. By using optimisation-based inversion algorithms, the defect parameters can be approximated by minimizing the error between the theoretical and predicted data. In Ref.[177], an inverse approach is proposed for the detection of defect and estimation of thermal diffusivity CFRP laminate using lock-in thermographic phase (LITP) profile reconstruction. The inversion algorithm combines simulation annealing algorithm (SA) and Nelder–Mead simplex search method (NM) for minimizing the objective function. The reconstruction profile is presented in Figure 2-22. It is reported that this approach can only be used for the determination of thermal diffusivities of CFRP laminate with the subsurface defect.

However, the real defects, in most cases, are not FBH(flat-bottom holes). The issue of the complex geometrical poses challenges for boundary condition definition, which results in a drastic increase in computation complexity for forward calculation[178]. In Ref. [171], one iterative algorithm for reconstructing back wall geometry is implemented by optimisation between measurement and simulation (FEM) of heat diffusion at an early stage. The above solutions are promising but can be challenging when applied to the reconstruction of layered composites, which can be severely influenced by anisotropic thermal diffusion caused by the different orientations in each layer. Without considering the anisotropic behaviour of the material, time-reverse reconstruction results can be less accurate and more computationally expensive to be performed.

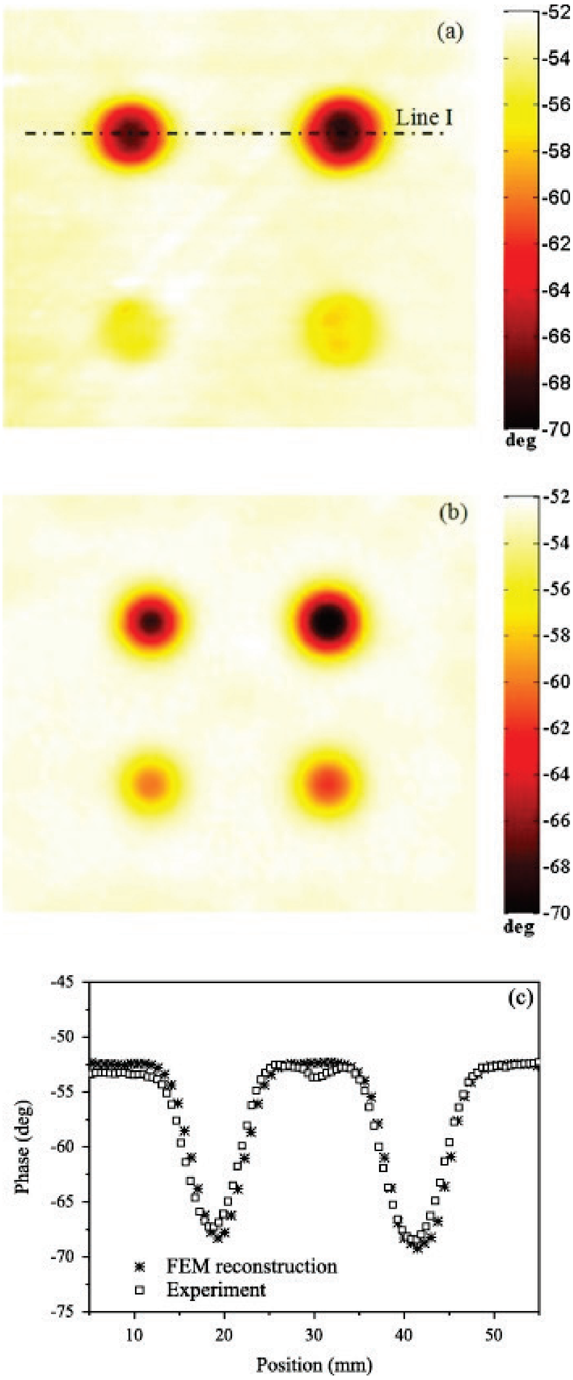

Figure 2-22 Lock thermography based reconstruction for FBH : (a) experimental LITP image, and (b) FEM reconstruction, and (c) Experimental and FEM profile comparison of line scan[177].

2.7 Microwave NDT for CFRP

The microwave NDT refers to the usage of EM wave ranges from 300 MHz to 300 GHz, which has wavelength ranges from 1m to 1mm for CFRP NDT&E[179]. The EM wave radiating from the waveguide or antenna interact directly with the material. The features used for microwave NDT is the reflection coefficient[145, 180]. With the increase of operation frequency, a smaller size probe is needed. Compared with ECT testing, due to the high-frequency EM wave, the range of radiation is smaller than that of low-frequency EM testing, it required less protection[181].

The frequency band for Microwave NDT can be divided into X band (8-12 GHz), Ku band (12-18 GHz), K band (18-26.5 GHz), and Ka-band (26.5-40 GHz)[182]. There are some work using the K band for the QNDE of CFRP in terms of the low energy impact damage evaluation. In Ref. [183], BVID from 4J to 12J was detected by the MORWG method, and the work applied PCA for extracting defective response, which is represented by PCs(Principal components) and multiply PCs with original data to obtain the defect signature enhancement image. The optimized operating procedures have been conducted due to the MORWG system highly relies on the step size of the scanning. In Ref. [184], an investigation of simulation on impact damage on GFRP using an open-ended microwave waveguide has been conducted. The results indicated that the pattern of impact damage could be obtained with the scanning step size fixed at half of the length and width of waveguide aperture, in the X and Y direction, respectively. In Ref. [183], it was found that the optimal direction for fibre breakage detection using MORWG is to remain parallel orientation of the electric field, which is polarized in by waveguide

However, due to the high conductivity and high permittivity of the CFRP, the NDT on CFRP remains challenging. It is expected to explore the multi-spectrum operation using MORWG in future work[185]. Additionally, the operation process, including optimized step size, angles of probes, are expected quantitative comparison. PCA feature is used for unsupervised classification; more appropriate feature extraction methods are recommended for internal and low energy impact damage. Moreover, the applicability of probes under different geometry should be further extended.

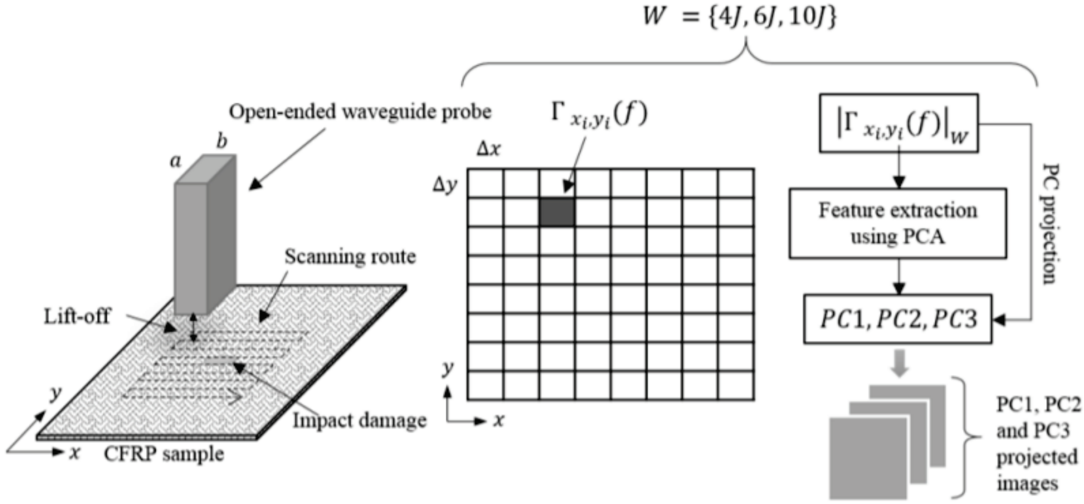

Figure 2-23 Microwave open-ended waveguide for CFRP impact damage QNDE[186]

2.8 Eddy current and eddy current pulsed thermography for CFRP

Eddy current testing is well established and widely applied in the ENDE(Electromagnetic Non-destructive Evaluation) community for NDT&E of CFRP.[13]. The principle of ECT testing is to induce the eddy current inside the conductive material, so that discontinuity of the material can be characterised by the impedance measured by the coil, shown in Figure 2-24. The eddy current uses the EM wave with a frequency from 10kHz to 100 MHz, which enables its applications from a conductive material such as metal and to less conductivity such as composites [187, 188]. In the ECT testing, the permittivity and conductivity of CFRP are key parameters to be measured with the ECT probe using impedance change[180]. The information on the CFRP component, including fibre orientation, delamination, crack, is featured by the conductivity variation. The local curing defects, such as porosity, thermal impacts, and the degradation of the polymer, can be characterised by permittivity variation. The abovementioned detection can be implemented by changing the frequency range. The unique advantage of ECT testing is non-contact measurement and fast scanning capability. Compared with X-ray or radiography methods, ECT testing is less expensive in terms of operation cost and less harm to the human body. [189]. However, there exists a huge difference in ECT's application between metallic material and less conductive composites. Compared with metallic samples, the lower electrical conductivity of CFRP leads to a larger skin depth of the material. Besides, the CFRP sample consists of conductive fibres and non-conductive polymer, which heavily affects the accurate measurement of impedance. Several strategies are overcome in the community in terms of the design of the Tx-Rx ECT probe and applying a polarized diagram for characterising its anisotropy[190-193]. In Ref. [194], it is found that the conductivity of CFRP was inversely proportional to the peak frequency of the imaginary inductance. In Ref. [195], the numerical model is developed to investigate the anisotropic conductivity's influence in a multi-layer CFRP laminate. In Ref. [196], it is found that the induced current density existing in overlapped fibres is higher than that of the unidirectional ones due to the contact between fibres reducing the resistivity. In recent years, ECT testing is applied as a heating source as active thermography, and this multi-physics QNDE approach shows its potential for CFRP NDT&E.

Eddy current pulsed thermography is to induce eddy current as of the heating source, discontinuity of the structure is interacting directly with eddy current. Thus the abnormal heating can be captured by the IR camera, of which the principle [197]. In ECPT testing, two configurations are applied for different scenarios: reflection mode transmission mode, which is shown in Figure *2-25* [198, 199]. Similar to ECT testing, the skin effect plays an important role in induction heating. Two heating modes can be found in the literature:(1) **Surface or near-surface heating**. In this case, due to the high electrical conductivity of the material, the skin depth is much small, and heating is happened on the surface[200]. In Ref. [201], for example, ferromagnetic metals have a skin depth of 0.04 mm at 100KHz excitation. The detection of the surface cracks of metallic samples is based on the eddy current's direct interaction, while for defect at a certain depth, it requires heat diffusion to the defect and reflected to be detected by IR camera[134]. (2) **Volumetric heating mode**. This mode refers to large skin depth due to the low electrical conductivity of CFRP. In Ref. [202, 203], it is reported that the skin depth in CFRP is about 50 mm with 100 kHz excitation. Considering the sample thickness is less than 10mm in the usual case, the heating happens on the entire sample. Therefore, the ECPT system owns the merits such as fast inspection speed and considerable penetration depth, higher resolution of IR camera compared with ECT. Compared with other AT techniques such as optical-based thermography, ECPT is less influenced by surface conditions of the sample (e.g.dust, oil contamination). Comparing with UT, it is non-contact measurement.

The literature review of eddy current testing composites and eddy current pulsed thermography is further discussed in four subsections. Section 2.6.1 reviews the state-of-art simulation method for modelling composites. Section 2.6.2 discusses four different eddy current experiment systems, including their applicability and limitation. Section 2.6.3 reviews the post-processing techniques for ECPT and ECPT. The applications to detect different defects in CFRP is presented in Section 2.6.4.

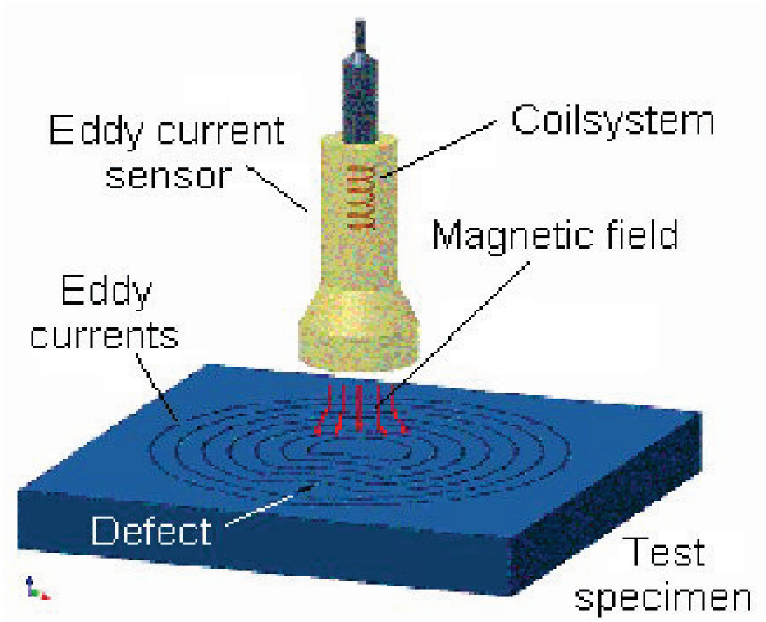

Figure 2-24 Principle of eddy current testing for CFRP[204]

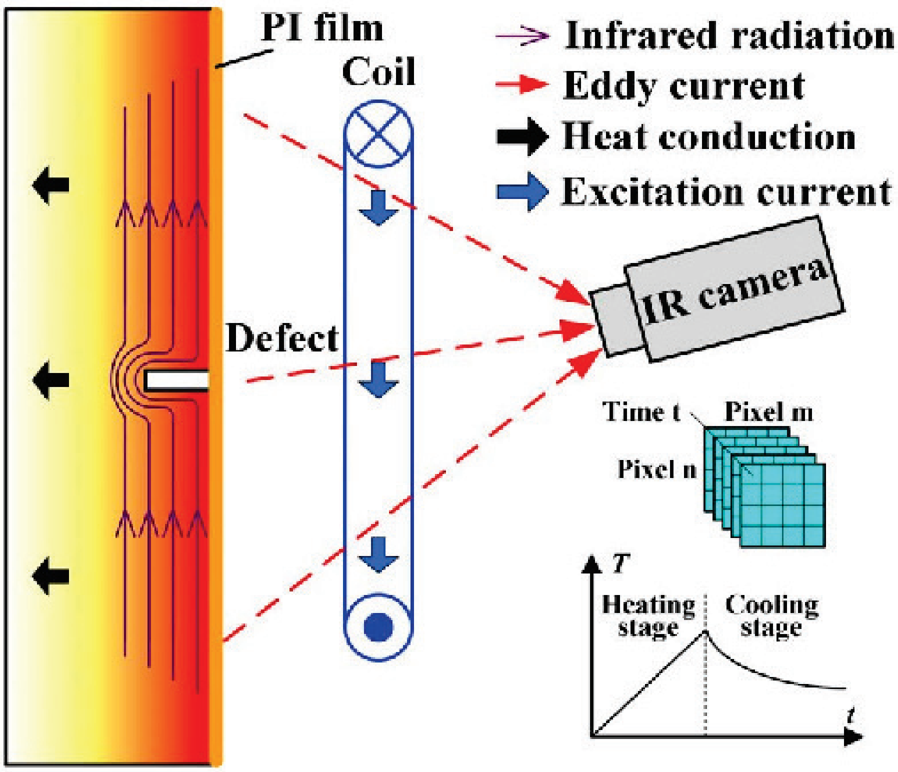

Figure 2-25 Principle of eddy current pulsed thermography system[205]

2.8.1 Simulation and modelling

The modelling and simulation of eddy current for CFRP plays a crucial role in understanding the anisotropy's influence and eliminating such influence with the optimized coil shape and the frequency. Due to the complex structure and highly anisotropic material properties of composites, the numerical model[206-208] is widely applied to the analysis and computation of eddy current, the magnetic flux of composites. However, the semi-analytical model[209-211] developed by CEA France shows its computation-inexpensive advantage. Furthermore, the change of coordinate method(CCM) integrated by this group can now solve the 3D eddy current computation in terms of the complex geometry of probe and specimen. Generally, the simulation of eddy current testing composites has developed from solving by homogenization [206]to solving by enabling anisotropy material properties[208, 212, 213], from 2D[209, 214] to 3D[214, 215]from thin plate[216] or single layer to multiple layer structure[208, 209, 211]. Due to the complex structure and highly anisotropic material properties of composites, the numerical model[206-208] is widely applied to the analysis and computation of eddy current, the magnetic flux composites. However, the semi-analytical model[209-211] developed by CEA France shows its computation-inexpensive advantage. Furthermore, the change of coordinate method(CCM) integrated by this group can now solve the 3D eddy current computation in terms of the complex geometry of probe and specimen. Generally, the simulation of eddy current testing composites has developed from solving by homogenization [206]to solving by enabling anisotropy material properties[208, 212, 213], from 2D[209, 214] to 3D[214, 215]from thin plate[216] or single layer to multiple layer structure[208, 209, 211].

2.8.1.1 Analytic modelling and simulation

Building the analytic model for simulating the electromagnetic and thermal field in layered CFRPs attracts wide attention from low frequencies (EC-NDT)[217-219] to high frequencies applications[220, 221]. The challenges in this field are to consider the multiscale of the CFRP component in terms of fibre, bundle, epoxy, and polymer, as well as the highly anisotropic properties presented by such structure. The dyadic Green function theory is used to build the analytical models for calculating the electromagnetic field in the multi-layer CFRPs[222-224]. In Ref.[224], the analytical and theoretical model to calculate the time-harmonic electromagnetic field by inducting eddy current in a uniaxial anisotropic plate is proposed. The work presents the assumption that the anisotropic CFRP plate is nonmagnetic and that the axis of uniaxial anisotropy is horizontal. Based on the above literature review, the limitations of the analytical model of eddy current testing the composites are:

1) Analytical models are limited to simple geometries. Modelling and simulating the multiple layers and textile structures require sophisticated approximation. Thus the accuracy can be reduced.
2) These models have low accuracy compared to the numerical model[224].

2.8.1.2 Semi-analytical model

The semi-analytical model is an improvement to balance the computation time and accuracy when it comes to complex geometry issues. In recent years, with the implementation of semi-analytical approaches, the CIVA platform has integrated the semi-analytical models into EC modules[225]. The previous combination of numerical and analytical approaches can address the issue of canonical geometries, e.g., planar stratified media or tubes of finite thickness[226]. The Curvilinear Coordinate Method is developed to avoid the full use of numerical methods for complex geometries [227]. The CCM is widely used for solving scattering problems of crossed gratings, and periodic structures range from the high-frequency to the low-frequency range[]. In recent days, the CCM was developed for ECT based on the planar sample[209, 211, 228], which is to simulate a 3D eddy current probe scanning a 2D layered media. The 3D ECT model based on CCM is then solved by applying the formalism to a 3D half-space sample[225, 229], shown in Figure 2-26. The merit of using CCM for complex geometries is that the calculation of mesh is not needed since all boundary conditions at each interface can be analytically described[230], which reduces the computation complexity and time. With CCM, it is possible to calculate the modal expansion of the tangential components of the EM fields in the sophisticated geometry at the interface. Besides, the anisotropic properties of the layered media can be described by the S-matrix algorithm [231, 232]. Based on the above literature review, the limitations of the semi-analytical model of eddy current testing the composites are:

1) The main difficulty for the semi-analytical approach is the numerical computation of epigenomes, which can characterise the structure since the discretization of the problem requires truncation into the Fourier domain. Thus it is still computation expensive when it comes to epigenomes.
2) There is a finite number of modes limiting the calculations of analytical shapes of samples. This method can suffer from convergence problems.

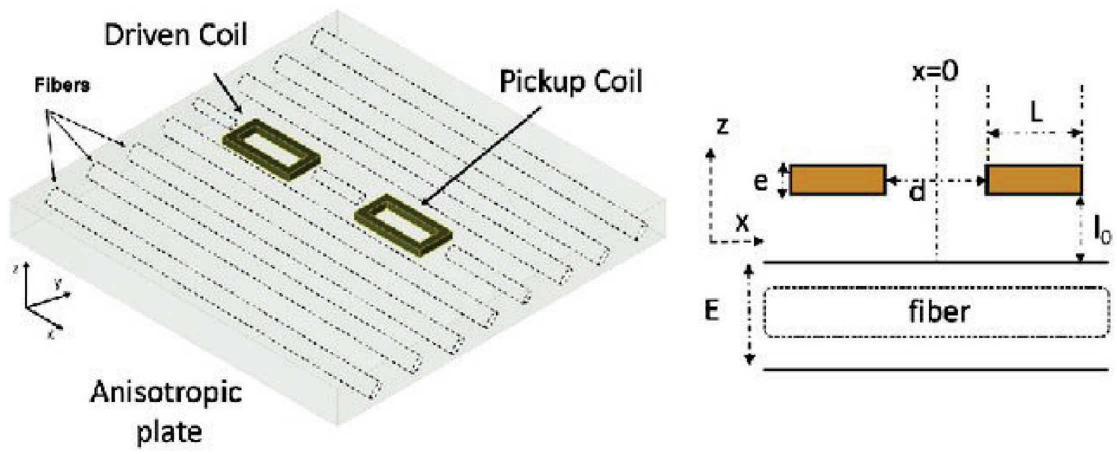

Figure 2-26 Semi-analytical model setup for planar CFRP plate[225].

2.8.1.3 Numerical model

The numerical model for ECT and ECPT is accurate and easily implemented for complex geometries. The A-V formulation based on FE(finite element)is often used [233]. In Ref.[234], the volume integral formulations were proposed to confine the discretization of source and induced eddy currents. In Ref.[235], a reduced magnetic vector potential method was proposed for ECT simulation. For volume integral formulation, it has the advantage of treating the excitation source and the sample regions separately and thus offering the flexibility to simulate sensors scanning and the multiscale dimensions in multi-layer case[236]. In Ref.[237], the integral-differential model using FE was proposed for eddy current NDT applications, and the calculation of electric vector potential is involved in the model. Then, the magnetic field is calculated based on the electric vector potential by an integral equation. Based on the above literature review, the limitations of the numerical model of eddy current testing the composites are:

1) The A-V formulation using FEM lacks the flexibility for simulating the scanning of the probe and multi-scale problem. Besides, it is time-consuming for 3-D problems when modelling the anisotropic properties is necessary[238].
2) The volume integral formulations based numerical models require a large amount of memory for space since the calculations involve full matrices.
3) In the volume integral formulations, the electric current has to be explicitly described, which leads to problems for simulating anisotropic structures, where the current density distribution is also anisotropic.

2.8.1.4 Multiscale model

The multi-scale model is developed for tacking with the simulating heterogeneous, multiscale structure of CFRP[239]. It is proposed on modelling from three different scales: the microscopic scale, which is the fibre scale; the mesoscopic scale, which is the layer scale; the macroscopic scale, which is the whole sample's scale.[240]. It is reported that in Ref.[241], the simulation of the whole material is challenging due to the scale factor between the fibre, and the composite dimensions are difficult to obtain. Thus the description of the transition from the fibre to the layer scale is implemented using a predictive homogenization method based on a statistical calculation on benchmark samples to obtain the electrical conductivity tensor of a single layer[242]. The second stage of transition from layer to specimen scales is finished by applying a multi-layer electromagnetic FEM model[243], which is illustrated in Figure *2-27*. In Ref.[244], A new multi-scale approach to predict the effective electrical conductivity tensor of a woven-fabric composite layer for frequencies lower than 10 MHz is presented, shown in Figure 2-27. However, there is still future work for the multi-scale model, such as the determination of conductivity tensor, for modelling CFRPs with defects due to the conductivity tensor of the defected area is challenging to be estimated.

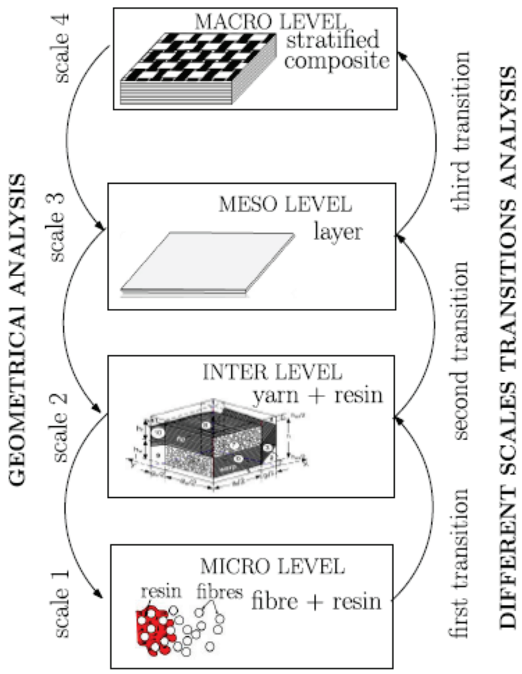

Figure 2-27 Illustration of multi-scale modelling for CFRP induction heating[245]

2.8.2 Eddy current experiment system

With the recent increase of requirement for EM NDT of CFRP, various eddy current experimental systems are developed. The eddy current technique shows its promising application on composites because of the conductive fibre in each layer, thus making electromagnetic wave penetrating the material with different depths by different frequency excitation. In this section, four eddy current systems: high frequency, low frequency, pulsed eddy current, and eddy current pulsed thermography system is reviewed.

2.8.2.1 High-frequency eddy current

The high-frequency eddy current refers to the use of EM wave with frequency ranging from 3 MHz to 100 MHz. With high-frequency excitation, a strong and focused eddy current can be generated within the skin-depth of the material and characterising the defects on a microscopic scale with reasonable resolution[246]. In Ref.[247], the HF ECT with 10 MHz excitations was developed to characterise the fibre orientation and various local defects such as matrix cracks, delamination, and impact damage. The state-of-art HF ECT system was developed in Fraunhofer Institute IZFP[19, 248, 249] called as EddyCus® CF map, which has the highest frequency of 100 MHz. The 3D ECT imaging scanner is shown in Figure 2-28. The instruments enable the fast inspection of the CFRP laminate during the manufacturing process. Despite some evident advantages, high-frequency eddy current testing still has limitations, such as the HF excitation has high sensitivity but also suffers from low SNR due to higher levels of noise as the system is more susceptible to lift-off and surface conditions of the sample[250].

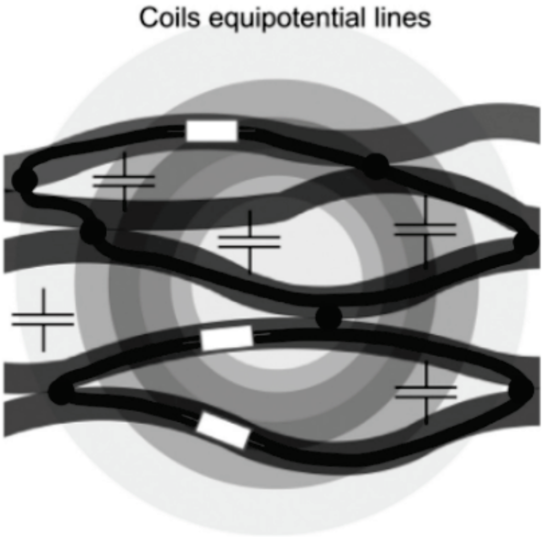

(a)

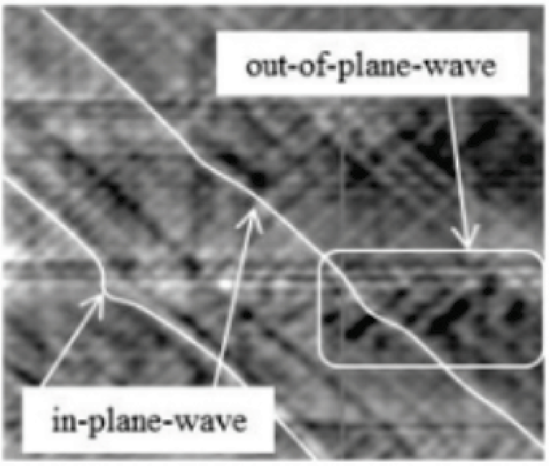

(b)

Figure 2-28 High-frequency scanner for CFRP orientation evaluation in Fraunhofer IKTS[13]

(a) Equivalent circuit model of contact fibres in high-frequency mode, (b) in-plane wave, and out-of-plane waviness detected by high-frequency mode.

2.8.2.2 Low-frequency eddy current

The low-frequency ECT inspection refers to the operation between 100 Hz and 1 MHz. It has the advantage of being robust to environmental noise and the shift to electrical resonance[250]. In [251, 252], the low-frequency eddy current system HTS-SQUID (High-Temperature Superconducting Quantum Interference Devices) magnetometer was proposed. In Ref.[253], the feasibility of the low-frequency eddy current system was explored. A small-size T-R type of probe was designed to improve the point spread function, which is shown in Figure 2-29. For low-frequency eddy current detecting on composites, limitations are the influence of lift-off variance on probe signal and low speed of ECT detection due to slow response.

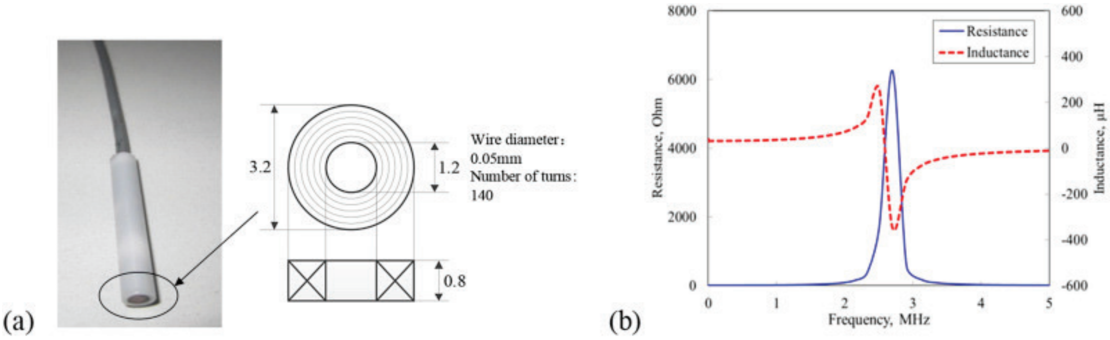

Figure 2-29 The implementation of low-frequency eddy current system[253]

(a) coil dimensions, (b) resistance, and inductance versus frequency.

2.8.2.3 Pulsed eddy current

The pulsed eddy current (PEC) sensing has been developed for metallic subsurface crack detection in recent years[254-257]. In Ref.[189], it was also applied for the detection of delamination in CFRP in recent development. The principle of PEC is to excite the probe with a broadband pulse, which can be a square wave in most cases[189]. The transient eddy current generated in the sample is related to magnetic pulses propagating into the material[258]. In PEC testing, the pulse excitation consists of a broad frequency spectrum. Thus the reflected signal containing the broadband spectrum is related to important depth information. In Ref.[259], the peak values and peak times of the transient current response have been used for defect detection and depth quantification. The latest development in PEC includes the reduction of lift-off influence[260], the detection of defects in multi-layered structures [261], honeycomb structure [189]. In Ref.[78], the improvement of PEC's sensitivity is achieved by detecting asymmetries in the transient PEC response signal response. However, to achieve the further application of PEC for CFRP, the system should be improved by the analysis of the frequency domain compared to the conventional eddy current method as well as the dispersive magnetic field affected by the heterogeneous structure, which reduced the sensitivity for CFRP QNDE.

2.8.3 Feature extraction for eddy current and eddy current pulsed thermography

The further application of ECT and ECPT was hindered by the anisotropy of the CFRP's structure in each layer, influencing the evaluation of defects in CFRP. Besides, the layered structure results in the damping of the thermal wave, which decreases the signature of the defect. To minimize the disturbance brought by the heterogeneous structure, feature extraction methods for QNDE are required.

Based on the ECPT, thermal image sequences that can be used to identify defective areas are captured and recorded by the infrared camera. The characteristics of CFRP specimens are represented by heat distribution, and the transient thermal image at different times contains different physical properties(e.g., [262]. So thermal image processing methods are pivotal to extract features of defects. At present, the PCA[154, 263, 264], ICA[154], Fourier transform[265], and wavelet [266] have been applied in thermal image analysis for defect identification. In Ref.[263], the PCA feature extraction is conducted by comparing the efficiency image-based or temporal profile-based decomposition. In Ref.[267], the Tucker decomposition-based signal reconstruction is proposed to detect and evaluate the impact damage of CFRP. In Ref.[266], the wavelet transform is applied to analyze the best thermal image, which was selected, having the most significant high-frequency wavelet energy.

In ECPT testing, the eddy current accumulation area induced by the defect can be observed visually by thermal imaging. But the improper selection of thermal images and image processing algorithms influences the **defect classification and identification** and NDT&E performance of ECPT. In Ref.[268], the neural network is applied to distinguish temperature increase between the crack and sound areas. In Ref.[269], the exponential point spread function for deblurring the linear motion influence on the thermal image is proposed. In Ref.[270], the cosine transformation-based separation and Mexican hat wavelet were used to reduce the effect of different emissivity values at edges, corners, or surface parts and achieve automatic defects localization. In Ref.[200], the thermographic signal reconstruction is applied to solve the non-uniform heating and background reference location. In Ref.[271], the principal component analysis(PCA)based method to separate different thermal patterns without using any training knowledge is introduced. In Ref.[272], the independent component analysis(ICA)-blind source separation is applied to separate spatial temperature into independent signal images. In Ref.[154, 273], a spatial-transient-stage tensor mathematical model and the Tucker decomposition algorithm are used to characterise and track the variation of properties. In Ref.[274, 275], the pulsed inductive thermal wave radar is applied to reduce emissivity variation and increase the detectability of subsurface defects. In Ref.[153], the wavelet transform and principal component analysis are integrated to identify low energy impact damages of CFRP. Quantitative detection of fibre breakage[276], matrix breakage defects by NDT techniques should be conducted due to BVID causing delamination and fibre breakage in the internal structure. The defect size, location, depth remain challenging determined due to the quasi-isotropic structure resulting in complex and multiple physics[277].In the testing of induction thermography on composites[274], the un-uniform heating is generated due to the anisotropic thermal conductivity thus reducing the SNR in IR camera[244, 278] which proves the importance of the elimination of un-uniform heating essential by varied kinds of feature extraction methods, such as phase image analysis[278], optical flow[279], principal component analysis and independent component analysis[154].

2.8.4 Specimen and applications

This section mainly reviews the samples used in the community for ECT and ECPT system, which is detailed introduced in Table 2-1.

For ECT testing, in Ref.[280], the ECT is applied for CFRP testing. The results illustrate that fibre breakage with or without matrix cracking can be detected using the variations in fibre volume fraction. In Ref.[189, 281], the detection of low energy impact damage (0.25 J) in CFRP materials was achieved. Besides, in Ref.[280], the characterisation of eddy current testing using HTS (high-temperature superconductivity) was presented for QNDE of impact energy less than 2J in CFRP laminate

For eddy current pulsed thermography testing, Most of the work came from the team at Newcastle University. They have successfully applied the ECPT system for the detection of surface crack[282], the relationship between temperature response and widths and depths have been concluded. As for impact damage, in their work, 10j and 12j of impacts can be detected with the thermography method and act as the shape of a circle, while areas of 6j and 8j by impacts are concentrated, energy less than 4j cannot be detected[154]. The delamination of CFRP can also be observed on IR camera through the work [40] that man-made delamination at 155μm, 310μm, 775μm, and 930μm deep have been observed through the new developed PEC-stimulated thermography and fibre orientation for surface and subsurface layers can be observed, giving the potential for minor defect detection, for example, fibre breakage. In recent years, the ECPuCT system (eddy current pulse compression thermography) was developed for CFRP QNDE with better accuracy and sensitivity. The delamination of different depths, debonding at the same depth with different properties, and the different orientations in the unidirectional sample were evaluated by the proposed system[1, 258, 283].

Table 2-1 Review of CFRP samples used for ECPT and ECT

Research group	time	Specimen	Defect type
Tian, G.Y. et al	2011 [282]	12 layer sample CFRP	Surface notches with width (0.1, 0.5, 1, or 2 mm) and depth (0.5, 1, or 2 mm)
	2011[284]	20-layered CFRP samples	Delamination is manufactured at the interface of 1st-2nd, 2nd-3rd, 5th-6th, 6th-7th, 9th10th, and 10th-11th layers
	2013[279]	12 layer sample CFRP	Barely invisible impact damage 2J-12J
	2014[189]	Honeycomb sandwich structure	Insert defects
	2016[285]	CFRP samples with 12 layers of 5HS carbon fibre woven with balanced woven fabric	Barely invisible impact damage 2J-12J
	2019[1]	12 layer CFRP	Teflon delamination
	2019[283]	Epoxy bonded CFRP	Brass, release film and release agent inclusion on the bonded line
	2019[145]	Complex geometry CFRP sample	Teflon inclusion
	2020[258]	Two-layer unidirectional CFRP	No defects, the sample is used for validation of FEM and semi-analytical model
H. K. Bui. et al	2018 [242]	Unidirectional CFRP plate	No defects. The sample is used for model validation

	2019[286]	6 layer 5H-satin carbon-fibre epoxy composite laminate plates	Debonding inclusion: Brass, release film and release agent inclusion on the bonded line
Henning Heuer. et al	2011[249]. 2016[248]	Multidirectional RCF materials	missing fibre bundles, lanes, fringes
Jin Q. et al	2017[253]	Honeycomb sandwich structure	Point like defect
Nihon University, Japan	2011[287], 2013[276]	Cloth CFRP, woven CF sheets. Unidirectional fibre CF sheets	0.25, 0.5, 0.75, 1.0, 1.5, 2.0 J impact damage

2.9 Challenges of NDT&E for CFRP

The challenges of further applications of various NDT&E for CFRP were the complexity of composite materials in terms of the multi-layer, anisotropic conductivity, and heterogeneous structure. There exists an urgent need for substantial further work to conduct NDT&E and SHM of CFRP components quantitively. It is illustrated in Figure 2-30 that various NDT methods, including ECT, UT, AT, and X-ray, are not solely capable of detecting and quantifying all defects and failures in composite materials

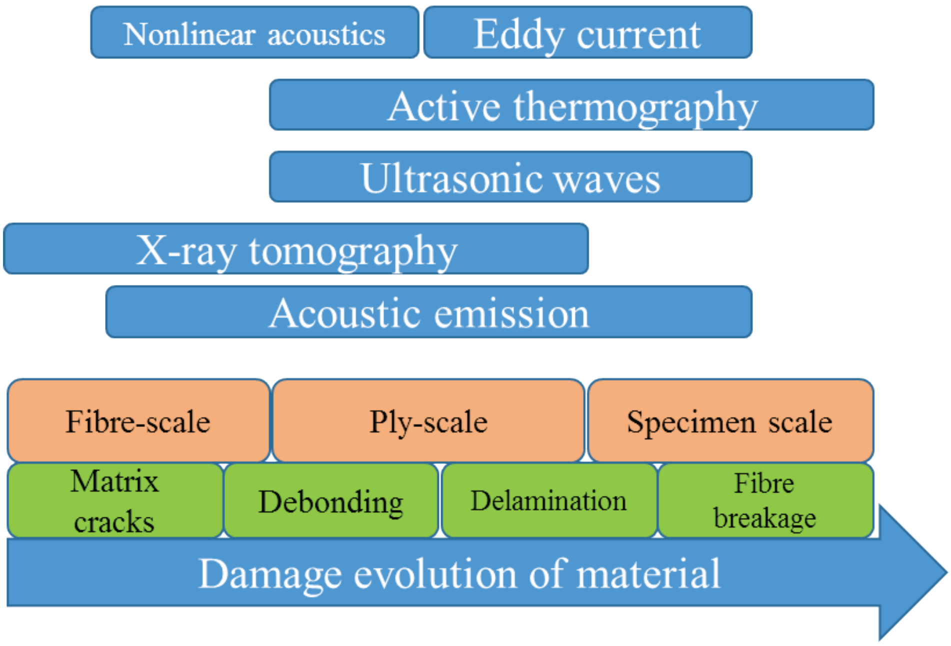

Figure 2-30 Applicability of different NDT techniques for defects of different scales

2.9.1 Challenges of ECPT for CFRP

Since ECT and ECPT are major topics of the thesis, based on the literature review in Section 2.6, challenges and problems of ECPT and ECT for CFRP are identified as follows:

1) Multi-layer modelling and simulation for CFRP: the multi-layer issue presents challenges for interface modelling, which are crucial for describing the scattering electromagnetic and thermal field in the structure. In addition, the functionality of the forward model was not fully explored in terms of parameter estimation, inversion, and reconstruction, which is urgently required for model-based QNDE techniques.
2) The current ECPT system has limitations when a non-uniform heating pattern affects the signature of defect and failure, creating the urgent need for defect location using feature-based techniques for non-uniform heating pattern removal for defect signature feature extraction.
3) The detection and evaluation of subsurface defects in CFRPs can be challenging due to the low SNR transient response, which can be improved by the combination of pulse compression techniques for enhancing the detectability of subsurface defects of the ECPT system.
4) The feature-based QNDE approaches have limitations when the sample has a single parameter to be estimated, for example, electrical, thermal conductivity as well as fibre orientation in the CFRPs. Thus, reconstruction based QNDE techniques are required for the parameter estimation and reconstruction in terms of optimisation between forward model and experimental data.

2.10 Chapter summary

In this chapter, the literature review of defects in CFRPs, state-of-art NDT techniques including phased array, guided wave, active thermography, eddy current and eddy current pulsed thermography, as well as the post-processing techniques, were discussed. Based on the review, the current challenges and issues of eddy current pulsed thermography for CFRPs NDT were identified and highlighted in section 2.7.

Chapter 3 Methodology introduction

To tackle with challenges identified in chapter 2 for NDT&E of CFRPs, this chapter presents the methodology developed in the PhD study, which is shown in Figure *3-1*, including the electromagnetic heating of CFRP, the numerical modelling of the multi-layer CFRP using finite element modelling, the proposed ECPuCT system, and the feature extraction techniques used for post-processing of the transient response.

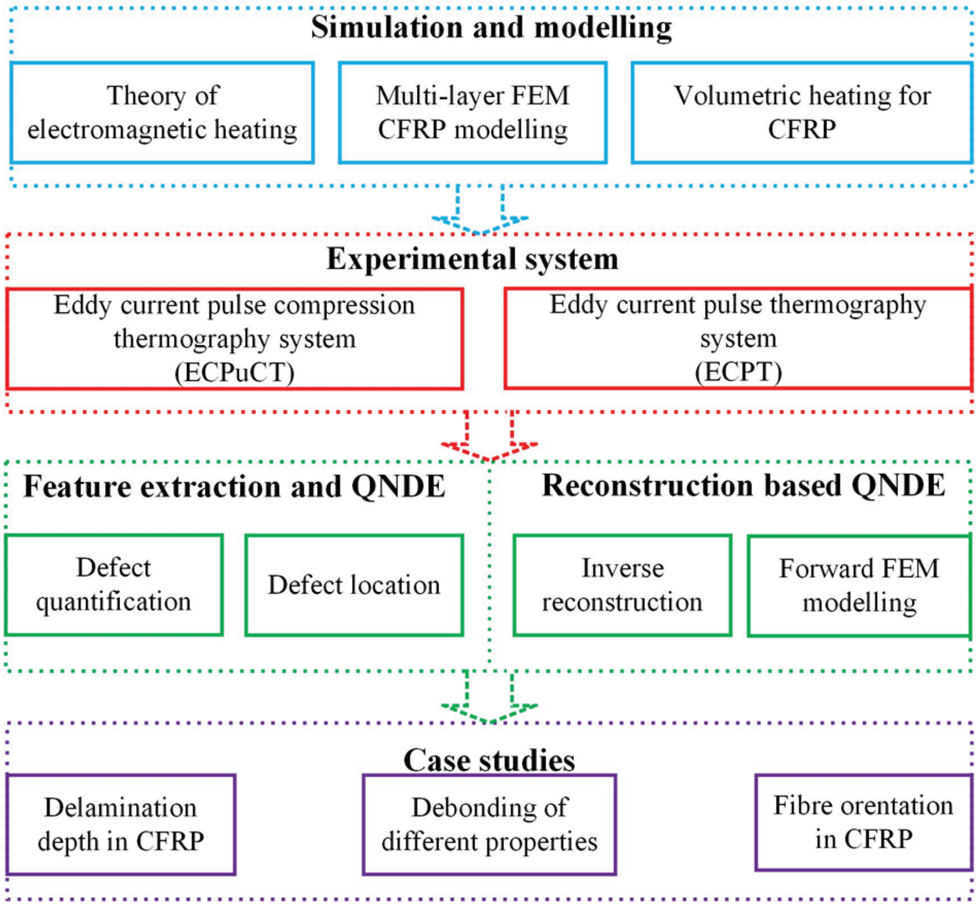

Figure 3-1 System diagram of the proposed methodology

3.1 Simulation and modelling of electromagnetic heating for CFRP

3.1.1 Fundamentals of Electromagnetic Heating

The principle of eddy current pulsed thermography involves two physics: electromagnetic heating and thermal diffusion. In this section, the multi-physics process is detailed, illustrated in Section 3.1.1 and Section 3.1.2, respectively. The two physical phenomena are combined to evaluate the components' electrical and thermal properties. In the heating and cooling stage of the ECPT experiment, the heating stage is dominated by the electrical conductivity of the material, while the cooling stage response can characterise the thermal conductivity of the material.

3.1.1.1 Electromagnetic Heating

At the beginning of EM heating, the EM wave generated by the coil propagates into the tested sample. The propagation of the EM wave can be solved by Maxwell's equation. In these equations, six EM parameters are linked together, including ***E, D, H, B, J.*** Among these, ***E*** denotes the electrical field, ***D*** represents the electrical displacement, ***H*** is the magnetic field, ***B*** is the magnetic induction, and ***J*** is the current density. The description of Maxwell can be in the differential form or integral form. The differential forms are usually solved for Finite Element Modelling. Thus the Maxwell equation can be written as follows:

$$\nabla \times H = J + \frac{\partial D}{\partial t} \tag{3.1}$$

$$\nabla \times E = -\frac{\partial B}{\partial t} \tag{3.2}$$

$$\nabla \times D = \rho \tag{3.3}$$

$$\nabla \times B = 0 \tag{3.4}$$

Among the above equations, the Maxwell-Ampère's law is denoted by equation (3.1), the equation (3.2) describes Faraday's law, which together describes the coupling process of the EM wave. Equations (3.3) and (3.4) is the Gauss'law for electrical and magnetic form calculation, which describe the flux conservation of magnetic and electrical field. Besides, the combination of equations (3.1) and (3.3) can lead to the calculation of electrical charge conservation as follows:

$$\nabla \times \mathrm{J} = -\frac{\partial \rho}{\partial t} \tag{3.5}$$

The equations (3.1) to (3.5) describe the differential form of Maxwell's equations for FEM calculation. To apply these equations for EM wave propagation in specify material, constitutive relationships of material properties should be added as follows:

$$J = \sigma E \tag{3.6}$$

$$D = \varepsilon E \tag{3.7}$$

$$B = \mu E \tag{3.8}$$

The σ denotes the electrical conductivity, ε is the electrical permittivity, and μ is the magnetic permeability, which are macroscopic properties of the specified material.

The eddy current pulsed thermography system is involved with the time-harmonic EM field for a specified material. Thus, according to the above derivations, the calculation of ***H*** field and ***E*** field for the time-harmonics situation is obtained as follows:

$$\nabla \times H = J + j\omega D \tag{3.9}$$

$$\nabla \times E = -j\omega B \tag{3.10}$$

Where j denotes the imaginary part, and ω is the angular frequency of time-harmonic EM wave.

Thus, with the combination of equations (3.6) to (3.8) and time-harmonic calculations from equations of (3.9) and (3.10), the calculation can be as follows:

$$\nabla \times \frac{1}{\mu} B = \sigma E + j\omega\varepsilon E \tag{3.11}$$

Then, with the consideration of magnetic vector potential and electrical scalar potential, the equation (3.10) can be updated as follows:

$$\nabla \times \frac{1}{\mu} \nabla \times A = \sigma(-\nabla V - j\omega A) + j\omega\varepsilon(-\nabla V - j\omega A) \tag{3.12}$$

Where ***A*** is the magnetic vector potential, and ***V*** is the electrical scalar potential. Equation (3.10) can be further refined as:

$$(j\omega\sigma - \omega^2\varepsilon)A + \nabla \times \frac{1}{\mu}\nabla \times A + \nabla V(\sigma + j\omega\varepsilon) = 0 \tag{3.13}$$

It is noted that in equation (3.13) that A and V are coupled together. With the implementation of gauge information, it can be further refined to the function of A as follows:

$$(j\omega\sigma - \omega^2\varepsilon)\tilde{A} + \nabla \times \frac{1}{\mu}\nabla \times \tilde{A} = 0 \tag{3.14}$$

Thus, the electrical field and the magnetic induction can be calculated as follows:

$$B = \nabla \times \tilde{A} \tag{3.15}$$

$$E = -j\omega A \tag{3.16}$$

During the process of induction heating, the electromagnetic heating source is defined as the Joule power density[288]:

$$P_\sigma = \int_{vol^-}^{vol^+} \sigma E^2 dv \tag{3.17}$$

Where vol denotes the enclosed volume of material and P_σ is the Joule heating souce.

3.1.1.2 Thermal Diffusion

With the obtained eddy current density in equation (3.17), the heat transfer in the solid medium can be expressed as follows:

$$\rho C_p \frac{\partial \mathrm{T}}{\partial \mathrm{t}} + \rho C_p \mathrm{v} \cdot \nabla T + \nabla \cdot q = p_s \tag{3.18}$$

ρ and C_p denotes the density of the material and heat capacity, respectively. T is the temperature of material as a function of spatial coordinates and time. v is the velocity vector, where it can be neglected in the ECPT setup since the coil and sample are a fixed distance against each other. q denotes the heat flux at the specified boundary of material. p_s is the induction heating power calculated by equation (3.18).

With the introduction of thermal conductivity λ into equation (3.18), where:

$$q = -\lambda \nabla T \tag{3.19}$$

It can be refined as follows:

$$\rho C_p \frac{\partial \mathrm{T}}{\partial \mathrm{t}} - \lambda \nabla^2 T = p_s \tag{3.20}$$

$$\rho C_p \frac{\partial \mathrm{T}}{\partial \mathrm{t}} - \lambda \nabla^2 T = \sigma E^2 \tag{3.21}$$

Equation (3.21) is the thermal diffusion process with coupling electromagnetic heating as a source.

3.1.2 Volumetric heating for CFRPs using ECPT

The theory of ECPT on ferromagnetic material has been addressed in the last section and researches [289-291]. The principle of ECPT for CFRP is different from that of ferromagnetic materials, concerning both the heating mode and the thermal wave diffusion pattern. According to Eq. (3.22), the penetration depth δ of an electromagnetic wave into a conductive material has a monotonic decreasing relationship with increasing current frequency:

$$\delta = \frac{1}{\sqrt{\pi \mu \sigma f_{carrier}}} \tag{3.22}$$

where $\mathrm{f_{carrier}}$ is the frequency of the excitation current [Hz], σ is electrical conductivity $[\mathrm{S \cdot m^{-1}}]$, and μ is magnetic permeability$[\mathrm{H \cdot m^{-1}}]$. In general, for CFRP, the bulk conductivity σ value is in the order of 15000 $[\mathrm{S \cdot m^{-1}}]$ and it is non-magnetic [153]. Considering an $\mathrm{f_{carrier}} = 300$ [kHz], the corresponding penetration depth is 7.5 [mm] while for the same value of $\mathrm{f_{carrier}}$, the penetration depth in steel ($\sigma = 9.93 \times 10^6$ [S/m], $\mu = 3.77 \times 10^{-4}$ [H/m]) is equal to 29.08 [μm], which is significantly smaller than one obtained for CFRP. Thus, since the thickness of the CFRP sample is often lower than the corresponding value of δ, the heating mode is volumetric.

The heating depth of the eddy current has an exponential decay in the through-thickness direction. Therefore, the heat generated through the Joule effect at a different layer of composites decays exponentially through the perpendicular direction.

The thermal response in CFRP can be recognized as a sum of thermal waves. Each of them has a different frequency f, thermal diffusion length μ, and diffusion velocity v. According to thermal wave theory, μ can be expressed in Eq. (3.23) as:

$$\mu = \sqrt{\frac{k}{\pi f \rho C}} = \sqrt{\frac{\alpha}{\pi f}} \tag{3.23}$$

Where k is thermal conductivity, ρ is density $[\mathrm{g.m^{-3}}]$, C is heat capacity $[\mathrm{J.g^{-1}.K^{-1}}]$, and α is the thermal diffusivity $[\mathrm{W.m^{-1}.K^{-1}}]$. The diffusion velocity v can be obtained as:

$$v = \sqrt{4\pi f \alpha} \tag{3.24}$$

Equations (3.23) and (3.24) indicate that thermal waves having higher frequencies diffuse faster but shallower, while low-frequency thermal waves diffuse slower but more in-depth into the sample. If there is a defect, the parameters (like amplitude and phase) of the thermal wave change, thus allowing the flaws to be detected by an InfraRed (IR) camera.

In the case of volumetric heating, the ECPT characterisation can be either in transmission or reflection mode. The transmission and Reflectionarrangements are depicted in Figure 3-2(a). If the thermal diffusion length μ is greater than depth d at which the delamination/defect is possibly buried, the response from the defect can be observed through the acquired surface temperature field. The unique advantage of volumetric heating compared to the surface heating scenarios (e.g., as in the case of light-stimulated thermography) comes from the direct interaction between the buried defect and the induced eddy current field, see Figure 3-2(b). In surface heating mode, the generated thermal wave must be reflected by the defect, taking twice the time with respect to the volumetric heating mode before being recorded by the IR camera. Overall, the heating pattern of the EC excitation in transmission arrangement can be considered as follows: firstly, the whole specimen is heated up by the induced eddy current and Joule's effect [153]. Then, the defected area is heated more than the sound areas at the same depth. The information needed for characterising the defects comes from the thermal wave travelling from the defected area at a depth d, as shown in Figure 3-2(a), where t_r and t_d represent the travelling time of the thermal response from defect to the surface in transmission and reflection mode respectively.

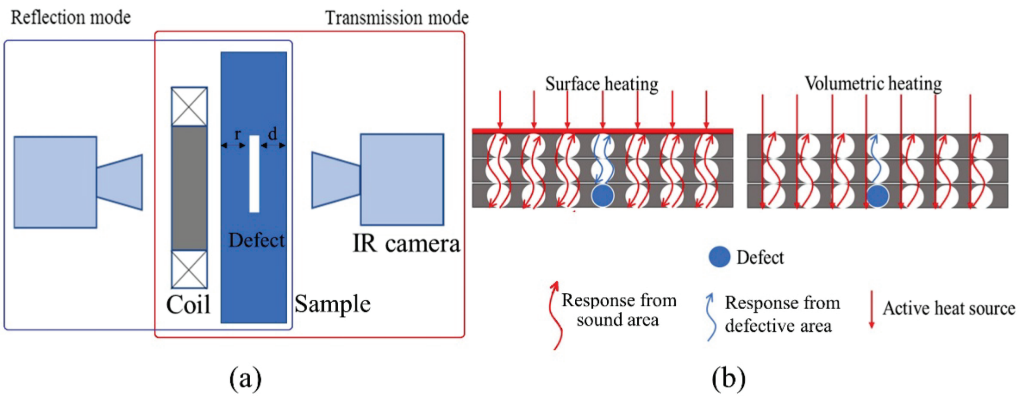

Figure 3-2 Eddy current pulsed thermography measurement modes

(a) Configuration of transmission mode and reflection mode: (b) Comparison of Surface heating and volumetric heating

3.1.3 Multi-physics numerical modelling using the finite element method

To understand the electromagnetic and thermal behavior of the eddy current pulsed thermography, modelling is needed. The current challenges for modelling ECPT are the anisotropic conductivity of the material [6]. The electrical conductivity of CFRPs depends strongly on the orientation of carbon fibres: the longitudinal conductivity (parallel to the fibre direction, σ_L) is the highest; while the transverse conductivity (perpendicular to the fibres, σ_T) is relatively lower and on the same order of σ_{Th}[292]. Additionally, this anisotropic electrical conductivity is further compounded by a strong dependence on the presence of interfaces between adjacent plies. These interfaces vary in size, physical composition, and chemical composition and therefore result in uncertain value [293]. Besides, σ_{Th} (according to the thickness of CFRP laminates) can be significantly affected by the presence of interfaces between layers and the lamination of the individual plies. For instance, the stacking sequence tends to increase the dispersion of measurements [294].

Due to the important number of carbon fibres impregnated in each layer, it is very difficult to take into account the real geometry in the simulation. The composite layer is then replaced by a homogenized one [240]. Moreover, as the composite sheets have a small thickness compared with their other dimensions, shell elements can be used to reduce the number of unknowns. The case of three-dimensional (3-D) induction heating simulation of the CFRP plate with equivalent anisotropic conductivities has been presented [241]. In the meantime, CEA LIST has recently developed a new semi-analytical method for the computation of the 3D primary fields induced by an eddy current probe in a homogeneous conductor presenting a local perturbation of the geometry [211]. This approach is an extension of the curvilinear coordinate method (CCM), which is efficient for the computation of the fields scattered by 2D diffraction gratings enlightened by a plane wave or perfectly conductive random surfaces [295, 296].

In this thesis, the 3-D induction heating simulation model of a multi-layer anisotropic composite material is proposed. The real geometry of multi-layer composite materials with an equivalent anisotropic individual layer is considered. A global equivalent model is then introduced to consider the different fibbers' orientations. Note that this model is an extension of previous works presented in [245, 297]. The interface algorithm is a recursive routine that aims at linking all the intermediate interfaces to computing the global structure, thus leading to a black box representation of the global structure, including all the internal reflections. We refer the reader to [297] for a more insightful on the interface model concerning both numerical schemes and implementation.

To model the anisotropic behaviour of composite materials, electrical and thermal conductivities (σ_i, λ_i) can be written as for the following equation (3.25) and(3.26) [240]:

$$\sigma_i = \begin{bmatrix} \sigma_{xx_i} & \sigma_{xy_i} & 0 \\ \sigma_{yx_i} & \sigma_{yy_i} & 0 \\ 0 & 0 & \sigma_{z_i} \end{bmatrix} \quad (3.25)$$

$$\lambda_i = \begin{bmatrix} \lambda_{xx_i} & \lambda_{xy_i} & 0 \\ \lambda_{yx_i} & \lambda_{yy_i} & 0 \\ 0 & 0 & \lambda_{z_i} \end{bmatrix} \quad (3.26)$$

The electrical and thermal conductivity are functions of layer orientation θ along with fibre axis, as shown in Figure *3-3*(b). If the orientation of each layer is changed, the conductivity can be calculated as follows in equations (3.27) and (3.28).

$$\sigma_\theta = \begin{bmatrix} \sigma_L \cos^2\theta + \sigma_T sin^2\theta & \frac{\sigma_L - \sigma_T}{2} sin2\theta & 0 \\ \frac{\sigma_L - \sigma_T}{2} sin2\theta & \sigma_T cos^2\theta + \sigma_L sin^2\theta & 0 \\ 0 & 0 & \sigma_T \end{bmatrix} \tag{3.27}$$

$$\lambda_\theta = \begin{bmatrix} \lambda_L cos^2\theta + \lambda_T sin^2\theta & \frac{\lambda_L - \lambda_T}{2} sin2\theta & 0 \\ \frac{\lambda_L - \lambda_T}{2} sin2\theta & \lambda_T cos^2\theta + \lambda_L sin^2\theta & 0 \\ 0 & 0 & \lambda_T \end{bmatrix} \tag{3.28}$$

where θ denotes the orientation of the layer, σ_L, σ_T denote the electrical conductivity in longitudinal and transverse direction respectively, λ_L, λ_T the thermal conductivity in the longitudinal and transverse direction. Note that the conductivity will be estimated in n chapter 6 and that a comparison of the estimated electrical and thermal conductivity with true values can be found in Ref. [298].

As shown in the second block Figure *3-3*(a), for a number N of layers of laminated composite, each layer i's magnetic field can be calculated as (3.29):

$$\begin{cases} \frac{d^2 H_x(z)}{dz^2} - j\omega\mu \cdot \sigma_{yy_i} H_x(z) = j\omega\mu \cdot \sigma_{yx_i} H_y(z) \\ \frac{d^2 H_y(z)}{dz^2} - j\omega\mu \cdot \sigma_{xx_i} H_y(z) = j\omega\mu \cdot \sigma_{xy_i} H_x(z) \\ \frac{d^2 H_z(z)}{dz^2} - j\omega\mu \cdot \sigma_{z_i} H_z(z) = 0. \end{cases} \tag{3.29}$$

The boundary conditions of the magnetic field are as follow in equation (3.30):

$$\begin{cases} H\left(\frac{p_i}{2}\right) = H_i \\ H\left(-\frac{p_i}{2}\right) = H_{i+1} \end{cases} \tag{3.30}$$

where p_i represents the thickness of layer i.

According to Faraday's law combined with the local form of Ohm's law, the interface to determine anisotropic electrical field from one layer to the next can be obtained as follow in equation (3.31):

$$\begin{pmatrix} E_i \\ E_{i+1} \end{pmatrix} = k \times \begin{pmatrix} \alpha_i & -\beta_i \\ \beta_i & -\alpha_i \end{pmatrix} \begin{pmatrix} H_i \\ H_{i+1} \end{pmatrix} \tag{3.31}$$

where k is the normal vector and α_i, β_i are scalar values dependable on electrical conductivity shown in equations (3.22) and (3.23) and can be calculated. Note that this procedure is also shown in the third block in Figure *3-3*(a).

After having obtained the current density E_i of layer i the heat source Q_i in layer i can be obtained as shown in the fourth block of Figure 3-3(a), of which the calculation process is shown in equations (3.32) and (3.33):

$$Q_i = J_i^T \cdot E_i = J_i^T \cdot \sigma_i^{-1} \cdot J_i \tag{3.32}$$

$$J_i = rotH(i) \tag{3.33}$$

After the calculation of Q_i of each layer, the heat transfer by radiation is neglected in the thermal analysis due to the short heating stage and low temperature rise during a real ECT test. Therefore, heat conduction is the main type of heat transfer. The governing equation of temperature field is shown in the fifth block of Figure *3-3*(a), and it is described in equation (3.34) as:

$$\rho_i C_{p_i} \frac{\partial T}{\partial t} - \lambda_i \cdot \left(\frac{\partial^2 T}{\partial x^2} + \frac{\partial^2 T}{\partial y^2} + \frac{\partial^2 T}{\partial z^2} \right) = \int Q_i(x, y, z, t), in\ \Omega_1 \tag{3.34}$$

with the boundary condition in equation (3.35).

$$-\lambda_i \cdot \frac{\partial T}{\partial t} = h(T - T_a) \tag{3.35}$$

where λ_i is obtained from Eq. (3.23), ρ_i is the material density, C_{p_i} is the specific heat, h is the convective coefficient, Ω_1 refers to the whole conductive layer, T is the temperature of layer i and T_a is the room temperature.

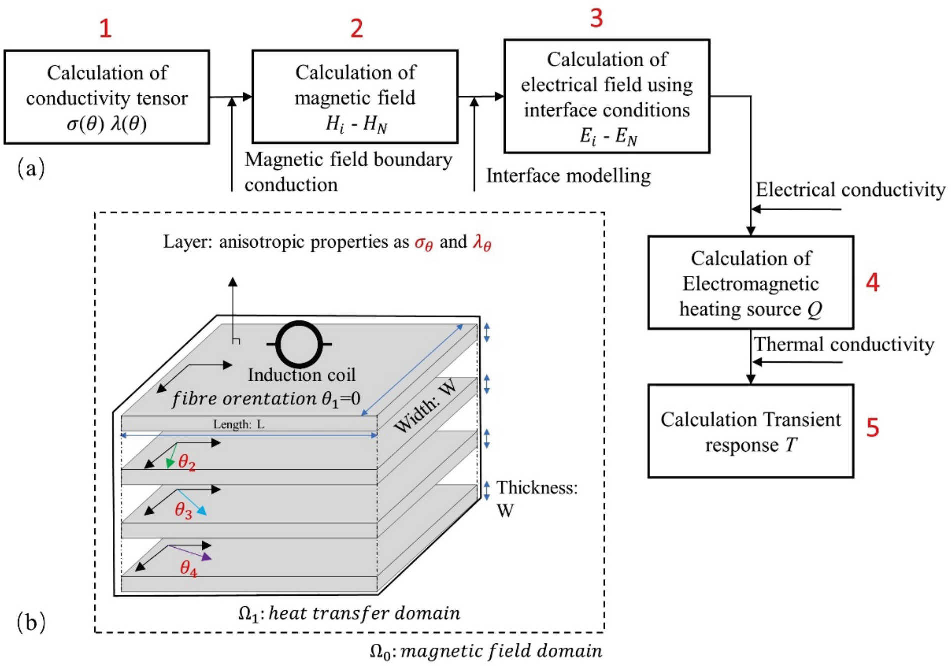

Figure 3-3 Multilayer CFRP modelling approach

(a) illustration of the process for FEM calculation, (b) representation of multi-layer composites with different orientations using FEM and interface

3.2 Experimental system of eddy current stimulated thermography

In this thesis, two experimental systems are proposed and applied for the CFRP NDT&E. The traditional eddy current pulsed thermography system and the newly proposed eddy current pulse compression system. The ECPT system refers to the application of square pulse excitation for the modulation eddy current of fixed frequency. In this case, the scanning is finished in square pulse(50 ms to 200 ms pulse width). Thus, it is capable of achieving fast scanning of a large area in a short time. However, the detectability of the ECPT system can be reduced when it comes to the QNDE of the subsurface defect in inhomogeneous material, e.g., delamination in CFRP. The eddy current pulse compression system is developed for this reason to modulate the excitation and delivering much more power to the sample, which achieves greater detectability for the subsurface defect.

3.2.1 Eddy current pulse thermography system

The traditional ECPT system is illustrated in Figure *3-4*. The system can generate high power currents on the sample using induction heating. The synchronization between the induction heater and the thermal camera is achieved using a signal generator, generating a square pulse. The thermal camera then captures the fixed duration (usually 1 second) of the induction heating process. The video of heating and cooling of the sample is later transmitted to the PC using an ethernet connection. With the data obtained, the visualization/feature extraction and quantification process are implemented in MATLAB.

The specification of the induction heating module is the Easyheat 224 Cheltenham Induction Heating for exciting the sample. The module can achieve maximum induction heating power of 2.4 kW as well as 400 A current with the carrier frequency ranging from 50 kHz to 400 kHz. Such high frequency of excitation can enable reasonable thermal contrast between defect and sound areas. Additionally, the system only requires 5 ms response time to reach the maximum power, which is experimentally validated.

The specification of the thermal camera FLIR A655sc is presented in Table 3-1. The camera has temperature accuracy is $\pm 2^{\circ}\mathrm{C}$ with a maximum spatial resolution of

640×480. The maximum frame rate is 200 FPS. The detector pitch is 17 μm. The spectral range is 7.5-14 μm, and the detector time constant is approximately 8 ms.

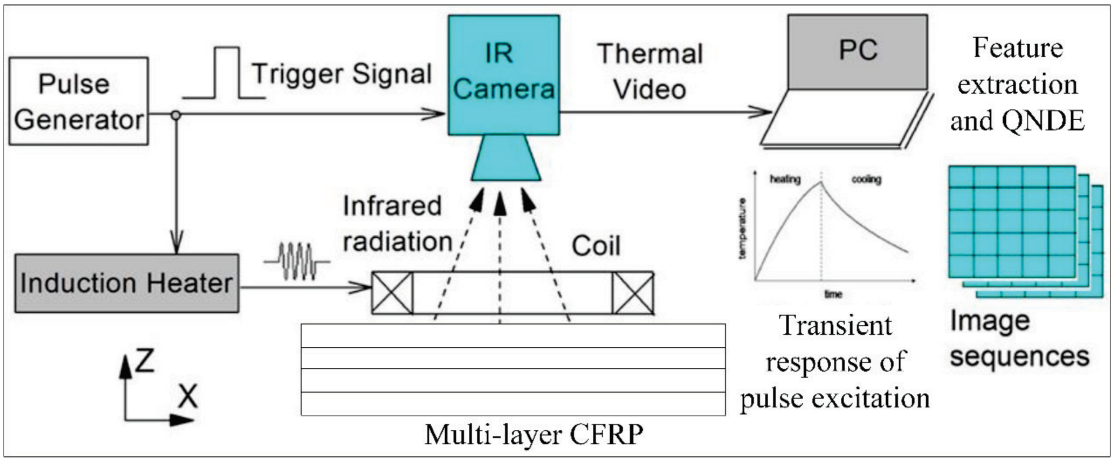

Figure 3-4 The hardware setup traditional ECPT system

Table 3-1 Hardware parameters of the infrared camera FLIR A655sc

Parameters	**Value**	**Unit**
Temperature accuracy	± 2	℃
Spatial resolution	640×480	Pixels
Maximum frame rate	200	Hz
Detector pitch	17	μm
Spectral range	7.5-14	μm
Detector time constant	~8	ms

3.2.2 Eddy current pulse compression thermography System (ECPuCT)

From the perspective of the experimental system, the current pulsed excitation system has limitations when the defect is in the subsurface, the inhomogeneity of the conductivity reduces the SNR of transient response. To improve the capability of ECPT system from the excitation techniques, the pulse compression technique is applied in this work. This section gives a detailed explanation of PuC(pulse compression) techniques. PuC is a wide-spread measurement technique used to experimentally estimate the impulse response of a Linear Time-Invariant (LTI) system in a noisy environment or in the presence of shallow SNR values [299]. In standard PT, flash lamps are commonly employed to excite the sample -assumed as an LTI system- within a time significantly shorter than the typical cooling time of the sample itself. Therfore, the so-provided heating stimulus can be modelled as a Dirac's Delta function $\delta(t)$, and the corresponding output $y(t)$, i.e. the pixel temperature/emissivity amplitude recorded with the elapsing time, is a good approximation of the impulse response $h(t)$ [19]. Features of interest are obtained by analyzing the $h(t)$ within a chosen range of interest T_h as showed in Figure 3-5(b). As it is shown in Figure 3-5(a), in PT the excitation is considered instantaneous, and the sample impulse thermal response is measured for a time of interest T_h, which is the impulse response time duration. In PuCT, the sample is excited with a coded excitation of duration T, and thermograms are collected for an overall time duration of $T + T_h$. An estimated impulse response of duration T_h is retrieved after performing the PuC algorithm (*i.e.* the duration of the equivalent PT analysis) [19,36].

PuC requires further processing to achieve an estimate $\tilde{h}(t)$ of the impulse response $h(t)$, the quality of the estimation depending strictly on both the correct implementation of the PuC algorithm and on the correct design of the coded signal [300]. The working principal of the PuC technique is sketched in Figure 3-5(b). Given a coded excitation $s(t)$ of duration T and bandwidth B, and another signal $\Psi(t)$, the so-called matched filter, such that their convolution "$*$" approximates the Dirac's Delta function $\delta(t)$ as:

$$s(t) * \Psi(t) = \tilde{\delta}(t) \approx \delta(t) \tag{3.36}$$

Then an estimate $\tilde{h}(t)$ of the $h(t)$ is obtained by convolving the recorded output signal $y(t)$ with the matched filter $\Psi(t)$. The process is mathematically shown below for a single pixel of the acquired thermograms, in the presence of an Additive-White-Gaussian-Noise $e(t)$, which is uncorrelated with $\Psi(t)$. By convolving the output signal $y(t)$ with the matched filter $\Psi(t)$, the impulse response can be obtained as:

$$\begin{aligned} \tilde{h}(t) &= y(t) * \Psi(t) = h(t) * \underbrace{s(t) * \Psi(t)}_{=\tilde{\delta}(t)} + e(t) * \Psi(t) \\ &= h(t) * \tilde{\delta}(t) + \tilde{e}(t) \approx h(t) + \tilde{e}(t) \end{aligned} \tag{3.37}$$

The main advantage of PuC over pulsed excitation is that an estimate of the impulse response can be achieved at the end of the procedure while delivering energy to the system over an extended time. In this way, it is possible to provide more energy, and hence to increase the SNR and detectability of eddy current thermography system. The SNR gain is proportional to the $T \times B$ product, *i.e.* it can be enhanced almost arbitrarily by increasing either the time duration or the bandwidth of the coded waveform. It should also be noted that the limited $T \times B$ product of practically employed coded signals results in an $\tilde{h}(t)$ always affected by sidelobes. This can be improved by a proper choice of the matched filter signal Ψ(t) [301]. In this thesis, $s(t)$ is a Barker Code (BC) of order equal to 13 and the matched filter Ψ(t) has been chosen simply to be the time-reversed sequence of the input coded signal $s(-t)$ [144, 302].

The coded signal employed for modulating the induction heating system on/off state was a bipolar BC with a bit length of 13. However, the BC code is not employed in its original bit version in PuCT application. In fact, each "1" and "-1" of the original BC code is padded with a series of "1" or "-1" respectively to allow the heat source spreading enough energy toward the SUT. Besides, changing the single bit duration varies the frequency spectrum of the resulting BC modulated heating stimulus. This means that a proper design of the BC code leads to the onset of thermal waves having a desired yet needed thermal diffusion lengths μ, allowing defects buried at different depths to be detected. The thermal diffusion lengths μ can be calculated by Eq.(3.23), by considering both the diffusivity α, and the frequency f value of the modulated thermal frequency spectrum at which the maximum heat emission occurs, *i.e.* 0.5 Hz in this case. Figure 3-6(a) shows the employed BC signal in which, every single bit lasts one second at the chosen FPS (50 frames per second), while its thermal frequency spectrum is depicted in Figure 3-6 (b).

In the implementation of ECPuCT, the chosen BC modulates the induction heating unit, $i.e.$ the on/off time instant at which a current I of given amplitude Amp and frequency $f_{carrier}$ flows within the coil. Figure 3-7 shows a sketch of the modulated EC signal by BC in ECPuCT.

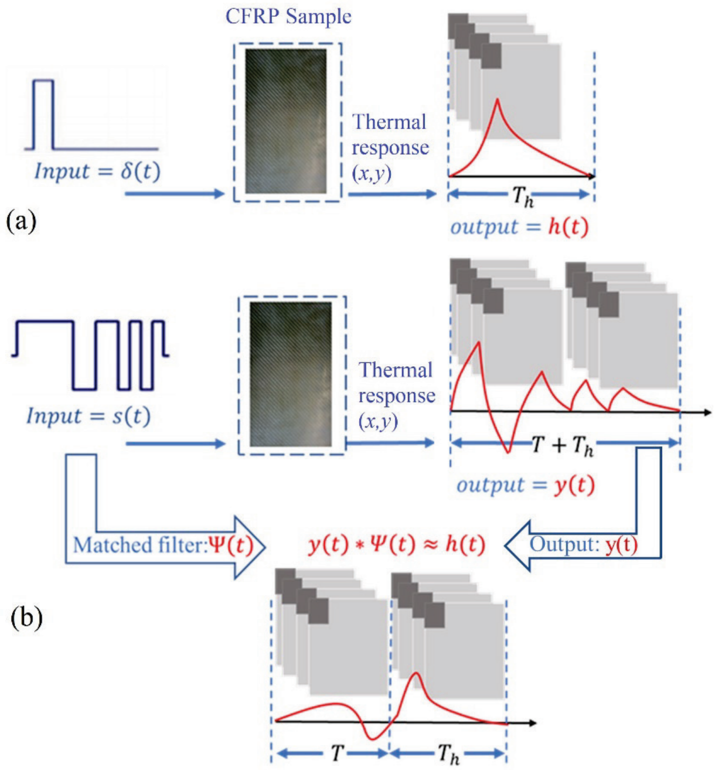

Figure 3-5 Estimation of impulse response

(a) Single-pulse excitation, (b) Process of impulse calculation

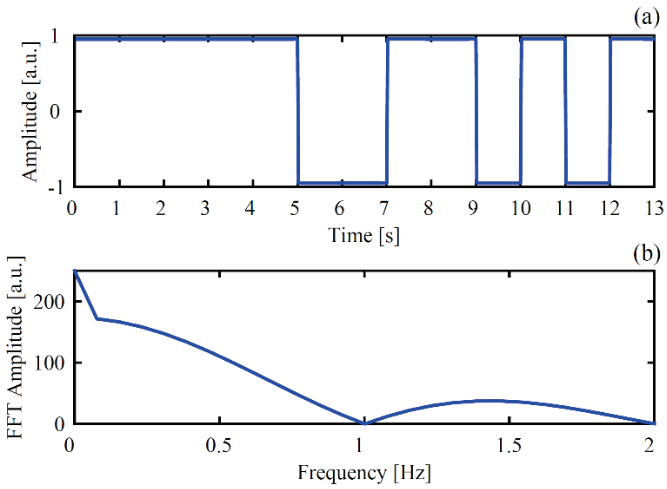

Figure 3-6 Barker Code signal as implement in ECPuCT and its spectrum

(a) Barker code in the time domain, (b) Barker code in the frequency domain

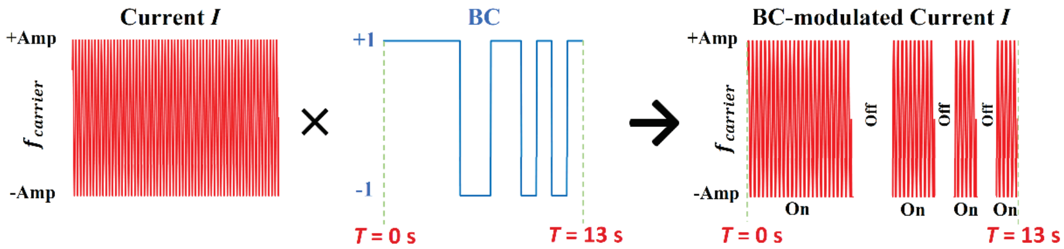

Figure 3-7 A sketch of the modulated EC signal by Barker Code in ECPuCT used in the thesis

3.3 Feature extraction of transient thermal signal

In this section, the feature extraction techniques used in the thesis for different purposes are introduced, including the kernel principal component analysis, partial least square, random transform, skewness, and kurtosis. The kernel principal component analysis is used for defect location and signature enhancement[1]. The partial least square technique is used for the removal of the non-uniform heating pattern[283]. The random transform is used for evaluation of the intensity of orientation in the multi-layer CFRPs. Statistical features, including skewness and kurtosis, can be applied for quantification of depth and size, respectively.

3.3.1 Kernel principal component analysis for defect location

This section gives a detailed explanation of the process of using K-PCA for feature extraction. After obtaining the transient thermal response $\tilde{h}(t)$The Kernel Principal Components Analysis (K-PCA) method is applied to locate the defected area and select abnormal pixels for feature extraction. The novel thermal pattern enhancement method is based on the K-PCA method. Compared with the traditional imaging PCA, this method considers the transient thermal response of each pixel rather than each image in the thermal video as independent variables. Each extracted PC is a linear combination of the original thermal response, and they form the basis of the respective vector space, arranged in order of decreasing variance. Thus, the first several PCs carry the most information regarding the original data [144].

To gain insight on how K-PCA is applied here for enhancing ECPT data, the implementation of the enhancement method is schematically depicted in Fig.4 (b) and mathematically introduced here below. Considering the transient thermal response $\tilde{h}$'s retrieved pixels by exploiting the procedure described in Eq.(3.38) being reshaped as:

$$[\tilde{h}_1, \tilde{h}_2, \dots, \tilde{h}_{M-1}, \tilde{h}_M] \tag{3.38}$$

where M is equal to $N_x \times N_y$ denotes the total number of x and y pixels of the acquired IR thermograms. Thus, the reshaped data can be recognized as a matrix having the dimension of $Q \times M$, where Q denotes the number of frames recorded by the IR camera, *i.e.* $T_h \times FPS$, where FPS stands for the acquired Frames Per Second. By using the kernel method, the impulse response is projected to kernel space ϕ, thus obtaining the kernel matrix $K(i,j)$ as:

$$K(i,j) = \frac{1}{M}\sum_{i=1}^{M}\left(\phi(\tilde{h}_i) - \frac{1}{M}\sum_{j=1}^{M}\phi(\tilde{h}_j)\right)\left(\phi(\tilde{h}_i) - \frac{1}{M}\sum_{j=1}^{M}\phi(\tilde{h}_j)\right)^{\mathrm{T}} \tag{3.39}$$

where ϕ is Gaussian kernel function, defined as Eq.(3.40):

$$\phi(\tilde{h}_i^1, \tilde{h}_i^2) = \exp\left(\frac{\left\|\tilde{h}_i^1 - \tilde{h}_i^2\right\|_2^2}{2\sigma^2}\right). \tag{3.40}$$

The kernel matrix $K(i,j)$ of Eq.(3.39), can be simply named as K. The eigenvector α of K can be obtained as:

$$\lambda_i \alpha_i = K\alpha_i \tag{3.41}$$

Based on the obtained eigenvectors α_i, the enhanced thermal pattern can be projected as:

$$H_{enhanced} = [\alpha_1, \dots, \alpha_T] H_{original}^{\mathrm{T}} \tag{3.42}$$

where $H_{enhanced}$ contains different extracted thermal patterns.

The process for enhancing defective pattern enhancement and location shown in Figure 3-8.

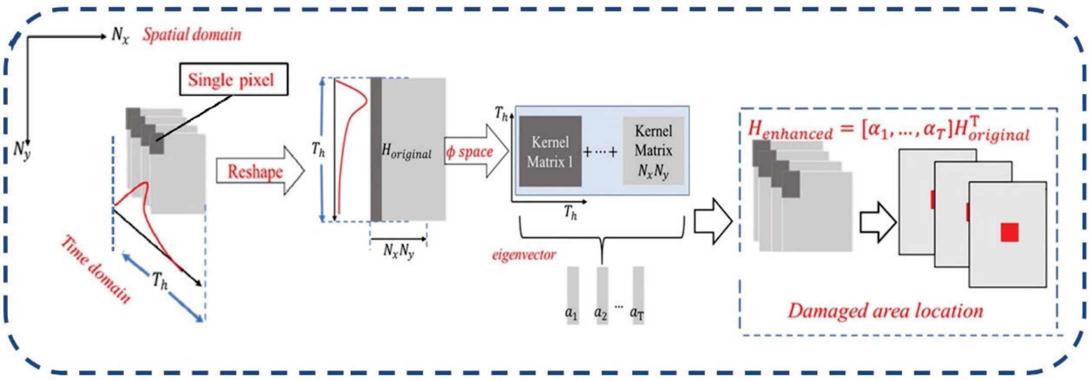

Figure 3-8 Block diagram of the implementation of the feature extraction process

3.3.2 Partial least square for non-uniform heating removal

The PLS technique was applied to reconstruct the non-uniform heating pattern generated by the coil shape and the anisotropy of the material properties. As for the implementation, the PLS can reconstruct the whole three-dimensional data (x, y, t) to characterise the non-uniform heating pattern at each time. Thus, by subtracting the original data by the PLS reconstructed data, the surface condition and anisotropic conductivity influences are mitigated. The algorithm is depicted in Figure 3-9 and mathematical formulation is shown below.

The set of 3D data for transient thermal response $H_{N_x \times N_y \times N_t}$ is reshaped from 3D to 2D as $H_{N_t \times (N_x * N_y)}$, which can be shortened as H_{set}. The PLS mathematical modelling of H_{set} is conducted as:

$$H_{set} = TP^T + E \quad , \quad Y = TQ^T + F \tag{3.43}$$

where $Y_{N_t \times 1}$is corresponding to each frame number vector $[1, \ldots, N_t]$ and $T_{N_t \times a}$ is the score matrix. The scores are interpreted as latent variables of each frame provoking systematic variation in H_{set}. $P_{N_t \times a}$ and $Q_{a \times 1}$ are the loadings matrices, which describe the way of projecting $T_{N_t \times a}$ to H_{set} and Y, respectively. H_{set} and Y are assumed to be partly modeled by same latent variables $T_{N_t \times a}$. The score matrix $T_{N_t \times a}$ columns are orthogonal to each other and H_{set} can be estimated as linear combination of $T_{N_t \times a}$ with coefficient weights $W_{(N_x * N_y) \times a}$. Thus, scores T can be expressed as:

$$T = H_{set}W. \tag{3.44}$$

After the calculation of scores, loadings P and Q are estimated through the regression of H_{set} and Y. Then, residual matrices are computed by subtracting the estimated TP^T and TQ^T from H_{set} and Y, respectively. The regression coefficients B for the model are obtained using the following equations:

$$B = WQ^T \tag{3.45}$$

that can be solved as:

$$Y = H_{set}B + F = H_{set}WQ^T + F. \tag{3.46}$$

The PLS problem is solved based on the Iterative Partial Least Square (IPALS) algorithm. After obtaining PLS components TP^T of the data H_{set}, the first PLS component is applied to reconstruct the non-uniform heating pattern, and PLS subtraction is conducted on the first component reconstructed data.

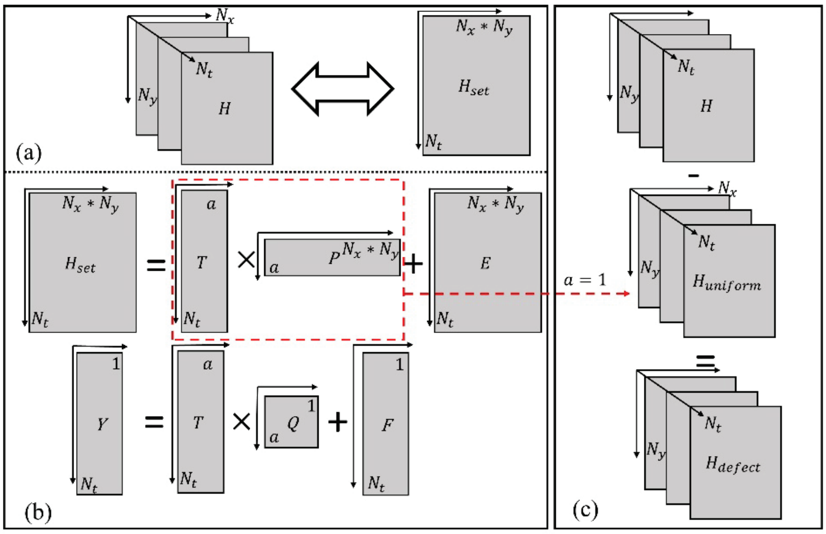

Figure 3-9 Implementation process for PLS subtraction

(a) Data reshape process, (b) PLS component calculation, (c) Subtraction on the first PLS component

3.3.3 Radon transform for orientation feature extraction.

The quantification of the orientations in the CFRP structure is essential for determining the misalignment and stacking error to ensure the integrity of the component. Random transform techniques are implemented as the feature-based approach for evaluation of orientation. This section gives a detailed implementation of the technique.

Considering the thermal image as $A(x, y)$, where the orientations to be evaluated is not determined, the radon transform of $A(x, y)$ is presented as follows [303]:

$$R(s, \theta) = \sum_{x=0}^{M-1} \sum_{y=0}^{N-1} A(x, y)\delta(x \cos\theta + y \sin\theta - s) \tag{3.47}$$

In the above equation, δ is the Dirac function for enabling the sum of in θ direction, Where N is the number of pixels along with the axis s. To identify the time of fly behaviour of the specific ply orientation in the time domain, the radon transform of ECPT in the time domain can be characterised as follows:

$$RT(t) = [\max\ R(s, \theta, t_1), \max\ R(s, \theta, t_2), \ldots, \max\ R(s, \theta, t_n)] \tag{3.48}$$

If the orientation to evaluate is fixed at θ_k, the orientation's behavior in time can be characterised as $RT(t, \theta_k)$ and its gradient:

$$RT(t,\theta_k) = [\ R(s,\theta_k,t_1), \text{max}\ R(s,\theta_k,t_2),\ldots, \text{max}\ R(s,\theta_k,t_n)] \qquad (3.49)$$

$$\frac{dRT(t,\theta_k)}{dt} \qquad (3.50)$$

3.3.4 Skewness feature and kurtosis quantifying the transient thermal response

Due to the asymmetric distribution of transient response, where the heating stage response is exponentially increasing and the cooling stage is exponentially decreasing, the skewness feature is used to describe the variation of the shape of the transient response. The skewness feature extraction for the transient response can be calculated as follows:

$$S(T) = \frac{E(T-\mu)^3}{\sigma^3} \qquad (3.51)$$

Where T denotes the transient response, μ denotes the mean value of the T, and σ denotes the variation of the data.

Kurtosis is applied to measure the heaviness of the tail compared with the normal distribution of the data. Generally, the transient response with the shape of the heavy tail leads to a higher value of kurtosis. The kurtosis can be calculated as follows:

$$K(T) = \frac{E(T-\mu)^3}{\sigma^3} \qquad (3.52)$$

Figure 3-10 demonstrates the purpose of applying skewness and kurtosis for the evaluation of the characteristics of transient response. As the figure shows, the asymmetric distribution can be related to the time to reach maximum heating. For instance, in the case of positive skewness, where heating time is shorter than that of the cooling stage, the faster the heating time is, the higher the skewness value is. For kurtosis, the high kurtosis value is related to the significance of the heating, which can be correlated with the electrical conductivity of the material. Therefore, by combing the skewness and kurtosis of the transient response, the QNDE of electrical and thermal properties of the material can be comprehensively conducted.

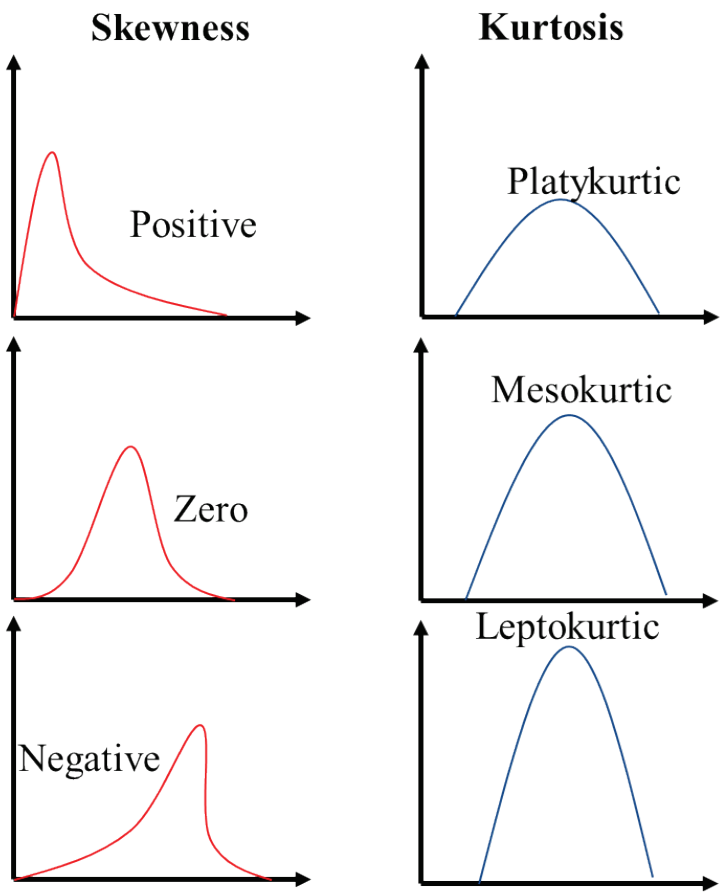

Figure 3-10 Illustration of the distribution of skewness and kurtosis for transient response evaluation

3.4 Reconstruction based quantitative evaluation for CFRP.

As illustrated in the last section, the feature-based approach QNDE approach is effective in dealing with single parameter evaluation when the feature is well calibrated for quantifying the specific parameter. However, there exist requirements for estimating the specific properties of the structure, e.g., thermal conductivity and electrical conductivity, in the case of induction heating, which is challenging for the feature-based approach. Thus, in this thesis, the reconstruction based QNDE approach is also proposed to serve as a complementary approach for estimating the electrical and thermal properties using eddy current pulsed thermography. The illustrating of the difference between the feature-based approach and the reconstruction-based approach is shown in Figure 3-11. The feature-based approach refers to the application of feature extraction methods, e.g., K-PCA, on the transient response of the ECPT system. The values of the feature can be calibrated to obtain a certain model to describe the defect parameters of the benchmark sample. While for the reconstruction-based approach, one simulation model is required; in this case, it is illustrated in Section 3.1.3. Then, the iteration optimisation process is implemented to minimize the difference between the output of the FEM model and the experimental measurement signal using a reconstruction algorithm.

The detailed implementation of the inversion algorithm and experimental setup for CFRP QNDE is illustrated in chapter 6.

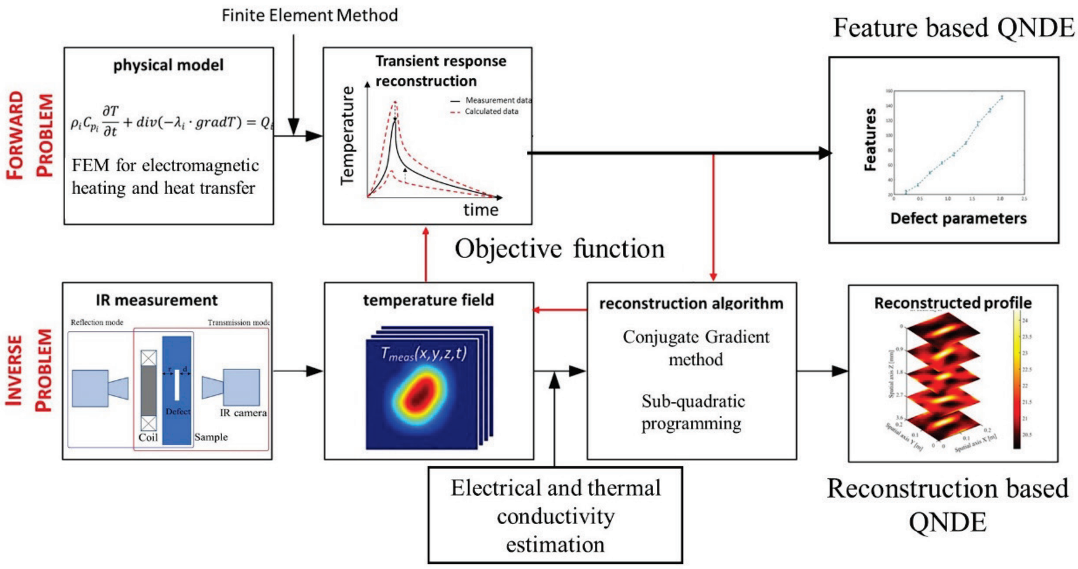

Figure 3-11 Diagram presenting the principle of feature-based and reconstruction based QNDE approach

3.5 Chapter summary

In this chapter, the methodology used and proposed in the thesis including the simulation and modelling, experimental system, feature-based and reconstruction-based QNDE approach is introduced: 1)The methodology of simulation and modelling is illustrated in terms of the theory of electromagnetic heating, volumetric heating theory for CFRP and multi-layer CFRP modelling for ECPT; 2) Two experimental systems including eddy current pulsed thermography system and eddy current pulse compression system The pulse compression theory, which aims to improve the SNR of the ECPT transient response, is mathematically described; 3)The numerical modelling, which integrates the multi-physics coupling between electromagnetic and thermal field, and anisotropic behavior of CFRP, is proposed and detailed explained;

4)The feature extraction techniques serve for different functionalities of QNDE including defect location, non-uniform heating pattern removal, orientation feature extraction, and depth quantification are mathematically presented. In the next chapter, based on the proposed techniques, the first case study for quantification of delamination depth in CFRP is conducted.

Chapter 4 Quantitative evaluation of delamination depth in CFRP using eddy current pulse compression thermography

The chapter explores the feature-based QNDE techniques for the evaluation of delamination with various depths in the CFRP structure. The system diagram of the case study is explained in Section 4.1. Detailed implementation of the feature-based approach, including K-PCA, skewness, and kurtosis, is presented in Section 4.2. Section 4.3 illustrates the experimental setup and benchmark sample for this case study. Section 4.4 presents the results for delamination detection and quantification. The conclusion is made in Section 4.5.

4.1 Introduction

Delamination is one of the most prevalent defects for composite materials, which might arise either during the manufacturing process or during their in-service life, e.g., during the standard lifetime of aircraft components. Typical delamination initiates and grows between different plies of the composite, which may result in lowered in-plane strength and stiffness, eventually leading to catastrophic failure of the whole structure [304]. To detect delamination and ensure the safe operation of composite components, NDT techniques are used during both manufacturing and operation of the composite components.

The aims of this case study are (i) to increase the detectability of delamination and (ii) to evaluate them quantitatively on an artificially-delaminated CFRP sample by using coded waveforms and PuC technique in ECPT. Hereinafter, such a combination will be referred to as Eddy Current Pulse-Compression Thermography (ECPuCT), of which the detailed implementation is presented in Section 3.2. Figure 4-1 shows the block diagram of the overall process to extract features for the delamination depths characterisation using ECPuCT. Each block of this diagram, numbered from 1 to 4, shows the steps followed in this study to extract the final feature. ECPuCT method is firstly applied to the CFRP benchmark sample containing humanmade delamination defects at different depths, and the raw data, in the form of thermograms, is acquired, as for block 1. Then a denoising algorithm is applied on each individual pixel's signal to remove noise, and a non-linear fitting function is also exploited to remove the step-heating contribution from the denoised data -as explained in [305]- See Figure 4-1 block 2. Then, as shown in block 3, the calculation of the impulse response $h(t)$, calculated by Eq. (3.37), performed by convolving the de-trended signal with a matched filter. After obtaining the impulse response $h(t)$ of each individual pixel, the feature extraction process is carried out, as depicted in block 4. K-PCA technique, presented in Section 3.4.1, is used on the retrieved $h(t)$'s to obtain principal components and to enhance delaminated areas. Based on the enhanced delaminated area, the impulse responses, including delaminated and non-delaminated areas, are selected manually. Different features, including the proposed crossing point of $h(t)$'s and skewness of defective areas impulse responses are validated and compared for delamination depth evaluation.

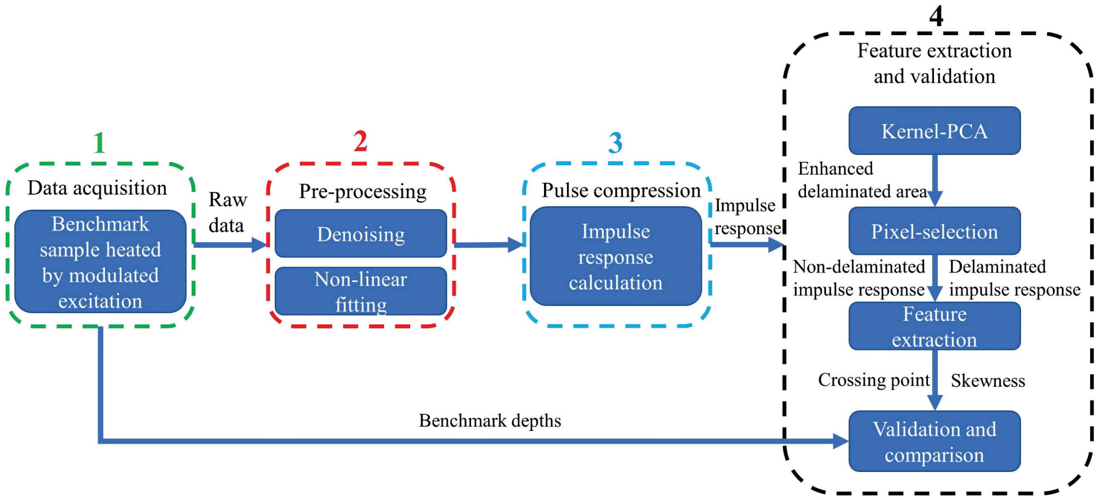

Figure 4-1 Block diagram of the processing steps of delamination depth quantification

4.2 Feature extraction process for delamination depth quantification

This section gives a detailed explanation of the process depicted in block 4 of Figure 4-1. After calculating the estimated impulse response $\tilde{h}(t)$. The K-PCA method is applied to locate the delaminated area and select abnormal pixels for feature extraction. The crossing point between defective and non-defective areas are selected for depth evaluation, whose process is presented in Figure 4-2.

Three different features, including crossing point and skewness, are extracted based on the selected impulse response. The crossing point is defined as the first cross point of the impulse response curves onto the defective area and non-defective area. The specific calculation of skewness and kurtosis to characterise the impulse responses' shape is presented in Equations (3.51) and (3.52)[306]. To calculate the features, the first 200 frames of T_h were used, which is shown in Figure 4-2. The reason for using this period is that previous studies [19, 36] has shown that the range of interest of the collected impulse response is limited to less than 10 seconds for reflection mode PuCT analysis. TheRef.ore, 200 frames have been here selected for the feature extraction in transmission mode, which corresponds to 4 seconds of diffusion time when an acquisition rate of 50 Frames Per Second (FPS) is employed. Moreover, side lobes affect the estimated impulse response would otherwise have a negative effect on the feature's extraction performance, e.g., reducing the sensitivity of the proposed feature for depth evaluation.

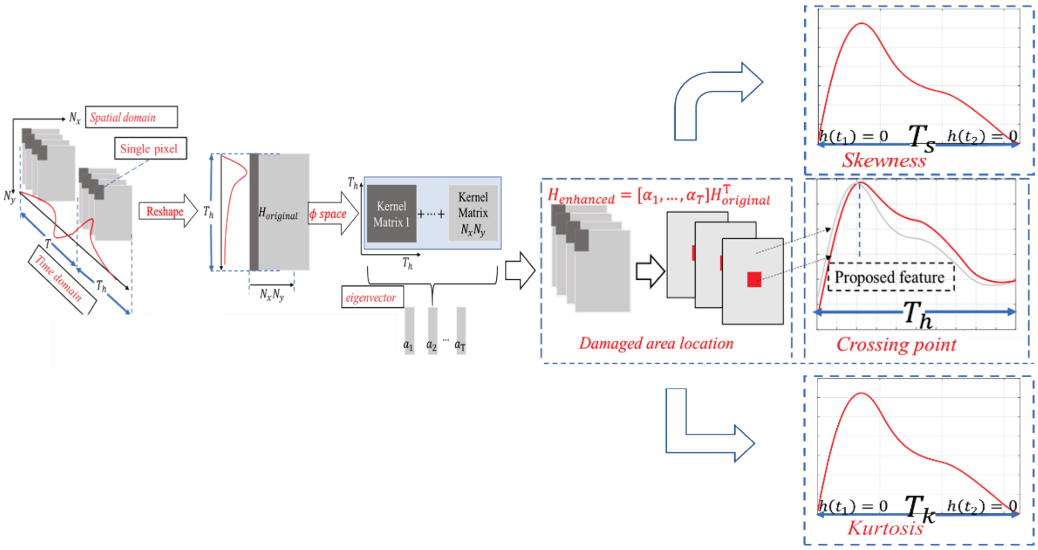

Figure 4-2 Diagram of the feature extraction process

4.3 Experimental setup

The ECPuCT system diagram is illustrated in Figure 4-3(a). A signal generator is used to send both the BC modulating signal to the induction heating coil and a Ref.erence clock trigger to the IR camera to acquire thermograms at 50 FPS. A Cheltenham Easyheat 224 Induction heating unit is used for coil excitation with a maximum excitation power and current values of 2.4 kW and 400 A, respectively with tuneable $f_{carrier}$ from 150 to 400 kHz. For the reported experimental results, values of excitation current I equal to 40 A and $f_{carrier}$ of 240 kHz were selected to avoid eventual damage on the CFRP sample due to the long excitation time using the BC signal.

Figure 4-3(b) shows a picture of the employed rectangular coil made of a high-conductivity hollow copper tube. Water cooling was implemented to the coil, and the lift-off was maintained at 3 mm from the SUT surface to ensure the volumetric heating of the sample. Only one side of the coil is selected as a linear coil to introduce parallel eddy currents in the direction of maximum conductivity in the sample. IR camera was the FLIR SC655, equipped with an un-cooled microbolometer detector array with a resolution of 640 × 480 pixels, the spectral range of 7.5 - 14.0 μm and NETD < 30 mK. The IR camera records the surface temperature distribution of the 13 s BC as well as an additional 30 seconds cooling period [305]. Finally, captured thermal videos were transmitted to a PC for visualization and postprocessing, including signal pre-process,

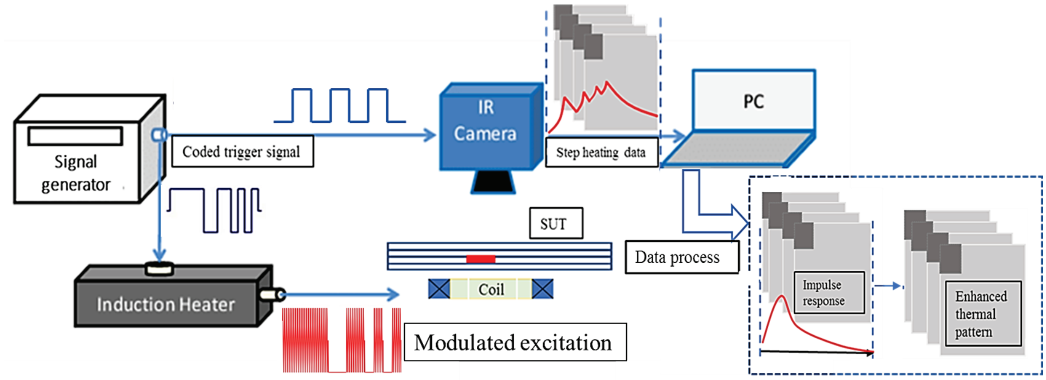

(a)

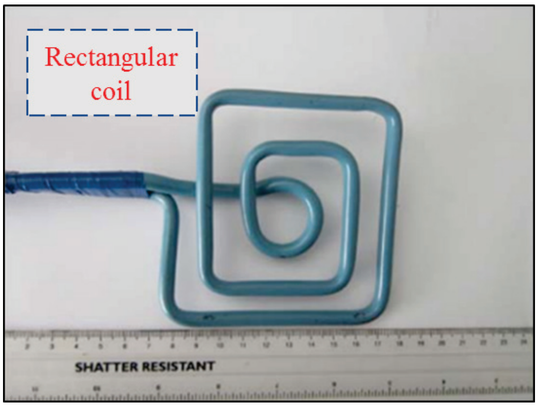

(b)

pulse compression, thermal pattern enhancement, and depth feature extraction.

Figure 4-3: Experimental setup

(a) Sketch of the experimental setup, (b) detail of the employed rectangular coil

The CFRP sample was realized by the MDP company (Terni, Italy) [305]. The CFRP laminate sample contained twelve plies of carbon fibre fabric with an areal density of 0.2 g/m3. Its lateral dimensions were 240 mm×200 mm for an overall thickness of ~2.80 mm. The fibre's orientations were 0° and 90°, and the matrix was an Epoxy Resin RIM 935. The laminate was made by vacuum-assisted resin infusion, and it was cured at room temperature and postured at 110 °C for two hours to obtain a fully cured system. The artificial delamination was realized by inserting thin square pieces of Teflon tape, having lateral dimensions of 20 mm×20 mm and thickness equal to 75 μm between the plies (see Figure 4-4(a)). Nine artificial defects were inserted at increasing depths: the shallower was placed under the 2nd ply at a depth d~0.46 mm (defect #1), the deepest

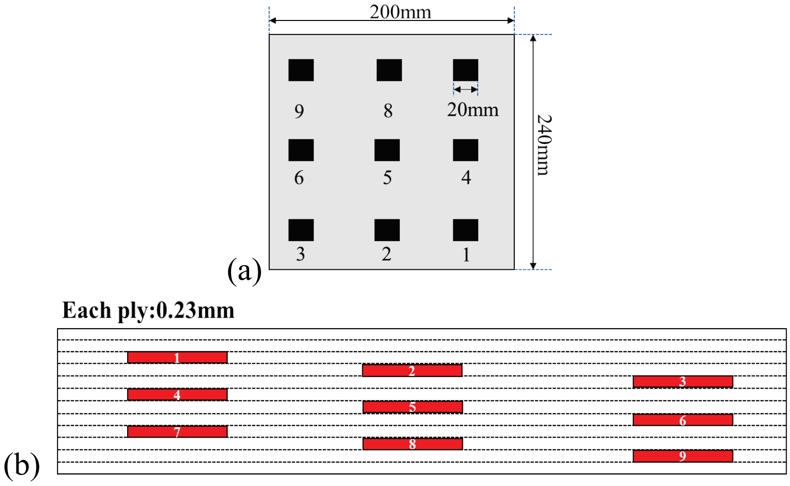

Figure 4-4 Schematic diagram of SUT

(a) plan view, (b) cross section view

(defect #9) under the 10th ply at a depth of d~2.3 mm as shown in Figure 4-4 (b).

4.4 Results and discussion

In this section, the results of the feature-based QNDE approach are fully illustrated in terms of the pulse compression for calculating impulse response, the defect location using K-PCA, and the quantitative feature extraction using the crossing point, skewness and kurtosis.

4.4.1 Process of obtaining estimated impulse response

As discussed in section 4.3, the BC excitation is applied to generate raw data. As block 2 of Figure 4-1 shows, the raw acquired data must be pre-processed before successfully applying the PuC algorithm to obtain estimated impulse response: the raw acquired data contains (i) noise generated during the signal acquisition process and (ii) an additional step-heating contribution due to the monopolar heating source that must be removed.

Regarding point (i), although the PuC algorithm acts as a low-pass filter as it is based on the convolution with a bandlimited matched filter signal Ψ(t) (see Eq.((3.36))), it is crucial to minimize the noise to ensure a successful feature extraction of delamination depth. To this aim, wavelet analysis is acknowledged as the most effective method for de-noising non-stationary thermal signals [307]. By using the multi-resolution and self-

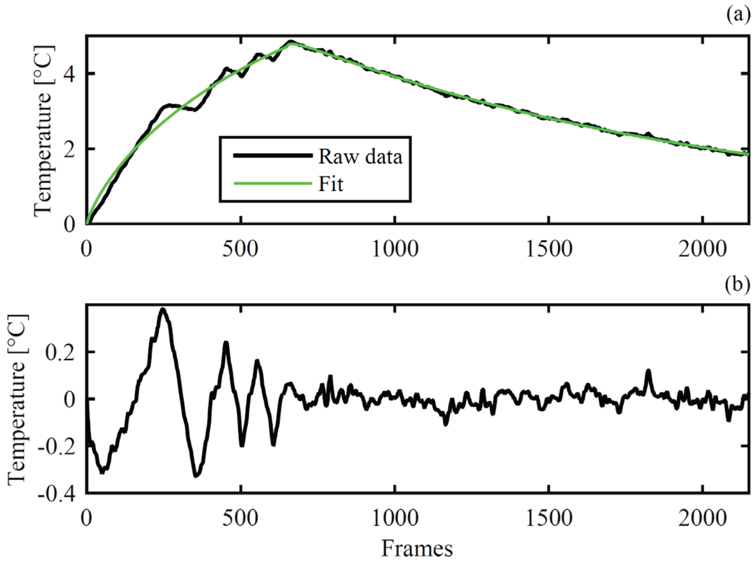

Figure 4-5 Computation of de-trended signal for PuC

(a) BC raw data and non-linear fitting function; (b) De-trended signal

similarity characteristics of wavelet analysis, the pseudo-white noise in non-stationary thermal signals can be eliminated.

Regarding point (ii), Silipigni et al. [19] presented different de-trending algorithms and polynomial functions for LED-stimulated PuCT applications. Their proposed non-linear fitting function is here used. Figure 4-5(a) shows the denoised thermal signal together with non-linear fitting function obtained for a single pixel, whilst Figure 4-5 (b) depicts the same signal after step-heating component removal, thus ready for PuC.

As discussed in Section 3.2, Figure 4-6 shows examples of the impulse responses obtained for a single pixel after PuC, hence obtained by convolving the signal depicted in Figure 4-5 (b) with the matched filter Ψ(t), both for a BC retrieved raw signal and for a BC de-trended and denoised raw signal. It can be noticed in Figure 4-6 that the signal maximin amplitude is reduced when applying denoising due to the elimination of non-stationary thermal noise, but the smoothness of impulse response after pulse compression is increased with respect to the raw signal depicts a sample impulse response of a single-pixel; it can be observed that the level of the sidelobe compared to the main lobe maximum amplitude is ~0.4. This may affect the process of feature extraction performance. Therefore, as explained in Section 4.2, the signal has been truncated from 0 to 200 frames of the corresponding T_h.

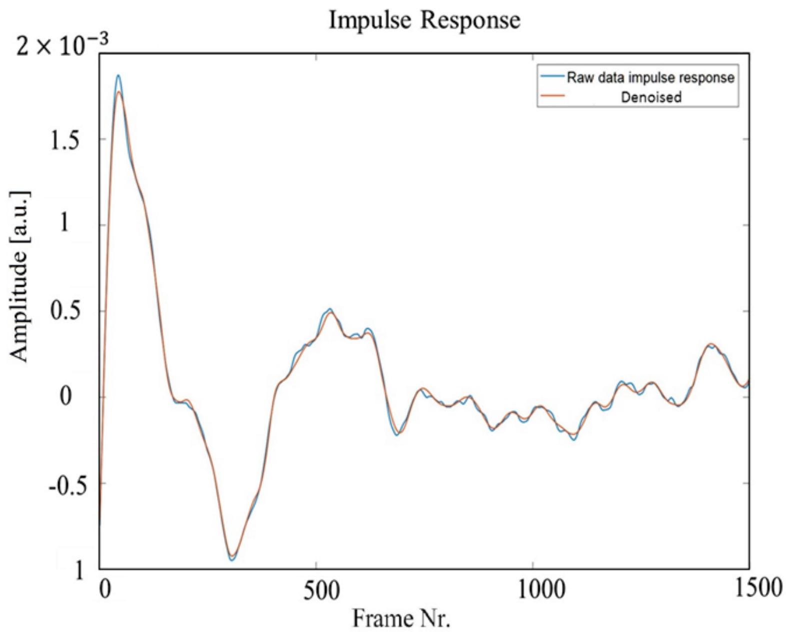

Figure 4-6 Comparison of one pixel's raw and denoised impulse response

4.4.2 Delaminated area location by Kernel-PCA

As illustrated in block 4 of Figure 4-1, the K-PCA technique is applied to enhance and locate the delaminated area. In this section, detailed implementation is introduced.

The impulse response $\tilde{h}(t)$ is a sequence of 1500 frames, *i.e.,* 30 seconds corresponding to the whole T_h . However, when it comes to visualizing the delamination, most of the frames contribute little to the defect location. To solve this problem, the K-PCA method described in section 3.4.1 is applied to find and learn the mutual relation of impulse response in individual pixels. Thus, the pixelwise-retrieved $\tilde{h}(t)$'s are embedded into a suitable high-dimensional feature space through the Gaussian kernel function. In addition, the kernel method is also an efficient way to imply the nonlinear characteristics of the raw data.

Figure 4-7 shows the extracted thermal pattern from the raw data (threshold). It is noted that first thermal pattern projected by PC1 summarizes the overall heating phenomena during experiment because the heating is conducted on one side of the rectangular coil, which generates linear heating. The sensitivity of pattern 1 for visualizing defect is heavily reduced for increased delamination depth. This is because pattern 1 contains most of information about heating pattern, which might cover up the faithful defect information. It is observed that patterns 2 and 3 projected by PC2 and PC3 respectfully obtain opposite profile or weighting for delamination area. Pattern 2 generally presents the delamination in lower contrast while pattern 3 shows higher contrast compared to the surrounding area. This is because the eigenvectors extracted were supposed to be orthogonal with each other in kernel space ϕ. The indicated relationship between pattern 2 and pattern 3 can enhance the detectability in the delamination area through logic operation, which is shown in Figure 4-8. In addition, since the largest electric and thermal conductivity values are along the fibre orientation, the delamination as a thermal barrier hinders the heat diffusion mainly in 0° and 90° directions, which makes the delamination edges hotter, and the delamination region colder[308]. As a result, the delamination and its edge have a large contrast in thermal pattern 1. Based on this fact, the enhanced thermal pattern of the nine defects are presented in Figure 4-9, where the achieved higher contrast shows the profile of delamination. Compared to the results in [305], where defect #9 was not observable under flash thermography and LED-stimulated PuCT, the induced eddy current can still penetrate into 2.30 mm depth to generate detectable IR signature of the deepest delamination. Defect SNR is reduced after D5, where the square shape of the delamination profile cannot be identified. However, the delaminated area can still be characterised by fibre structure in 0° and 90° from D6~D9 since induced eddy currents are parallel to 0° and 90°, which have the largest electrical conductivity and thermal conductivity in SUT thus generating abnormal thermal wave with diffusion length μ longer than the delamination depth d.

Generally, artificial delamination in CFRP has been demonstrated to exhibit different patterns by the K-PCA method. The enhanced pattern emphasizes the defect with a larger contrast in comparison to the sound regions and provides a guide on how to select the proper pixels or regions of the impulse response to quantitively evaluate the different depths of delamination. In the Sections 4.4.3 and 4.4.4, the impulse response retrieved at the area of the most abnormal pixel is investigated for feature extraction.

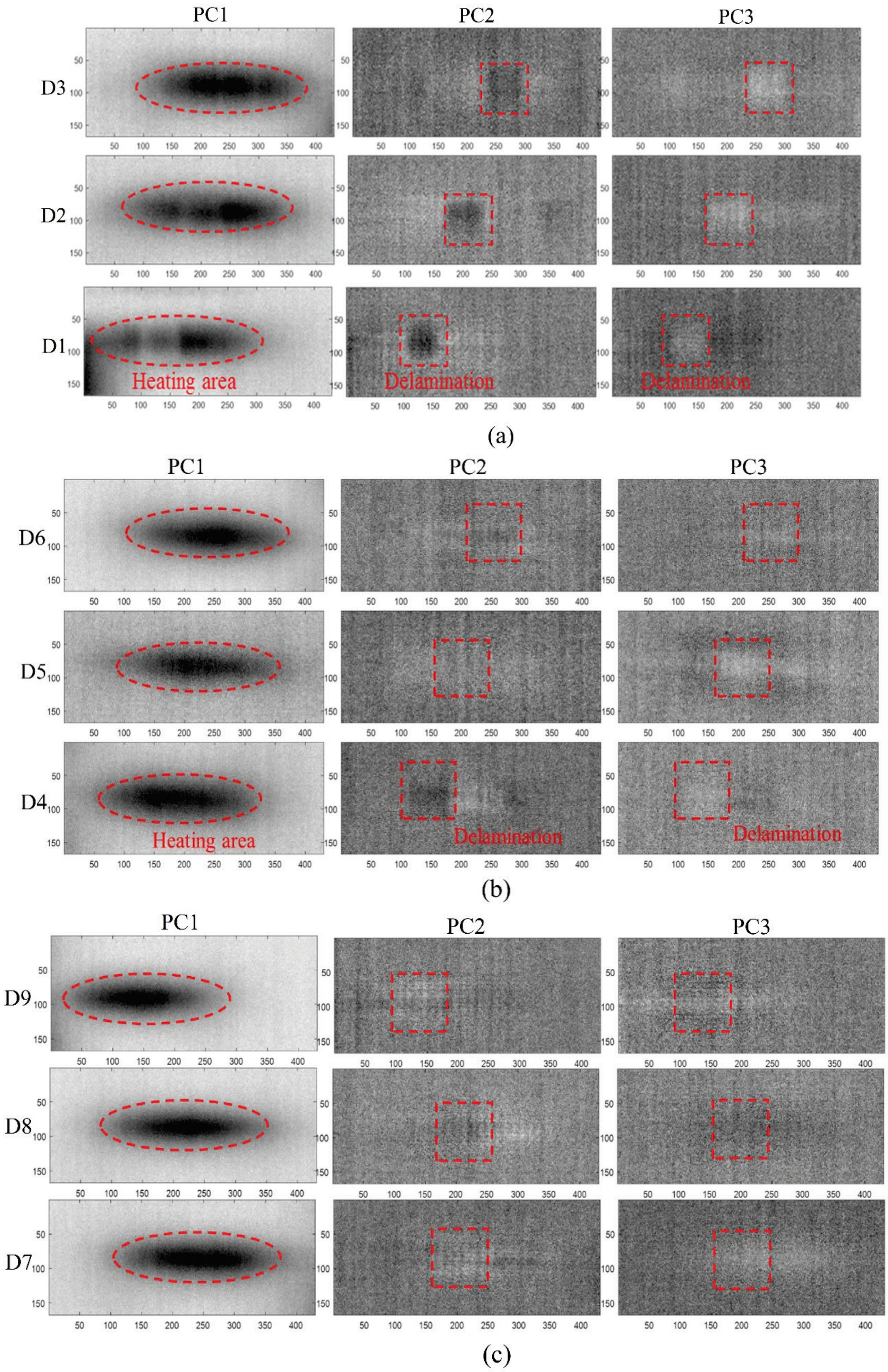

Figure 4-7 First three extracted thermal patterns

(a) D1, D2, D3, (b) D4, D5, D6, (c) D7, D8, D9

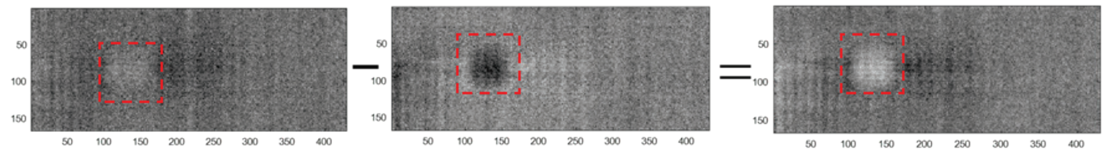

Figure 4-8 Process of obtaining enhanced pattern

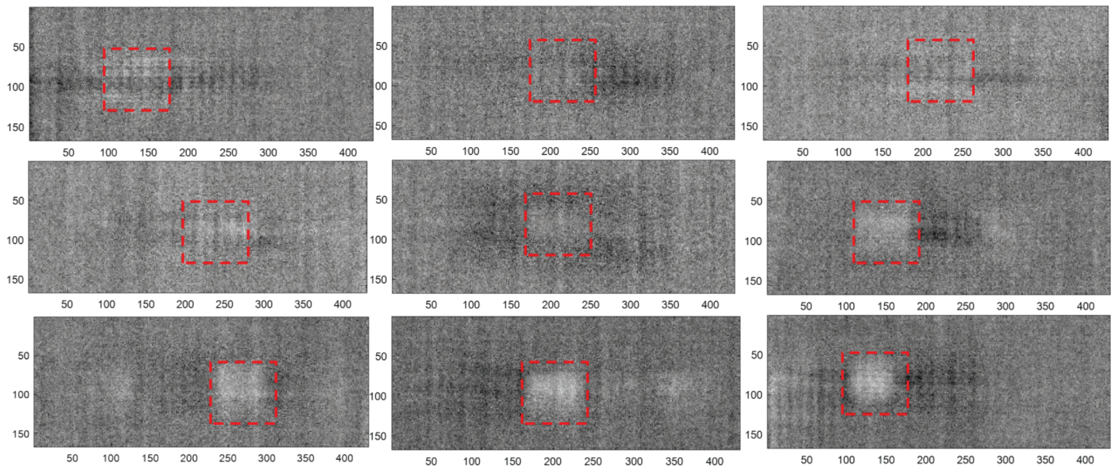

Figure 4-9 Enhanced thermal pattern D1~D9

4.4.3 Crossing point feature analysis

As discussed in section.4.4.2, the delamination ranging from 0.46 mm to 2.30 mm of depth can be visualized by an enhanced thermal pattern method based on the impulse response. Moreover, to determine the delamination depth, the phase contrast between defected and non-defected areas can be exploited by the comparison of the obtained impulse responses based on PT theory [137]. The defected areas are detected and selected by KPCA, as shown in Figure 4-10 in line with the sample introduction in Figure 4-4.

Each defected area and non-defected area are formed by five lines of data in the center of higher contrast and lower contrast based on the enhanced pattern. Based on the selected area, the comparison between impulse responses of defected and non-defected areas are presented in the plot series of Figure 4-11. It can be noted that the impulse response curves behave similarly to the general trend for both the defective and the sound areas. However, the defective area is cooling slower due to the thermal diffusivity, which means the material ability to exchange heat with its surroundings has become worse with the increase in depth. The deeper the delamination, the worse is the ability to exchange heat with the non-defective area. Results showed in Figure 4-12 demonstrates that the impulse response amplitude is less sensitive than the phase change of the crossing point of the defective and non-defective area. Thus, it is observed that the position of the first crossing point of impulse responses of defected and non-defected areas has a monotonic relationship with delamination depth, as shown in Figure 4-10 (labeled area) and Figure 4-11. This can serve as an excellent feature to quantify the delamination depth. From Figure *4-12*, it can be noted that the feature based on the crossing point value follows a linear trend if three defects in a row over the SUT are considered, *e.g.,* D1-D3 or D6-D9, which is due to the linear coil used in this experiment. In fact, the experimental conditions can be considered the same if defects are on the same line. Better results could possibly be obtained by achieving more uniform heating through optimizing coil configuration.

However, after defect 6, the crossing pattern of the defected area and the non-defected area has been disturbed by noise, as shown in Figure *4-12* (c). Moreover, extra crossing points are observed in D7, the continuous equal value of defected and non-defected areas in D8 and initial disturbed crossing points in D9 are caused by the low SNR of the original signal. Thus, despite the effectiveness of the denoised approach applied in this work, the accurate sizing of defect is still challenging to be extracted in D7~D9.

To validate this crossing point feature of impulse responses, the experiments were conducted again under reflection mode. The process of feature extraction for transmission and reflection modes is the same as illustrated in the Figure 3-2. It is observed in Figure *4-12* and Figure *4-13* (b) that the proposed features have monotonic relationships with delamination depth in reflection mode. Furthermore, the proposed feature in reflection mode holds better linearity and sensitivity, as shown in Figure *4-12*, and better stability (less standard deviation error), as in Figure *4-11*(b) than transmission mode. In addition, compared with impulse responses in transmission mode in Figure *4-11*, the response curves of the delaminated and the non-delaminated areas in reflection mode becomes divergent. These differences can also be investigated in the future.

To summarize, the proposed crossing point feature was validated in both transmission and reflection modes, so it can be concluded that the proposed feature can be used for quantifying CFRP delamination depth. The cross point feature, e.g., crossing point time

Ref.ects the defect depths and the skin depths of eddy current in both transmission and reflection mode.

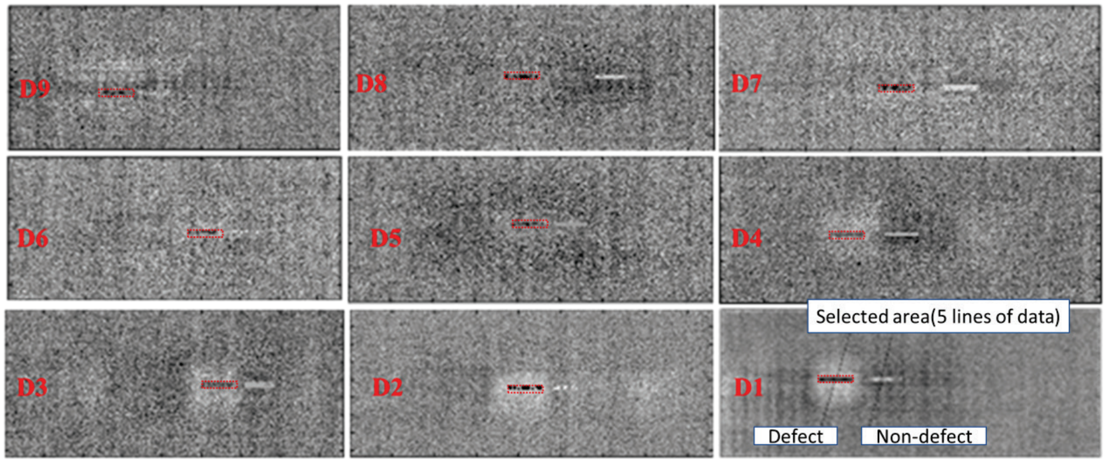

Figure 4-10 Selected damaged area and non-damaged area based on K-PCA enhanced pattern

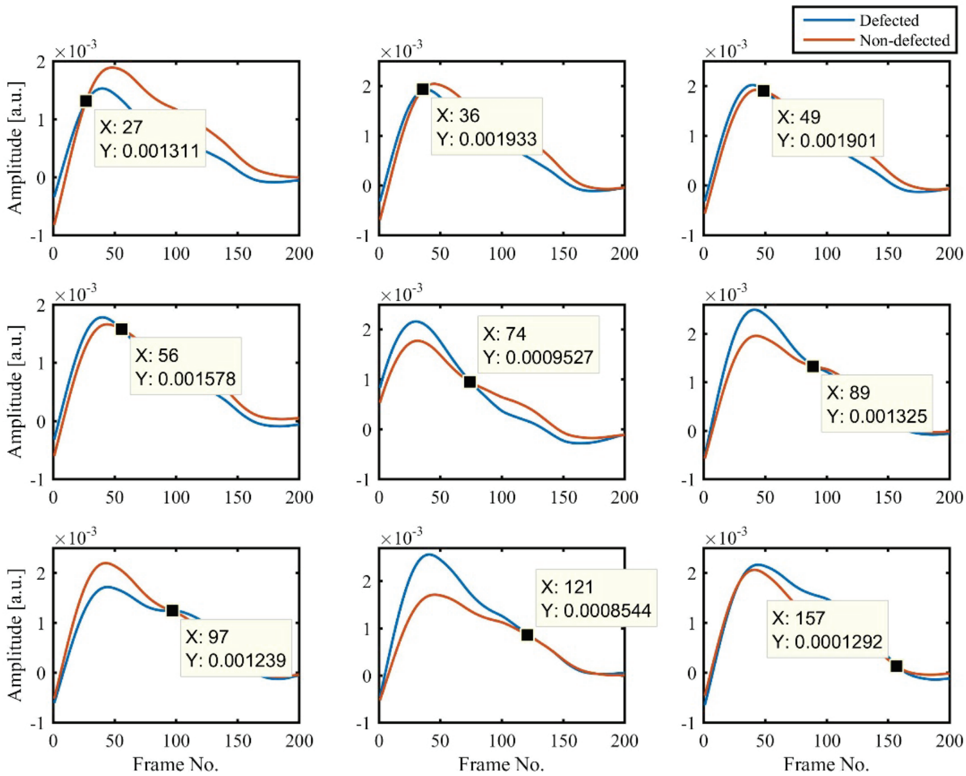

Figure 4-11 Crossing point feature obtained from the mean value of selected impulse responses in transmission mode

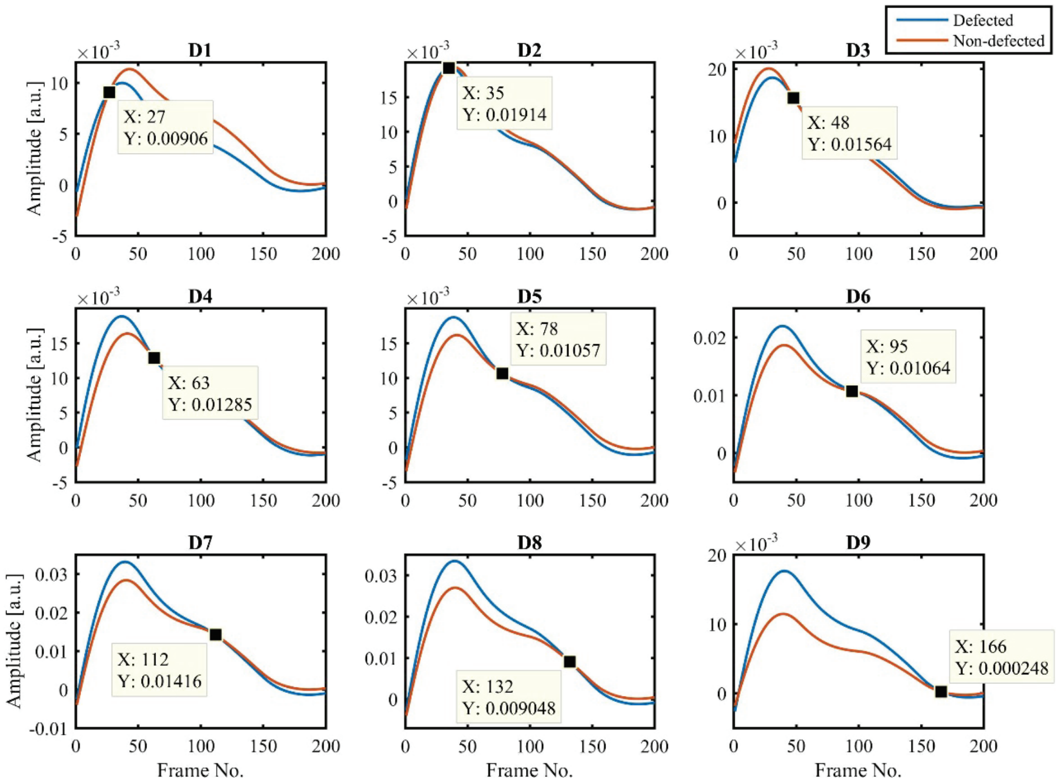

Figure 4-12 Crossing point feature obtained from the mean value of selected impulse responses in reflection mode

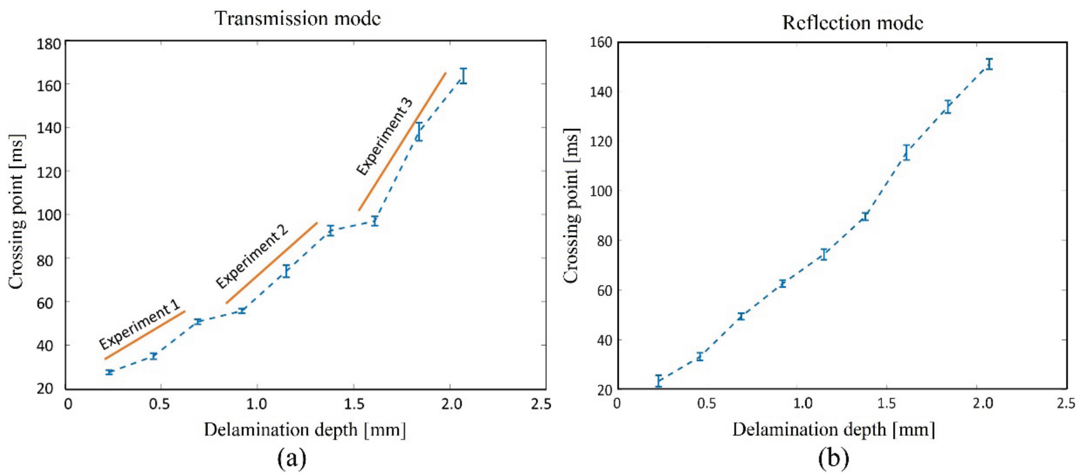

Figure 4-13 Feature validation of crossing point with error bar versus delamination depth

(a) transmission mode, (b) reflection mode

4.4.4 Skewness and kurtosis feature analysis

Based on the mathematical definition of skewness, this feature can be used to quantify the asymmetry of the considered data. In this section, the skewness is calculated on the major part of the impulse response (first 200 frames of T_h period). It is observed that positive skewness values are found for impulse responses, as depicted in Figure 4-14. In Figure 4-14(a), the skewness of data in transmission mode shows a monotonic relationship with delamination depth because the impulse response curves of 9 defects are becoming more symmetrical along with the increase of delamination depth. However, in reflection mode, Figure 4-14 (b), this relationship becomes less monotonic than in transmission mode, which might be due to the texture influence on the selection of abnormal pixels. The kurtosis feature is also calculated at the same proportion as the skewness feature. The kurtosis is high order statistical approach to measure the heaviness of tails of normally distributed data. It is observed in Figure 4-15(a) and (b), the kurtosis feature shared similar behavior as a skewness feature, where the reflection mode behaves worse than the transmission mode for quantifying the delamination depth.

As a matter of fact, in reflection mode, the IR camera is much closer to the coil than the transmission mode to maintain the same lift-off in two different modes. Thus, the fibre texture contributes to reflection mode is more evident than in transmission mode. Figure 4-16 presents the enhanced pattern of defect #1 by K-PCA in transmission and reflection mode. It is observed that fibre structure in reflection mode is more obvious than the transmission mode, which proves the idea that texture influence is more significant in reflection mode. The crossing point performance is also good in reflection mode, even with surface texture influence, as illustrated in Figure 4-13 (b).

Overall, the skewness of the extracted impulse response can help characterise the delamination depth because of its monotonic relationship with delamination depth.

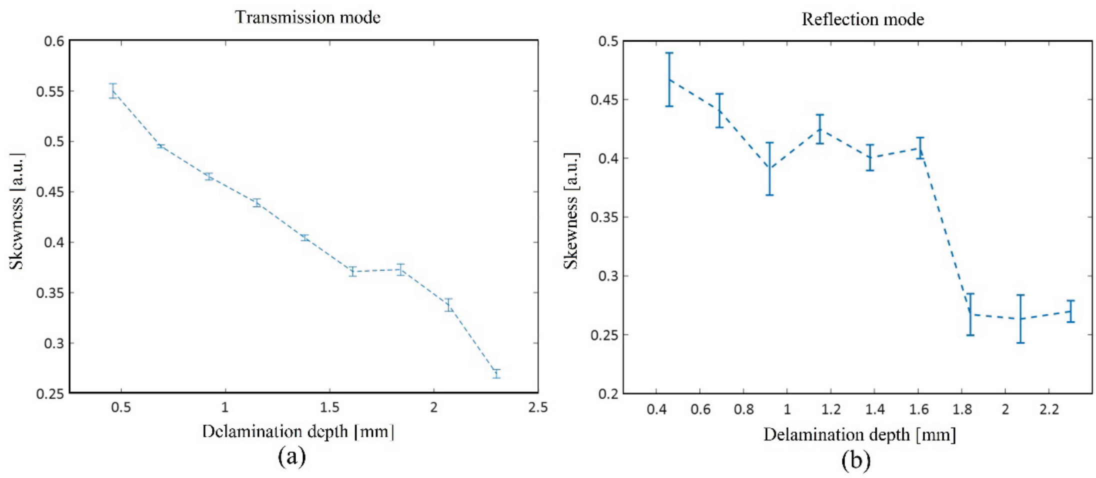

Figure 4-14 Error bar plot of the skewness features in different modes

(a) transmission mode, (b) reflection mode

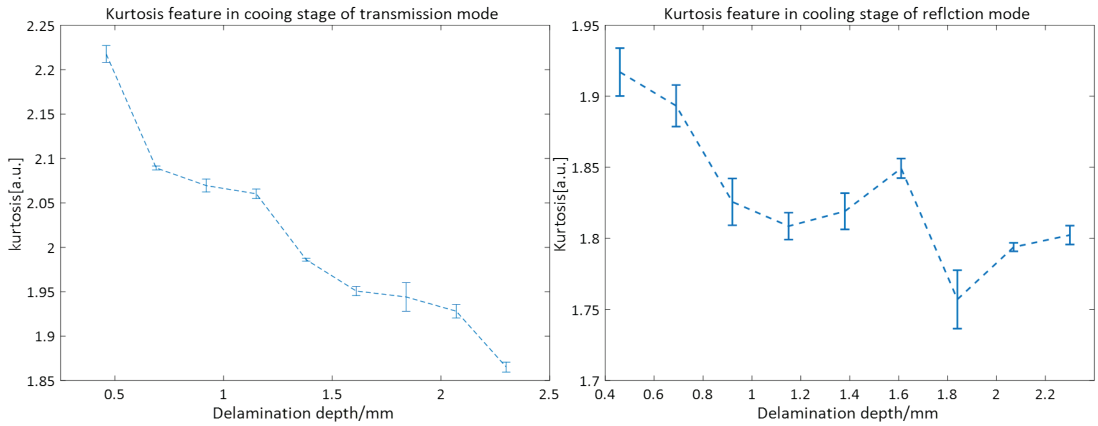

(a) (b)

Figure 4-15 Error bar plot of the kurtosis features in different modes

(a) transmission mode, (b) reflection mode

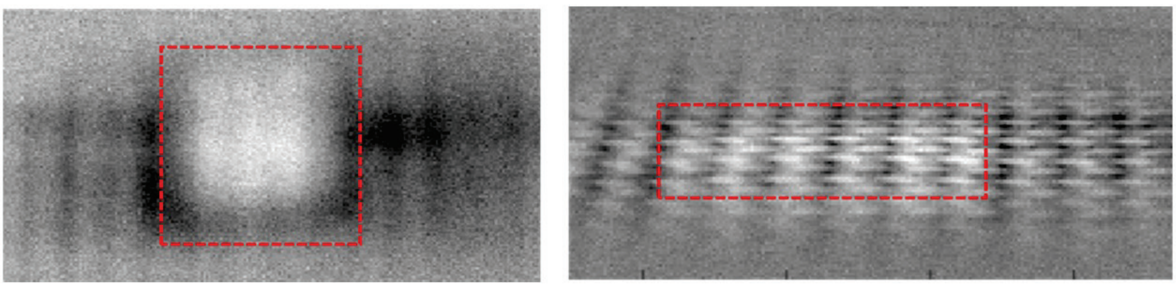

(a) (b)

Figure 4-16 Enhanced pattern of defect #1

(a) transmission mode, (b) reflection mode

4.5 Chapter summary

In this chapter, the ECPuCT system, which combines the eddy current pulsed thermography and pulse compression technique, is explored for characterising delamination with different depths in CFRP laminates, different features including crossing point, skewness, and kurtosis were compared and validated. The proposed features were verified through experimental studies under both transmission and reflection mode. The summary of this work is as follows:

1) The K-PCA method can well extract the meaningful pattern in the impulse response behavior as time elapses, helping in locating the delamination areas effectively. It was observed that the method could reveal the spatial pattern, which corresponds to the defect with enhanced contrast, hence improving defect

detectability.

2) The proposed crossing point feature is extracted based on the crossing point of impulse response from defective and non-defective areas previously discriminated by the K-PCA method. This feature has a monotonic trend in both transmission and reflection modes for delamination depths. The feature performance in terms of linearity is better in reflection mode than in transmission mode.
3) The skewness and kurtosis feature of the impulse response are also investigated. It is shown that these two features illustrate the same monotonic relationship with delamination depths in transmission mode as well. However, the monotonic relationship does not keep with delamination depths in reflection mode due to the influence of the texture structure. Compared with other features' performance in reflection mode, the feature of the crossing point demonstrates more robustness against texture to ensure the stability in reflection mode.

In the next chapter, the proposed ECPuCT system was applied for the evaluation of debonding in the multi-layer CFRP structure. The difference between delamination and debonding is that delamination is a defect at different depths with the same material properties while debonding is a defect at the same depth with different properties. The first case poses a challenge for depth quantification ability, which is addressed by utilizing the pulse compression technique. The latter case poses challenges of non-uniform heating patterns for multi-physics properties evaluation, which is addressed in the next chapter.

Chapter 5 Evaluation of debonding in CFRP-epoxy adhesive single-lap joints using eddy current pulse-compression thermography

This chapter investigates the feature-based QNDE techniques for the evaluation of debonding with different electrical and thermal properties in the CFRP structure. The introduction of system setup, including experiment system, sample, feature-based approaches of the debonding in CFRP-epoxy adhesive single-lap joints, is explained in Section 5.1. Detailed implementation of the feature-based approach is presented in Section 5.2. Section 5.3 illustrates the benchmark sample of CFRP-epoxy adhesive single-lap joints. Section 5.4 presents the results for debonding detection and properties quantification. The conclusion and summary are made in Section 4.5.

5.1 Introduction

Contaminations arising during the manufacturing or usage of Carbon Fibre Reinforced Plastic (CFRP)-epoxy adhesive single-lap joints can drastically affect the mechanical performance of the structure and eventually lead to its catastrophic failure. However, the evaluation of the interface quality in bonded structures is still a challenging task. This is because the faithful evaluation of bonded areas is hindered by various factors: (i) their complex shape, (ii) the heterogeneous nature of the multilayer adherend, (iii) the non-uniform heating pattern combined with significant lateral thermal diffusion. All the mentioned factors contribute to the recorded thermograms and cause poor Signal-to-Noise Ratio (SNR), therefore being difficult to interpret the results.

This chapter tackles the challenge of detecting the interface contamination by combining eddy current pulse-compression thermography and image post-processing algorithms. As illustrated in Figure 5-1, the impulse responses from samples containing either brass, release film, or release agent contaminations were obtained through pulse-compression combined with Eddy Current Pulsed Thermography (ECPT). Non-uniform heating patterns are removed by the partial least square technique. Then, the time instants containing meaningful information about the contaminated interface layer are inferred by comparing each norm of kernel principal component over suitable time windows. The evaluation of contamination depths and properties are conducted in selected time windows by principal component analysis and time-phase analysis.

Results proved that release agent contamination plays a minor role in changing the electrical and thermal properties of the single-lap joints compared with brass and release film.

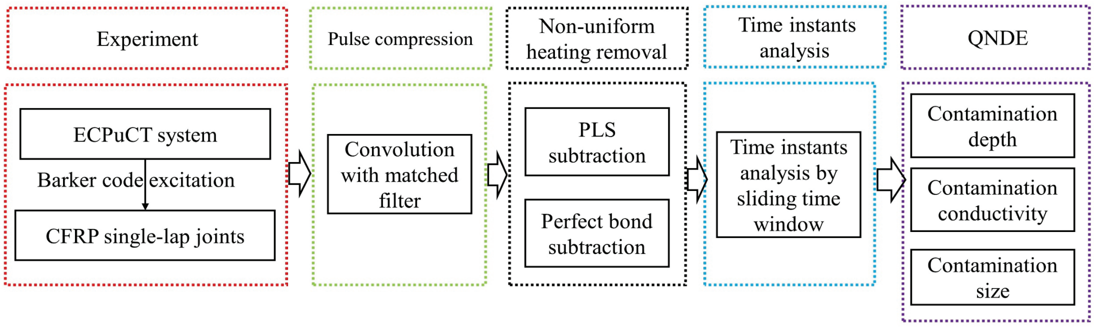

Figure 5-1 System diagram for debonding QNDE

5.2 Feature-based QNDE for debonding evaluation

To quantitatively evaluate the properties of the debonding at the same depth, the location of the time when the information is maximum about the debonding layer is crucial. The evaluation of debonding properties is conducted based on the optimal time window. The process to evaluate the electrical and thermal properties of the contamination is based on the selection of a proper time window within the pixelwise-retrieved $\tilde{h}(t)$ that provides information about the contamination layer. The proposed procedure is schematically depicted in Figure 5-2.

If $H_{N_x \times N_y \times N_t}$ is segmented evenly in time as $h_{i,i+1}$, where i denotes the time position of a chosen time window, then the projected image can be calculated as $\alpha_{i1} * {h_{i,i+1}}^T$ by using K-PCA for $h_{i,i+1}$ to obtain the first principal component. For each projected image $\alpha_{i1} * {h_{i,i+1}}^T$, the contrast of the delamination over the sound area is considered as the norm of each corresponding α_{i1}, which is presented as the Sliding K-PCA part in *Figure 5-2*. By selecting the best image with a positive local maximum α_{k1}, the corresponding image is reconstructed as $\alpha_{k1} * {h_{k,k+1}}^T$.To understand if the period $\alpha_{k1} * {h_{k,k+1}}^T$ contains the maximum information, derivate, and time-phase of the impulse responses are used, as shown in the middle part of Figure 5-2. Then, the image $\alpha_{k1} * {h_{k,k+1}}^T$ is used to locate the contamination response $h_{k,k+1}$ for brass film, release film, and release agent, as it is shown in Figure 5-2 (QNDE labelled part). The contamination properties are characterised by the norm distance of α_{k1}, and the size of brass film and release film is determined by spatial kurtosis on the image $\alpha_{k1} * {h_{k,k+1}}^T$.

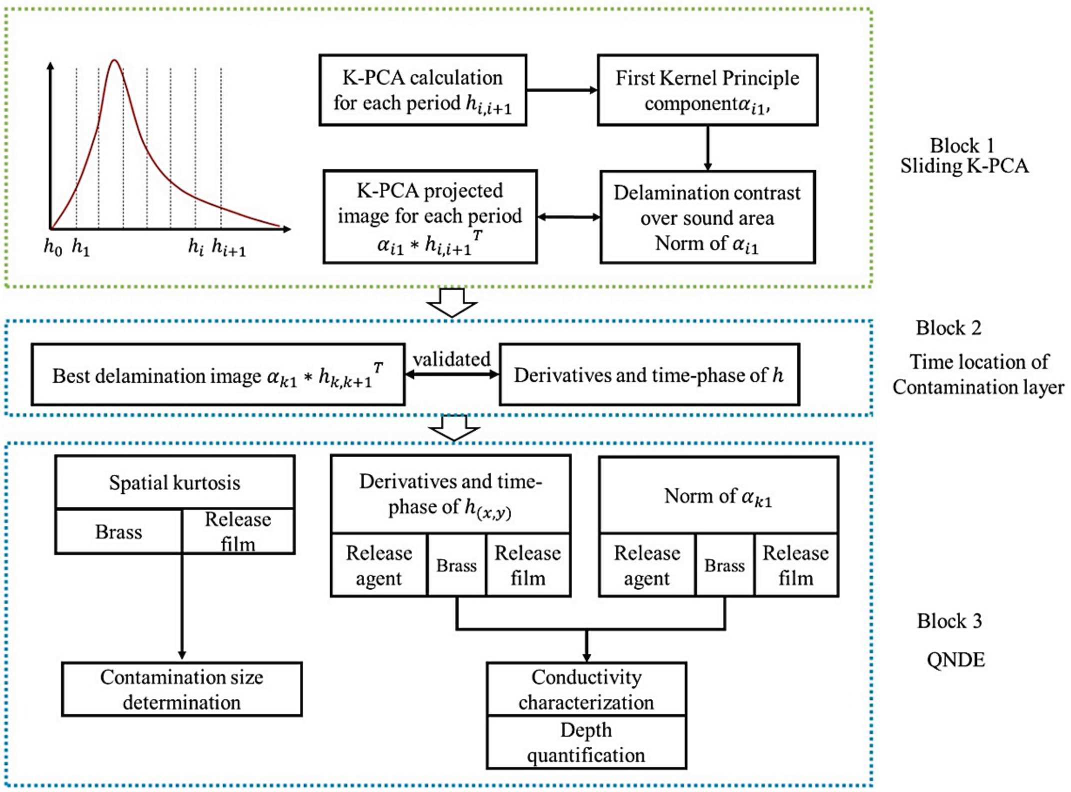

Figure 5-2 Diagram depicting the proposed methodology

5.3 Experimental setup

The ECPuCT experimental setup for this case is the same as Section 4.3. As for the sample used in this chapter, as explained in Section 5.1, three types of contaminated debonding of brass, release film, and release agent was manufactured. The composite plates were manufactured using six plies of HexPly M21 - 5H Satin woven prepreg. Due to the woven structure and the number of lay-up, residual stress can occur in specimens. The thickness of the specimens may vary through the structure. However, the mentioned variation is here negligible as it is in the range of 10^{-6} m. The interfacial contaminations were realized by using brass film, Wrightlon 4600 release film, and Marbocote 45 release agent. As it is shown in Figure 5-3(a), two CFRP plates were overlapped to create a single lap joint, such that the bonded area was 280 mm × 25 mm while the total area of each composite plate was 280 mm × 120 mm.

In the bonding area, two-fold brass film and release film inserts were added to simulate debonding at the interface; release agent was sprayed over the epoxy film sheet prior to second adherend placement to weaken the epoxy quality. As shown in Figure 5-3(b) and Figure 5-4(b), five square release films were placed at the upper interface, having a nominal thickness of 0.076 mm and a size of 12.70 mm × 12.70 mm. Ten square-shape brass inclusions, all having a thickness equal to 0.05 mm were embedded into the sample as depicted in Figure 5-3(a), Figure 5-4(c). Please note that these brass inclusions had different sizes: bigger ones are $12.70\ \text{mm} \times 12.70\ \text{mm}$, and smaller ones $6.35\ \text{mm} \times 6.35\ \text{mm}$. As for the weak bond sample, the part with less contamination was made by spraying the release agent on a mask above the uncured adhesive epoxy, as shown in Figure 5-3(c). On the other hand, the part with more contamination was made by spraying the release agent uniformly on the whole bonding area, as shown by a blue area in Figure 5-3(c). It should be noted that in the latter case, the release agent has been diffused into the uncured epoxy, which may result in untraceable amounts at the interface between the epoxy adhesive and composite adherend.

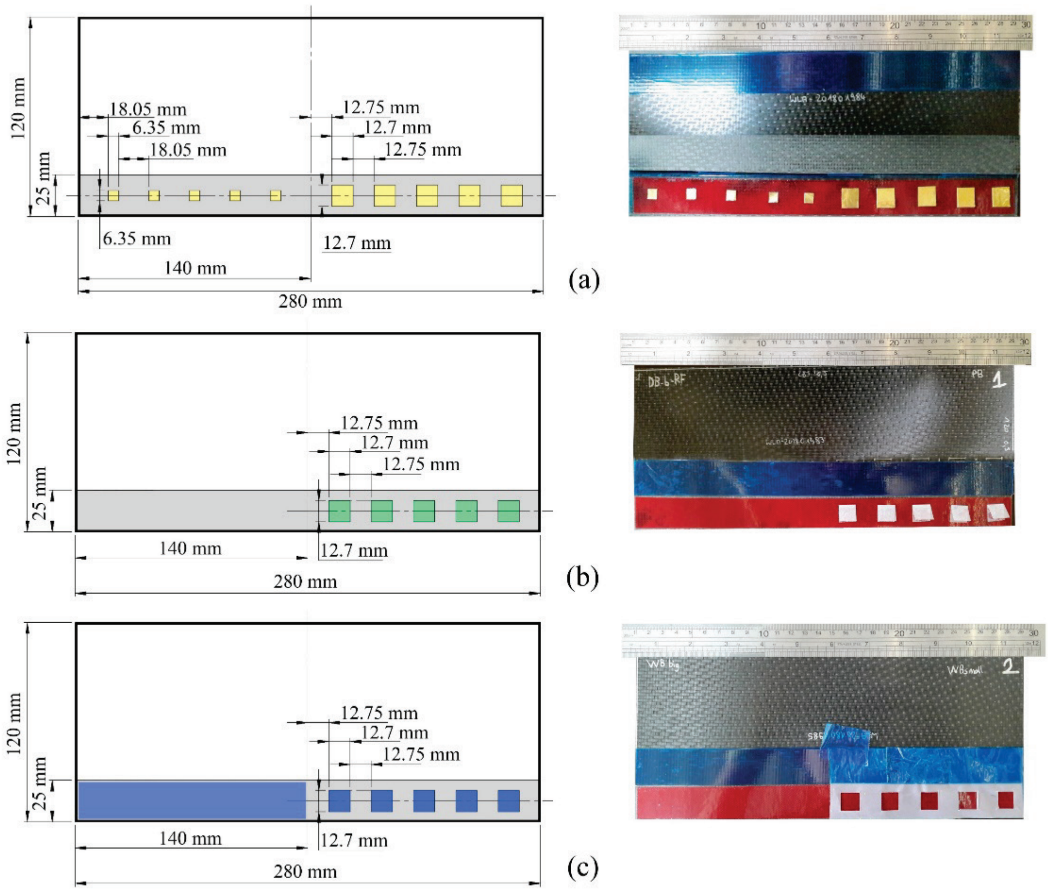

Figure 5-3 CFRP-epoxy adhesive single-lap joints plan sketch

(a) Perfect bond and release film inclusion, (b) Brass film inclusion, (c) Release agent inclusion

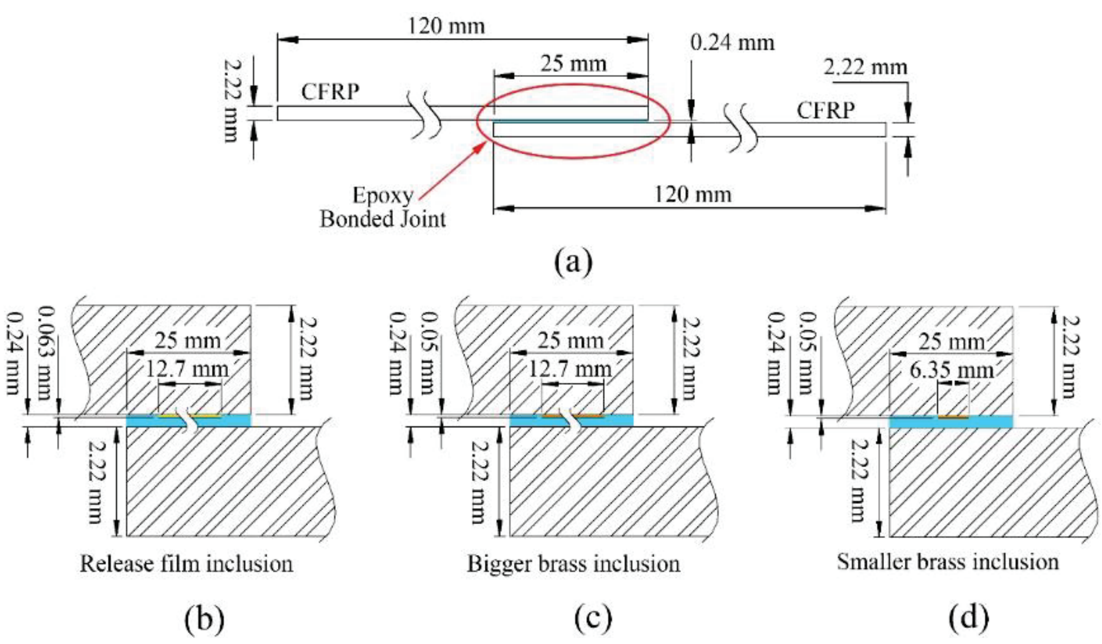

Figure 5-4 CFRP-epoxy adhesive joints cross-section sketch

(a) Perfect bond, (b) Debonding with release film, (c) Debonding with bigger brass film, (d) Debonding with smaller brass film

5.4 Results and analysis

In this section, the PuC thermal data are pre-processed to remove non-uniform heating by PLS, time window sliding for depth detection of contamination, and quantitative evaluation of contamination layers, including classification and sizing of contamination as illustrated in Figure 5-2, QNDE part.

5.4.1 Non-uniform heating pattern removal

The non-uniform heating pattern usually generated by the coil in induction heating can hinder the ability to detect and locate the defect. Thus, as it is shown in the third block of Figure 5-1, this section focuses on the implementation of non-uniform heating pattern removal. The non-uniform heating pattern generated by the anisotropy of the material, geometry, and coil shape should be removed to obtain a more uniform image. This would help in achieving a better feature extraction. Two different methods have been used to remove non-uniform heating patterns: PLS and perfect bond subtraction using the reference image.

In this work, PLS reconstructed thermal data is subtracted from the PuC thermal data. As shown in Figure 3-9, only the first PLS component is used to reconstruct the non-uniform heating according to [309], the first component contains the heating pattern, while second or third components might carry defect information. Besides the PLS approach, repeatable experiment on the perfect bonding sample is also conducted to obtain data without defect but containing non-uniform heating pattern. The results of both approaches are illustrated in *Figure 5-5*. In *Figure 5-5*(a), the $12.70\ \text{mm} \times 12.70\ \text{mm}$ brass film is identified by three heated fibres shown in K-PCA1 using perfect bond and PLS subtraction methods respectively. It is of utmost importance to note that the PLS subtraction method does not require to gather data from the sound sample, thus the misalignment of spatial coordinates caused by different experiments is avoided. Instead, further efforts are needed to subtract perfect bonding in a proper way. TheRef.ore, in the case of K-PCA1 with PLS subtraction, the brass pattern is more uniform and closer to the real square shape than the one obtained over the same sample using perfect bond subtraction (see third row of *Figure 5-5*(a)). However, the pattern of the smaller brass film inclusion $6.35\ \text{mm} \times 6.35\ \text{mm}$ is not clearly visible in *Figure 5-5*(a) that can be due to the texture of the fibres above the brass. In the case of release films depicted in *Figure 5-5*(b), the defects are more clearly visible. The difference in the SNR of the patterns from bigger brass and the release film is due to the fact that brass inserts have higher electrical conductivity than the sound sample, hence not only allowing eddy currents flowing but also heating up due to the Joule's effect. Release film defects are not electrically conductive, therefore completely interrupt and deviate the eddy current flux around them.

It can be observed in the first row of *Figure 5-5* that the K-PCA1 obtained from the raw acquired $h(t)$'s contains the elliptical thermal pattern generated by the excitation coil. On the other hand, by subtracting either the perfect bond or the PLS data from the various contaminated bonding data, the debonding area is further enhanced, as it is visible in the second and third rows of *Figure 5-5*. For the release agent inclusion, the detection capability is massively reduced, as shown in *Figure 5-5*(c) and (d). The contrast between more release agent inclusion and the sound area is observable in *Figure 5-5*(c). The release agent might have been diffused into the epoxy resin or distributed uniformly along the bonded area. However, in *Figure 5-5*(d), the defect pattern is similar to the non-uniform heating pattern, which shows that less release contamination agent is not detectable.

Based on the discussion above, the proposed non-uniform heating removal process using PLS techniques can remove the non-uniform heating pattern for the detection of contamination. Mismatch of spatial coordinates can be avoided through PLS subtraction.

In order to compare and validate the performance of the ECPuCT testing, the benchmark sample is also tested by high-frequency high-resolution acoustic microscopy[310], which is demonstrated in Figure 5-6. The release film detected by acoustic microscopy shows better spatial resolution shown in the second column of Figure *5-6* compared with the ECPuCT techniques. However, the difference between the less release agent inclusion and more of that is poorly characterised by the acoustic microscopy compared with the results in Figure *5-5*(c) and (d). The comparison demonstrates the ECPuCT is better in terms of evaluating the properties of contamination, while the acoustic microscopy is better for detection and location of defect owning its high spatial resolution.

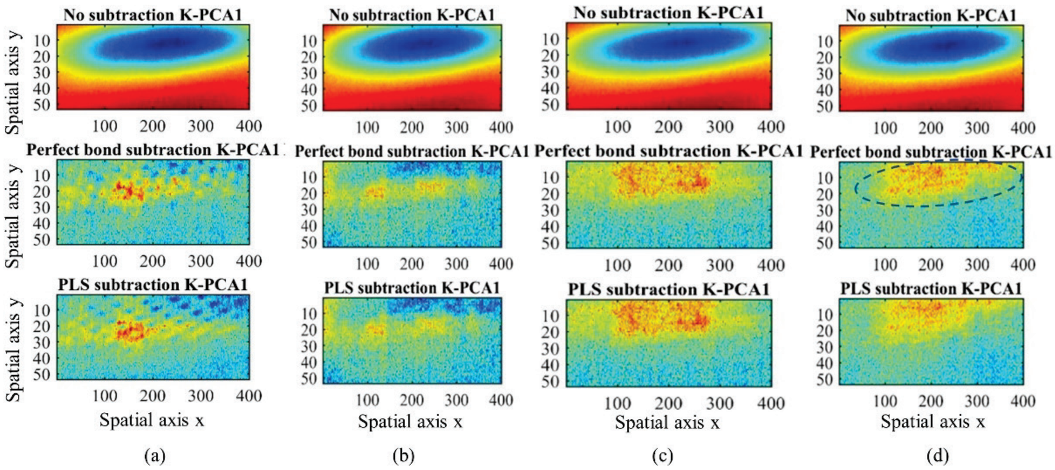

Figure 5-5 Results obtained without subtraction and with the subtraction of PLS and perfect bond

(a) Brass film, (b) Release film, (c) More release agent contamination, (d) Less release agent contamination

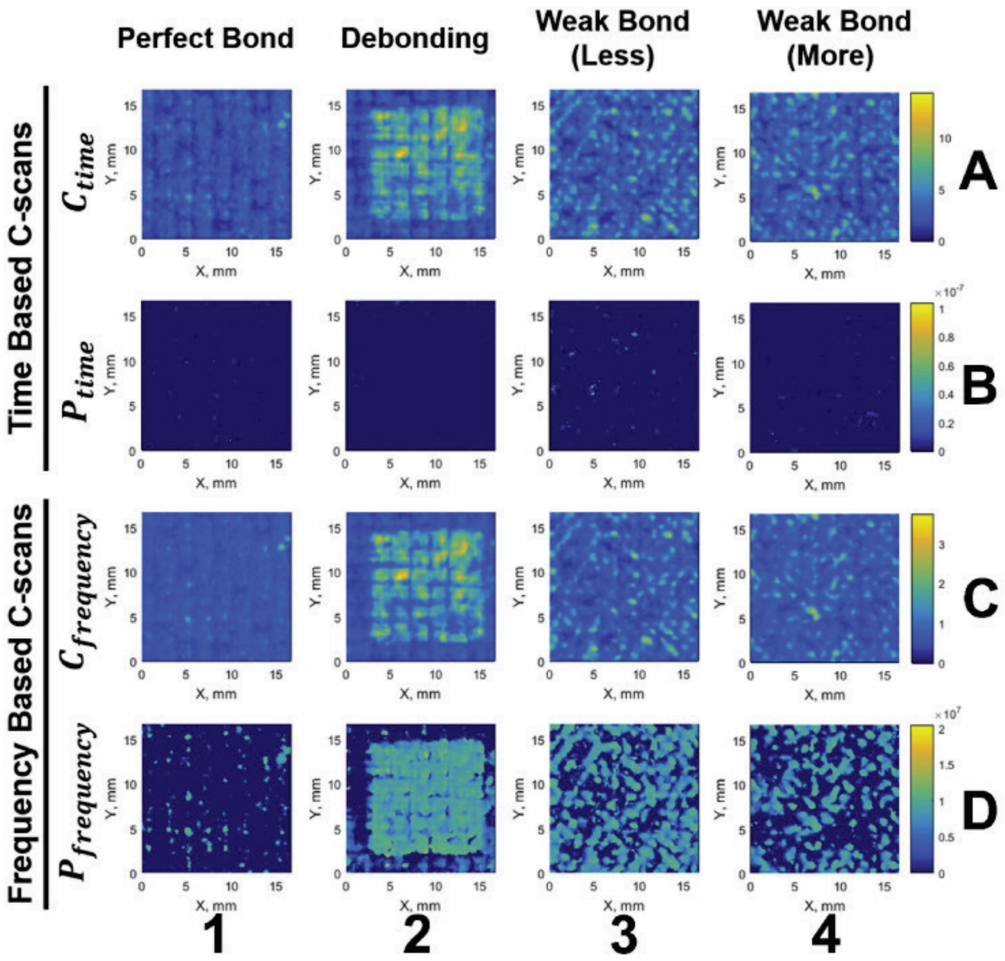

Figure 5-6 Debonding detected by acoustic microscopy

(amplitude-time based (A), phase-time based (B), amplitude-frequency based (C), phase-frequency based (D)) for four different bonding quality (perfect bond (1), debonding with release film contamination (2), weak bond with less release agent contamination (3), weak bond with more release agent contamination (4))[310]

5.4.2 Multi-physics analysis based on sliding window of K-PCA

To find the time instance carrying the maximum information about the contamination layer, physical analysis of the eddy current and thermal phenomena based on sliding K-PCA is conducted. The impulse response-based K-PCA calculation is presented in previous work [1]. The time series of the images is subdivided into non-overlapping time-windows each one having five frames. In K-PCA, the linear kernel is applied due to the limited number of data in five frames. The calculation is based on the first principal component, which can help compress major information. The physical meaning of K-PCA1 after PLS subtraction is to observe the variations of SUT's thermal response. The feature used as depth indicator is the norm of first principal component for every five frames within the first 80 frames of PLS subtracted data.

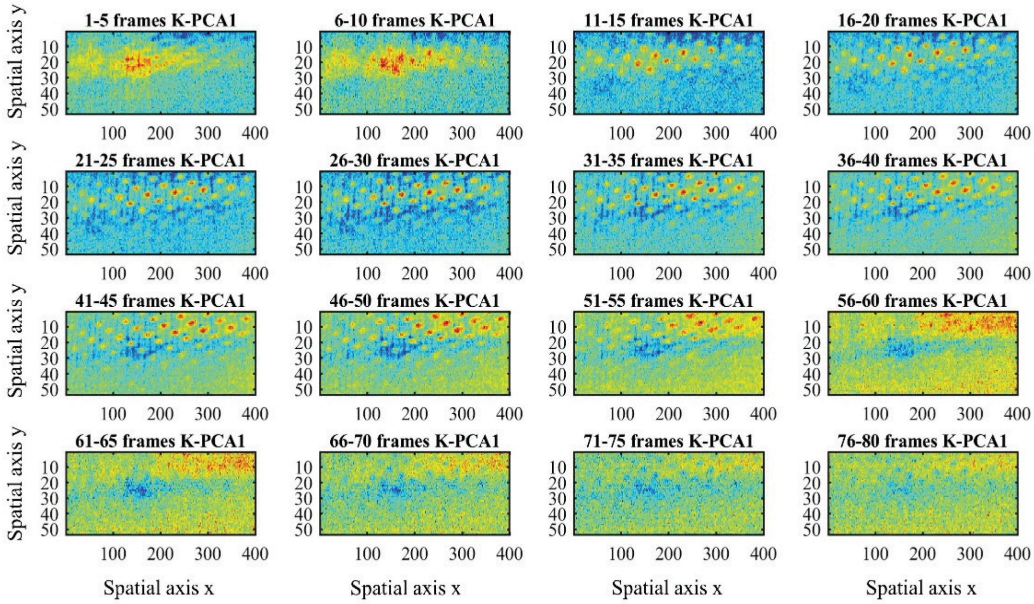

Figure 5-7. Sliding K-PCA results for brass film inclusion

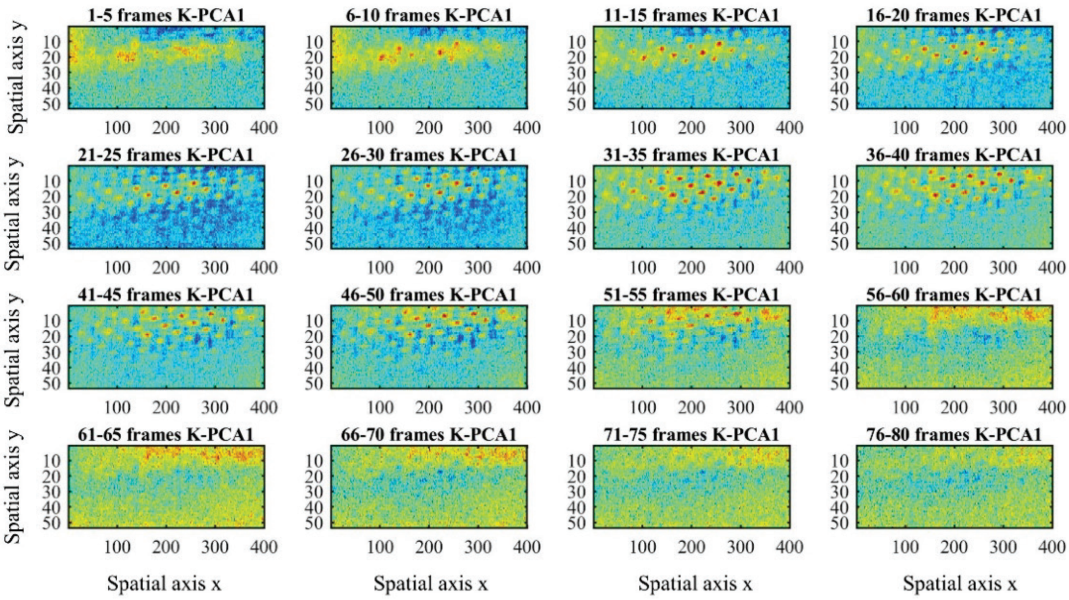

Figure 5-8 Sliding K-PCA results for release film inclusion

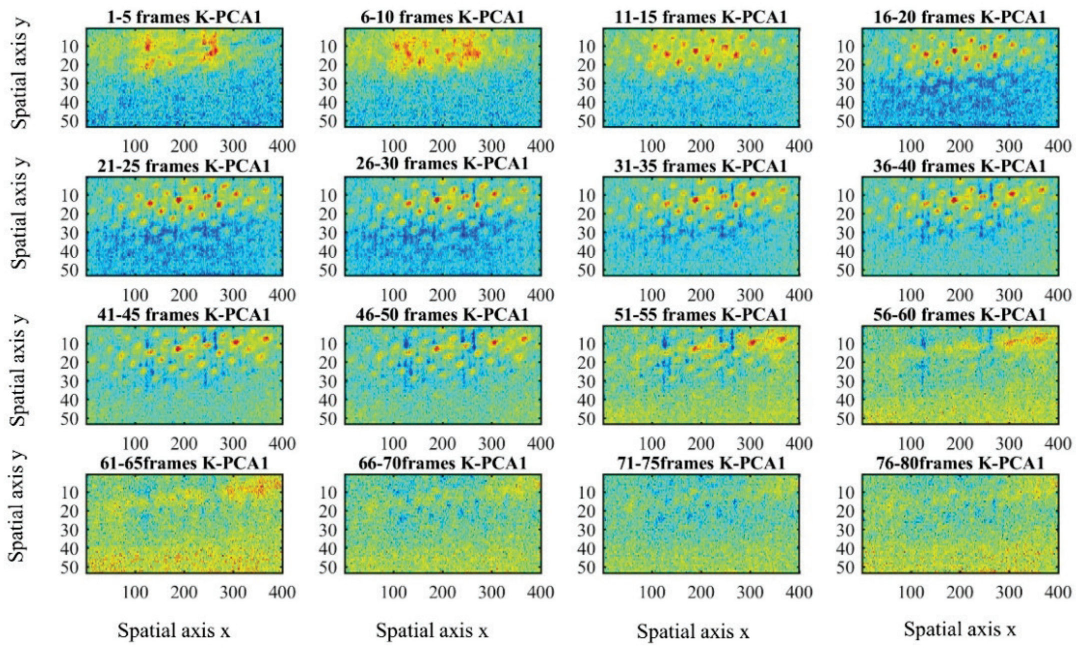

Figure 5-9 Sliding K-PCA results for the weak bond with more contamination

The Sliding K-PCA results of brass, release film and release agent inclusions are presented in Figure 5-7 to Figure 5-9 for every five frames. As shown in Figure 5-7, a higher contrast between brass and sound area is achieved in the first ten frames. This can be explained by the higher electrical conductivity of brass so that more significant eddy current density is expected than that in the surrounding CFRP and bonding material. According to [311], in the first phase of the induction heating, EC is the dominant effect. Thus the higher the conductivity, the higher the EC density and the resulting heating due to the Joule's effect. As shown in Figure 5-7 and Figure 5-8, the highest contrast is also found at the beginning for release film and release agent samples. The difference between conductive contamination (brass) and non-conductive ones (release film and release agent) is the time to reach the peak contrast. It can be seen in Figure 5-10 that it only takes five frames (100 ms) for the brass to reach its maximum contrast, but for non-conductive contaminations, it takes ten frames (200 ms). In Figure 5-7 to Figure 5-9, from frame 11 to 25, the defect pattern is covered by the response from the texture of the CFRP layer over the debonding area. Heat diffusion between the layers plays a major role in the detection of debonding: for brass film, the heat diffuses from brass to the surrounding, for release agent contamination or release film, the heat from the surrounding CFRP diffuses into the contaminated area.

Within the 80 frames, they are shown in Figure 5-10, first 15 frames indicate the maximum domination of the Joule's effect, while in the cooling stage, around frame number 60, thermal diffusion plays a significant role.

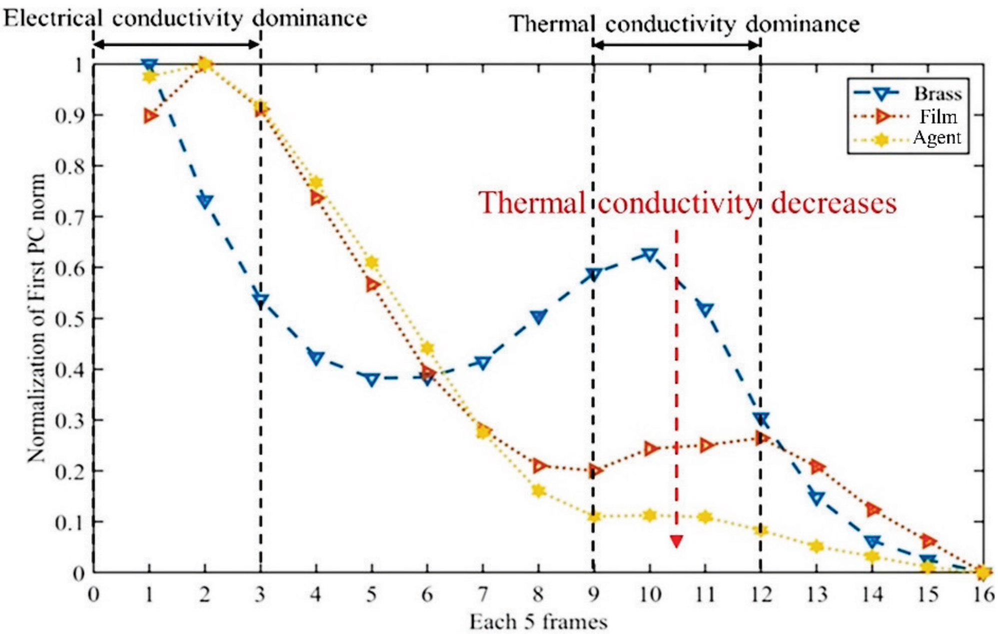

Figure 5-10 First PC norm of different contaminations versus the number of frames

5.4.3 Classification of contamination and Quantitative evaluation of size

In this section, the impulse response and its derivatives are compared to classify the thermal and electrical properties of contamination materials as well as the brass size. In Figure 5-11(a), it can be observed that at the beginning of the heating stage, the impulse response of brass rises quicker than the other two contaminations and CFRP due to its higher electrical conductivity. The release film shows the least significant response to the Joule's effect because it is not conducive. The impulse response of intact CFRP shows a slightly higher heating response than the release agent at its peak time.

It is observed that the peak value and its time instant for the brass are different from release film inclusion, which has a later peak time than the CFRP and release agent, as shown in Figure 5-11(c). After reaching the peak, the release film inclusion cools down slower than both intact CFRP and weak bond as it hampers the heat diffusion. This effect is visible in Figure 5-11(a).

However, it is challenging to evaluate the thermal conductivity of the brass contamination only by the impulse response because the Joule heating is more significant in the brass with respect to the sound CFRP surrounding area. Therefore, the heat diffuses from the brass to the surrounding area, even at the cooling stage. Thus, the derivative of the impulse response can be used to evaluate the thermal conductivity, as shown in Figure 5-11(b). Figure 5-10, and Figure 5-11(b) shows similar trends, *i.e.,* electrical conductivity plays a dominant role at around the 10th frame, while thermal conductivity shows a prominent role at the 60^{th} frame. It can be seen in Figure 5-11(b) that in the 60th frame, the absolute value of impulse response's derivative from brass has a higher value than other contaminations, proving its higher thermal conductivity. It is comparing the difference of release agent and CFRP in the heating and cooling stages in Figure 5-11(b), it is observed that the release agent has more influence on the thermal conductivity of the contaminated area than the electrical conductivity. Besides, by using the time-phase information of the impulse responses defined through Hilbert transform [31], it can be observed that the phase turning point also happens at the 60^{th} frame (see Figure 5-11(d)). Please note that the turning point happens at the same value at which there is the transition in Figure 5-10, and Figure 5-11(b).

To determine the size of contaminations, spatial kurtosis is applied to the data. The sizing data was derived from five pixels lines of data in the best contrast image. Since the size of bigger brass is $12.70\text{ mm} \times 12.70\text{ mm}$ and the smaller one has one-fourth of the area, it is observed that the spatial kurtosis of smaller ones over bigger ones is 2.05/3.30=0.62, which is slightly bigger than 0.5 for the width ratio shown in Figure 5-12. This can be caused by texture influence, which has been explained in Section 5. 4.1. For the release films, the kurtosis ratio of two same films with the same size is 3.11/2.95=1.05, which indicates their similar size as shown in

Figure 5-13.

It is proved that at first 15 and 60 frames, the physical properties of inclusions can be classified, and using the spatial kurtosis at 15^{th} frame brass size can be quantified.

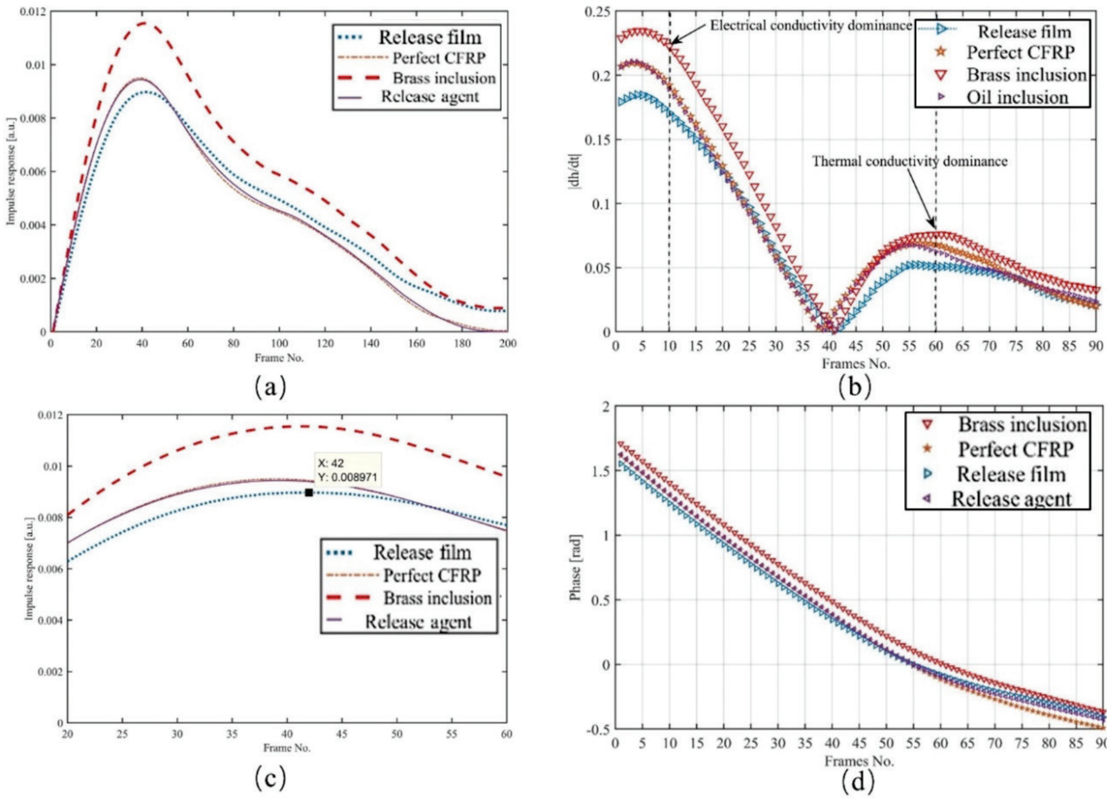

Figure 5-11 Data of different material at selected position

(a) Impulse responses, (b) Absolute value of impulse response derivatives, (a) Zoom of the peak value of impulse responses, (d) Time-phase variations of different inclusions

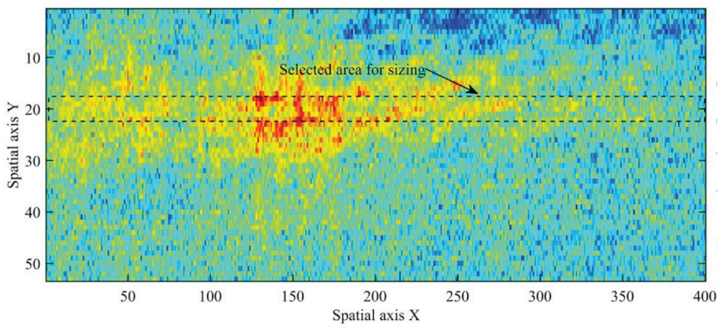

(a)

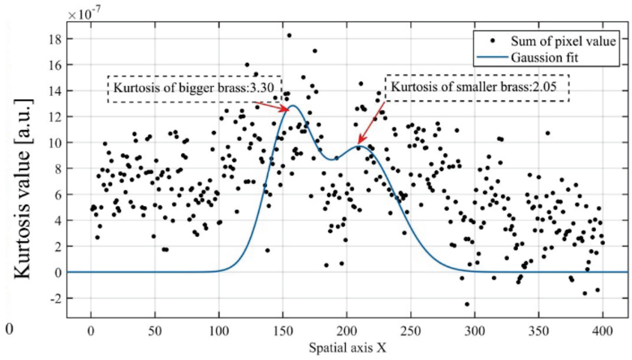

(b)

Figure 5-12 Spatial kurtosis for sizing of bigger and smaller brass films

(a) Selected area for size quantification, (b) Results of spatial kurtosis

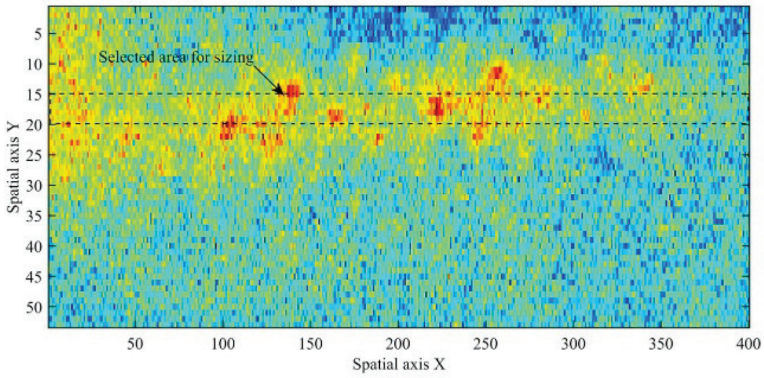

(a)

Figure 5-13 Spatial kurtosis for sizing of the release films

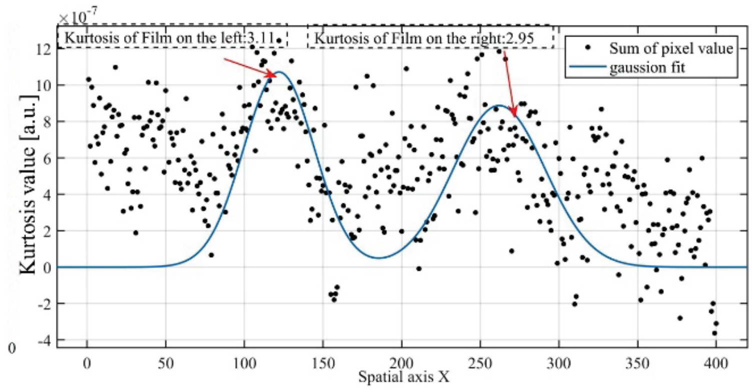

(b)

(a) Selected area for size quantification, (b) Results of spatial kurtosis

5.5 Chapter summary

This chapter focusses on the detection and evaluation of the CFRP-epoxy adhesive single-lap joints with artificially embedded contaminations of different materials in separate samples using eddy current pulse-compression thermography. Three processing steps have been applied: (1) the removal of non-uniform heating through PLS; (2) sliding Kernel Principal Component Analysis for determination of the best time interval to reveal information about contamination layer; (3) classification of contamination properties at the specific time using proposed features. The summary is as follows:

(1) PLS can remove the non-uniform heating pattern and achieve better results of perfect bond subtraction because it solves the problem of misalignment of spatial coordinates resulting from different experiments.
(2) After the removal of non-uniform heating patterns, sliding K-PCA features, and the norm of the principal component can be applied for the detection of contamination layer in heating and cooling stages. Since the eddy current can generate volumetric

Joule heating in CFRP, the first time instant of the high contrast happens at the very beginning of the retrieved impulse responses, *i.e.,* first 15 frames (300 ms), indicating the difference in contamination's electrical properties on adhesive joints. It has also been verified that the 60th frame contains the maximum information about the contaminations in the cooling stage;

(3) The debonding (contamination) proprieties can be classified using the derivatives of impulse response at a specific time. The release agent contamination has minimum influence on the electrical and thermal properties of the adhesive layer compared with brass film and release film. The release agent contamination affects the thermal properties of the adhesive epoxy layer more than the electrical properties.

This feature-based approach addresses the non-uniform heating problem with complex geometry and improves SNR for the detection and characterisation of (debonding)contaminations. The major challenge of the non-uniform heating pattern is tackled by using the PLS technique. The evaluation and quantification of the electrical and thermal properties of different contaminations are conducted by a feature-based approach. However, the feature-based approach has limitations when there is no multi-defect sample, where the relationship between features and defect parameters can be obtained. In the next section, to overcome the abovementioned issues, the work proposed the strategy of reconstruction based approaches to reconstruct the orientations of multi-layer CFRP.

Chapter 6 Inverse reconstruction of fibre orientation in Multilayer CFRP using forward FEM and eddy current pulse thermography

Feature-based QNDE techniques can inspect surface thermal distribution and cannot provide comprehensive information of carbon fibre reinforced polymer (CFRP) at a layer level, which is vital for quantitative layer characterisation indicating possible failures, e.g., fibre misalignment, debonding, etc. In this chapter, the case study of the layer orientation of multi-layer CFRP is estimated and reconstructed. Section 6.1 briefs the introduction of background for reconstruction based techniques. Section 6.2 presents the inversion strategy of two-step reconstruction, and the feature extraction technique, radon transform, for validation of the proposed techniques are introduced. Section 6.3 presents the experimental setup for model validation and reconstruction. Section 6.4 presents the outcome of the reconstruction and its comparison with feature-based techniques. The chapter summary is presented in Section 6.5 for highlighting the contribution of this work.

6.1 Introduction

ECPT (Eddy current pulsed thermography) has been reviewed in Chapter 2 used for detection, imaging, and sizing of structural imperfections for CFRP aerospace components. In ECPT, image processing based methods range from dealing with fixed pattern noise [312] to thermography signal reconstruction (TSR) algorithm [128]. With the requirement of automatic feature extraction, detection, and evaluation from industry, principal components analysis (PCA) [313], kernel principal component analysis (K-PCA), and sparse principal component analysis [314] have been implemented, which are introduced in chapter 4 and 5. However, the defect evaluation results based on these methods are highly dependent on the algorithm. For instance, the selection of a different principal component (PC) produces entirely different results, which should be supervised by human guidance [315]. Thus, the quantification accuracy may vary from the experience level of the operator. Besides, the forward solution is insufficient in the quantification of multiple parameters, e.g., when both defect size and conductivity parameters need to be quantified simultaneously. Thus, this chapter seeks to develop an inversion approach to reconstruct the three-dimensional (3D) profile of CFRP at different depths for providing a comprehensive view of the component's structure.

Reconstruction is increasingly attracting attention within the NDE community for a complementary approach compared with the above feature-based techniques. For instance, a defect shape reconstruction algorithm has been proposed for pulsed thermography [172] based on the interpretation of relative contrast between experimental data and simulated data. One drawback of these direct methods is that 2D/3D heat transfer is not considered. An alternative solution for the problem is to consider the 2D/3D heat equation as a nonlinear ill-posed problem [173]. Optimisation methods, e.g., least-squares [175], gradient search [176], Levenberg–Marquardt [171], can minimize the computed data with the experimental data through iterative calculation. By using optimisation-based inversion algorithms, the defect parameters can be approximated by minimizing the error between the theoretical and predicted data. The above solutions are promising but can be challenging when applied to the reconstruction of layered composites, which can be severely influenced by anisotropic thermal diffusion caused by the different orientations in each layer. Without considering the anisotropic behaviour of the material, time-reverse reconstruction results can be less accurate and more computationally expensive to be performed. By implementing the layer reconstruction for CFRP, the fibre misalignment or debonding at different depths can be comprehensively evaluated with better accuracy and robustness compared with feature-based techniques.

To tackle these challenges, this work uses thermal diffusion in the fibre direction to perform the reconstruction of CFRP layer information. The system diagram is presented in Figure 6-1. Firstly, experiments of multi-layer samples are conducted by the ECPT system. Then, the multilayer anisotropic CFRP is modelled by a finite element method (FEM) and validated by the experimental work. The electrical and thermal conductivities are estimated by the experimental transient response. After obtaining the electrical and thermal conductivity, iterative minimization of response from simulation and experiment is used to reconstruct orientations of each layer using the estimated conductivity. Results are validated with a feature-based approach for orientations QNDE, the radon transform, proving better accuracy and stability. It is also found that errors increase as the layer depth increases due to the diffusive nature of both electromagnetic and thermal waves.

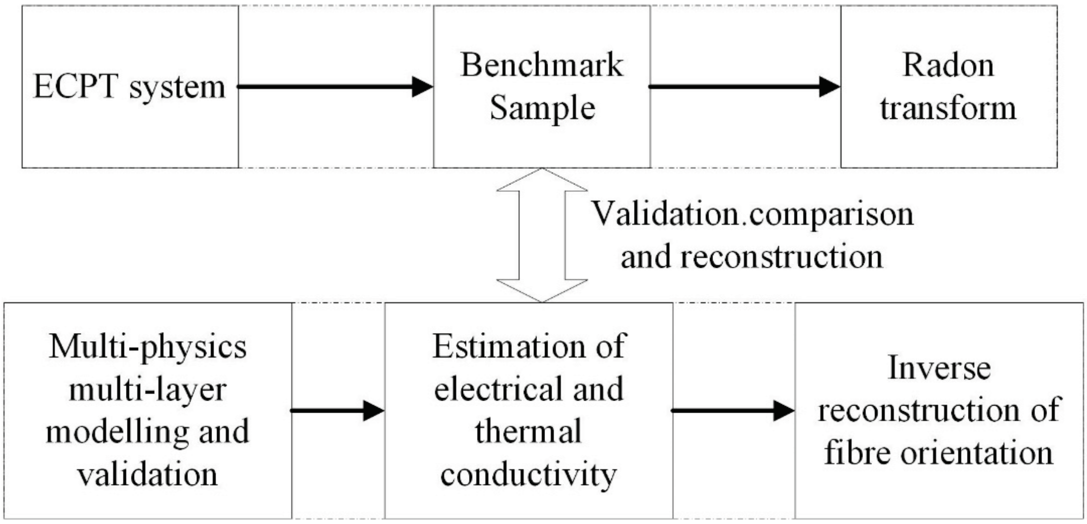

Figure 6-1 System diagram for CFRP reconstruction

6.2 Methodology introduction

As illustrated in Figure 6-1, the overall process involves two-step inversion. The first step is to estimate the electrical and thermal conductivity, while the second step is to conduct the orientation inversion based on the estimated parameters. In this part, Section 6.2.1 gives the detailed implementation of electrical and thermal conductivity estimation, while Section 6.3.1 presents the implementation for layer reconstruction.

6.2.1 Electrical and thermal conductivity estimation

To proceed with layer orientation reconstruction, electrical and thermal conductivity in the fibre direction must be estimated, which are used to calculate the conductivity of different orientations. Considering the inversion of conductivity as a nonlinearly constrained optimisation problem as follows:

$$minimize_X \; F(X) = \frac{1}{2}\left\|T_i(X) - T_{ref}\right\|^2 \tag{6.1}$$

$$subject\ to\ \ c_k(X) = X - 10 < 0$$
$$c_j(X) = 1 - \mathrm{X} < 0 \tag{6.2}$$

where X is a two-parameter vector $[\sigma_L e^{-4}, \sigma_T]$ or $[\lambda_L e^{-1}, \lambda_T]$. The former denotes the parameters of electrical conductivity in longitude and transverse direction, respectively. The latter one represents parameters of thermal conductivity in longitude and transverse direction. The constants e^{-4} and e^{-1} are used to regulate the parameters on the same level of scale. $T_i(X)$ is the output of the model, and T_{ref} is the experimental signal. The Lagrangian for this problem is:

$$\mathcal{L}(X,\zeta,\nu) = F(X) - \zeta c_k(X) - \nu c_j(X) \tag{6.3}$$

where ζ and ν are Lagrange multipliers. To implement the Eq.(6.3), at an iteration X_i, a sequential quadratic programming algorithm defines an appropriate search direction d_i as a solution to the quadratic programming sub-problem as follows:

$$\min_{d_i} F(X_i) + \Delta F(X_i)^T d_i + \frac{1}{2} {d_i}^T \Delta_{xx}^2\, \mathcal{L}(X_i, \zeta_i, \nu_i) d_i \tag{6.4}$$

$$\begin{aligned} subject\ to\ \ c_k(X_i + d_i) < 0 \\ c_j(X_i + d_i) < 0 \end{aligned} \tag{6.5}$$

The process for the detailed implementation of electrical and thermal conductivity inversion is shown in Figure 6-2. The inversion starts by optimizing the heating stage response for searching $[\sigma_L e^{-4}, \sigma_T]$, which satisfies the stopping criteria, during each iteration, the search direction of σ_{d_i} is updated by the quadratic sub-program presented in Eq. (15) and Eq. (16). The above solutions of equations (6.4) and (6.5) for estimating electrical and thermal conductivity are solved in Matlab using *fmincon* function.

The reason for using the heating response for electrical conductivity inversion is presented in [271], which illustrates that the electric current field is generated at the heating stage and eddy current quickly rises from zero to maximum, whereas heat diffusion does not play an obvious role as can be considered zero or negligible value. After obtaining the electrical conductivity from the approximation of heating response between the forward model and simulation, the values are input in the model to calculate the cooling stage response, hence deriving the thermal conductivity value. It is worth mentioning that the main purpose of the separation of the optimisation of electrical and thermal conductivity is to increase the efficiency of optimisation. Better results and accuracy can be achieved to couple the whole transient response for two objective functions(e.g.electrical and thermal conductivity). However, in this case, the starting points and the optimisation algorithm should be carefully selected and improved, which introduces more complexities to optimisations procedures and might not converge in a reasonable time.

To better quantify which period of heating is the best for electrical conductivity inversion, this work reports inversion analysis with two-time segmentations, 50 ms and 200 ms, respectively, on sample 1 for validation of the techniques and sample 2 for obtaining fibre orientation at different layers for the case study. The characteristics of each sample will be given in the next section

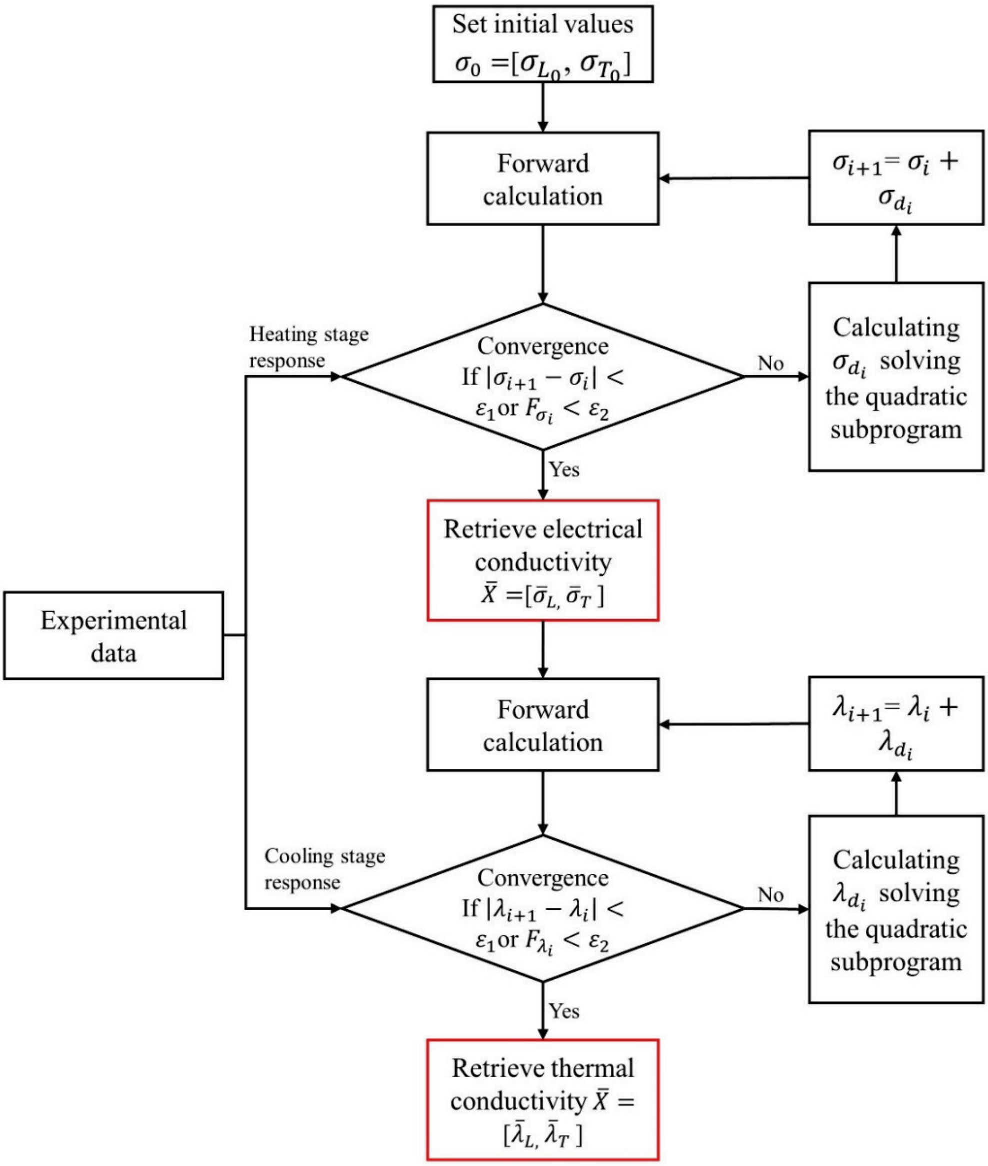

Figure 6-2 Block diagram for estimation of electrical and thermal conductivity

6.2.2 Fibre orientation inverse reconstruction

The aim of the inverse reconstruction process is to optimize the output of the forward model so as to approximate the experimental results. Hence, the objective function can be introduced as follows:

$$minimize_\theta \ f(\theta) = \frac{1}{2}\left\|T_i(\theta) - T_{ref}\right\|^2 \tag{6.6}$$

where $H_i(\theta)$ is the output of the model and T_{ref} is the experimental signal. Eq. (16) denotes the temperature-vs-time difference. Thus, the quantitative evaluation of orientation can be described as searching for the best orientation vector:

$$\hat{\theta} = \{\hat{\theta}_1, \hat{\theta}_2, \hat{\theta}_3 \dots, \hat{\theta}_N\} \in R^n \tag{6.7}$$

that make a minimal error between the measured signal T_{ref}, and forward calculated signal $H_i(\theta)$. Besides, the inversion parameters should be subject to:

$$-\frac{\pi}{2} < \hat{\theta} < \frac{\pi}{2} \tag{6.8}$$

where $-\frac{\pi}{2}$ and $\frac{\pi}{2}$ are the upper and lower limits of orientation vector $\hat{\theta}_i$.

During each layer‘s orientation search, in each iteration, the inversion parameter orientation can be solved with the following conjugate gradient algorithm as follows[21].

$$\theta_{n+1} = \begin{cases} -g_{n+1} & (n = 1) \\ -g_{n+1} + \beta_{n+1}\theta_n (n \geq 2) \end{cases} \tag{6.9}$$

$$\beta_{n+1}^{FR} = \frac{\|\beta_{n+1}\|^2}{\|\beta_n\|^2} \tag{6.10}$$

$$g_{n+1}(\theta) = \frac{\partial f(\theta)}{\partial \theta_{n+1}} \tag{6.11}$$

The schematic illustration of the inversion process for defect parameters is shown in Fig. 4. Thus, the steps of the inversion process can be summarized as follows:

1) specifying the input parameters for forward calculation, including initial fibre orientations, electrical and thermal conductivity, layer thickness, number of layers, and experimental conditions, including coil setup, excitation pulse time duration, current frequency, and amplitude.

2) initiating the forward calculation, which is governed by equations (6.1)-(6.8), to calculate the transient temperature response $T_i(\theta)$;

3) search the minimal of $f(\theta)$ using the conjugate gradient algorithm presented by equations (6.9)-(6.11).

4) establishing whether the minimization of layer i is achieved, if i <total layer number, then $i = i + 1$;

5) repeat from step 2 to step 4 until i >total layer number;

6) reconstruction completed.

6.3 Experimental setup

6.3.1Experimental system introduction

To validate the forward model for EM computation, the ECPT system shown in Figure 6-3 has been exploited. An Agilent 33500B signal generator was used to send the pulse signal to the induction heating system, and a Ref.erence clock trigger to the Infrared (IR) camera to acquire thermograms at 50 frames per second. A Cheltenham EasyHeat 224 induction heating unit is used to excite the coil with a maximum excitation power and current values of 2.40 kW and 400 A, respectively, with tunable $f_{carrier}$ from 150 kHz to 400 kHz. For the reported experimental results, values of excitation current I equal to 250 A and $f_{carrier}$ equal to 270 kHz was selected and the pulse width was set to 200 ms. Water cooling was implemented to cool down the coil, and the lift-off maintained at 1.00 mm from the sample under test (SUT). To eliminate the coil orientation with respect to a different layer, a Helmholtz coil was selected to heat the sample. The infrared camera was a FLIR SC655, equipped with an un-cooled microbolometer detector array with a resolution of 640×480 pixels, the spectral range of 7.5 - 14.0 µm and NETD < 30 mK.

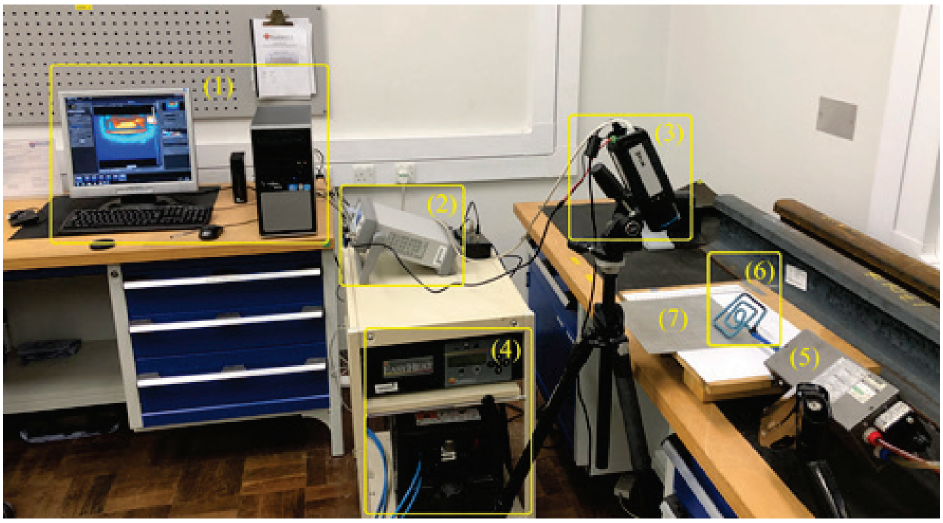

Figure 6-3 shows the experimental setup

(1) computer with software, (2) signal generator, (3) IR camera, (4) EasyHeat induction heating system, (5) work head, (6) coil, (7) sample under test

6.3.2 Sample introduction

The characteristics and geometries of the two samples used in this work are shown in Table 6-1 and Figure 6-4 respectively. SUT1 is a 2-layer [45.00, 0] quasi-isotropic sample with a thickness of 0.10 mm for each ply, of which the 2D dimension is $200mm \times 100mm$. SUT2 is also a quasi-isotropic sample with thickness of 0.90 mm for each ply , with the 2D dimension of $200mm \times 200mm$ and a layer stacking sequence [0,45.00,-45.00, 0]. Electrical and thermal conductivity in fibre direction is presented in Table I. As shown in Fig. 6, the first sample is used for validation of the model while the second is used for reconstruction of the 3D profile of the material.

Table 6-1 Sample parameters

Parameters	Value	Unit
Relative permeability	1	*1*
Electrical conductivity(fibre axis)	{39000,7.9,7.9}	*S/m*
Relative permittivity	4.3	*1*
Thermal conductivity(fibre axis)	{60, 4, 4}	*W/(m·K)*
Density	1500	*kg/m³*
Heat capacity at constant pressure	1000	*J/(kg·K)*

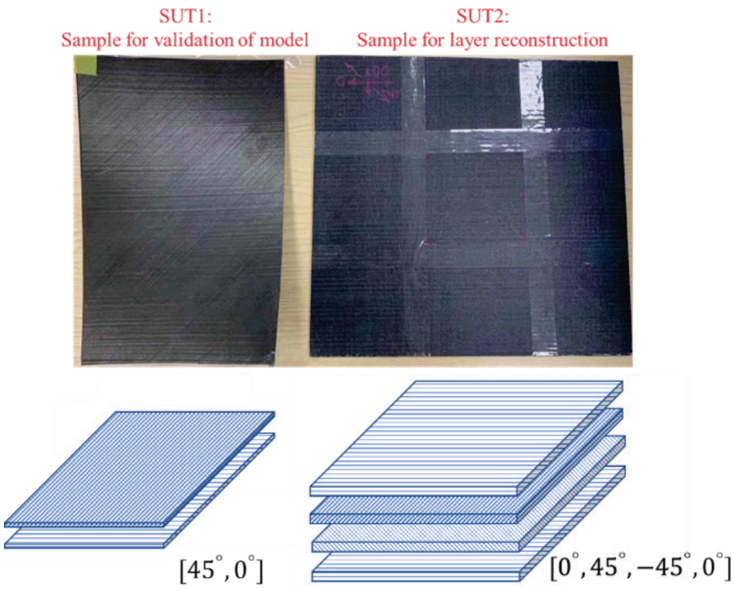

Figure 6-4 sample introduction

6.4 Results and analysis

In this section, the multi-physics and multi-layer FEM model presented in Section 3.3 is validated through experimental results. Besides, the process of electrical and thermal conductivity estimation, as well as the inversion reconstruction process, are illustrated.

6.4.1 FEM model validation using sample 1

The forward model in Section 3.3 requires to be specified and validated with an experiment to prove its effectiveness and accuracy of reconstruction. The multi-physics and multilayer model computes the transient temperature of the first sample [45.00°, 0.°]. It is shown in Figure 6-5 that the simulation data demonstrate good agreement with experimental data. There exists minor disagreement from 250 ms to 350 ms as the calculated time intervals are smaller than the IR camera's FPS. The transient response that indicates sequences of merged thermal waves can be applied to quantify the orientations of CFRP. The spatial distribution of the heating pattern induced by the Helmholtz coil is presented in Figure 6-6. Figure 6-6(a) and (b) shows that at 100 ms in the heating stage, a maximum of the heating pattern is observed along 45.00° direction, which means that interaction of the first layer with eddy currents is dominant at this stage. Figure 6-6(c) and (d) show the thermal distribution at 250 ms: the heating pattern is a superposition of the thermal responses of the first layer (45.00°) and the second layer (0°). The spatial thermal distribution caused by the time of flight of thermal waves traveling inside the media serves as the foundation for reconstructing the profile of CFRP. Additionally, the maximum temperature at 100 ms and 250 ms is 2.5 °C and 4.0 °C, respectively. This temperature rise is observed both in simulation and experiment, corroborating the model's capability and accuracy.

To validate the reconstruction approach for orientation reconstruction, the radon transform is applied as a feature extraction approach for validating the work's effectiveness and accuracy. The approach was first applied to sample 1, of which the results are shown in Figure 6-7. In Figure 6-7(a), the intensity of 45.00 degrees is much higher than that of 0°. It is observed that in Figure 6-7(b), the first layer shows its maximum sensitivity from 0 to 410 ms, reaching its peak at 410 ms. The second layer reaches its peak at 550 ms.

In the next section, the model is used as a forward calculator to iteratively compute the transient temperature response for approximating the experimental data.

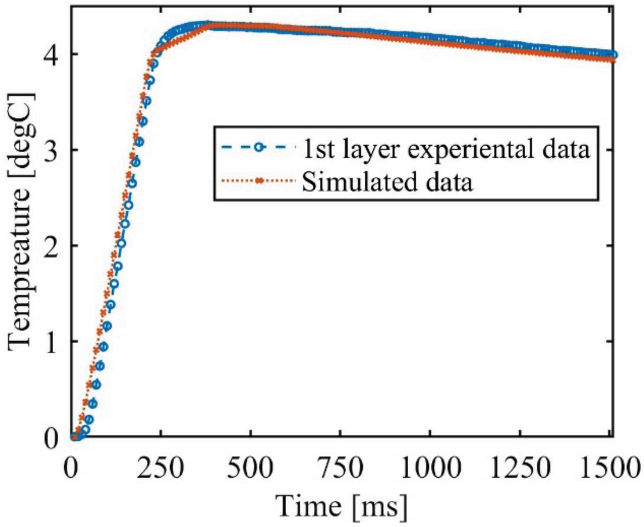

Figure 6-5 Validation of the first sample (two layers [45.00,0] using transient response)

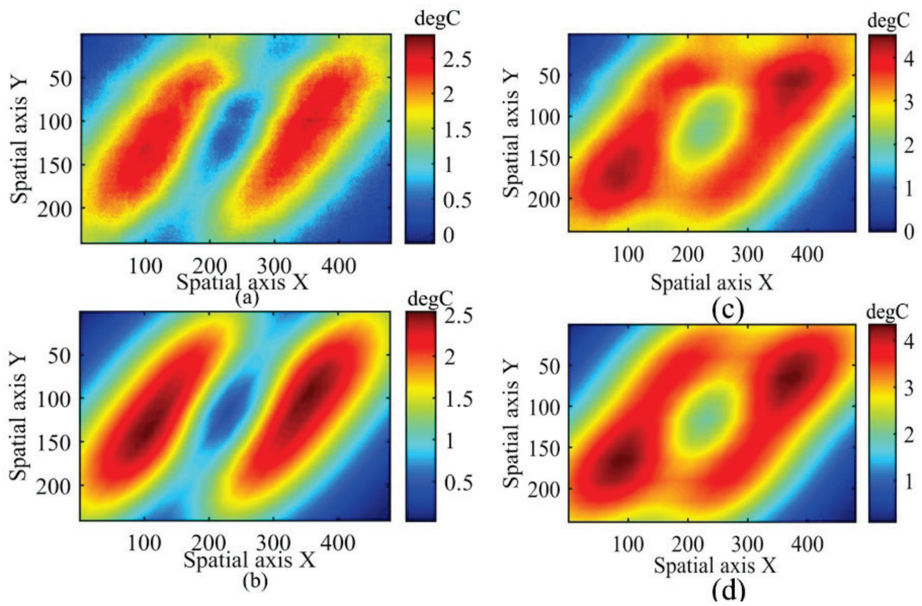

Figure 6-6 Validation of spatial thermal distribution

(a) experimental data at 100 ms, (b) simulation data at 100 ms, (c): experimental data at 250 ms, (d) simulation data at 250 ms

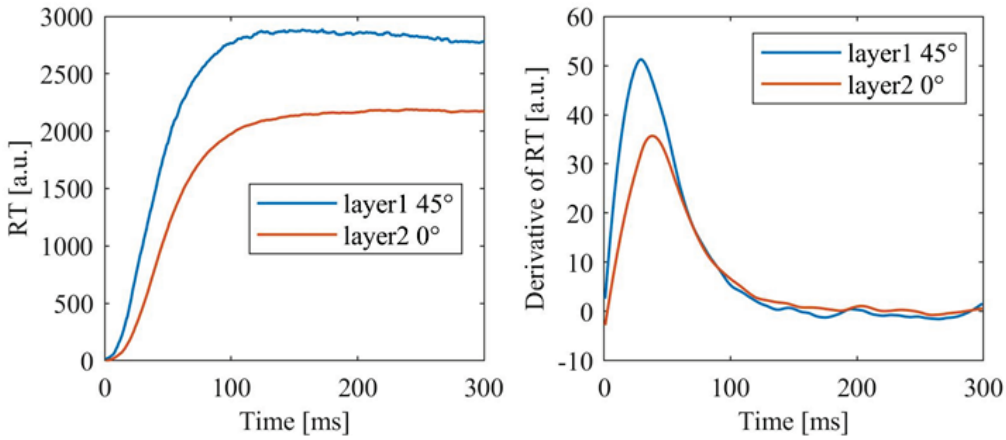

(a) (b)

Figure 6-7. Segmentation of time using radon transform based on known orientations from the first sample

(a) radon transform of each orientation vs. time, (b) Derivatives of radon transform of each orientation vs. time.

6.4.2 Estimation of electrical and thermal conductivity using sample 1&2

As mentioned in Section 6.2.1, the validated model is applied, and the conductivity values are estimated using the heating stage response for electrical conductivity and cooling stage response for thermal conductivity. For SUT1, the heating stage time segmentation is set to be 50 ms and 200 ms to investigate its influence on inversion accuracy.

The convergence plot of inversion is shown in Figure 6-8. It is worth mentioning that for sequential quadratic programming (SQP), each iteration involves sub-problem function evaluation, which is usually 3-10 times of the evaluation. Thus the total number of evaluations of the forward model is 3-10 times the iteration number shown in Figure 6-8. Figure 6-8(a) and (b) show the conductivity estimation using 200 ms heating stage data. Compared with Figure 6-8(c) and 10(d), the 200 ms setup leads to a much faster convergence speed than that of 50 ms. This is because the 200 ms time window includes more reference transient response for SQP values comparison and updating, leading to better accuracy. As for that of 50 ms heating stage response, shown in Figure 6-8(c)-(f), it requires a much smaller objective value for convergence because of the limited period for comparison.

The values updated in iteration and outcome are presented in Table 6-2 and Table 6-3. It is observed that using the first 50 ms for electrical conductivity estimation, the second sample shows better accuracy in terms of absolute error and the convergence value. This is because a thinner sample (SUT1) produces more Reflectionthan that of the thicker one, thus more dispersion of thermal waves, while for SUT2, the heating stage is less influenced by the heat diffusion, leading to better results.

Additionally, for SUT1, using a longer time increases the accuracy of inversion, as for what discussed above. In the next section, the estimated conductivity is used for reconstructing the orientations of the multilayer sample.

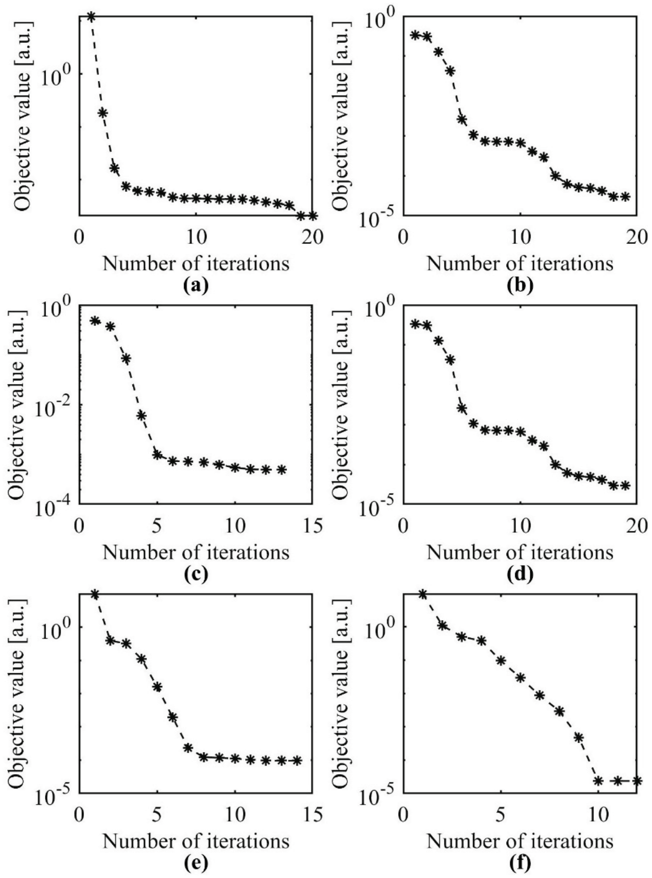

Figure 6-8 Convergence plot conductivity estimation

(a) electrical conductivity using 200 ms heating stage in sample 1,(b) thermal conductivity estimation of in sample 1, (c) 50 ms of the heating stage for electrical conductivity estimation using sample 1, (d) thermal conductivity estimation of (c) in sample 1,(e) 50 ms of the heating stage for electrical conductivity estimation using sample 2, (f) thermal conductivity estimation using the electrical conductivity of (e) in sample 2.

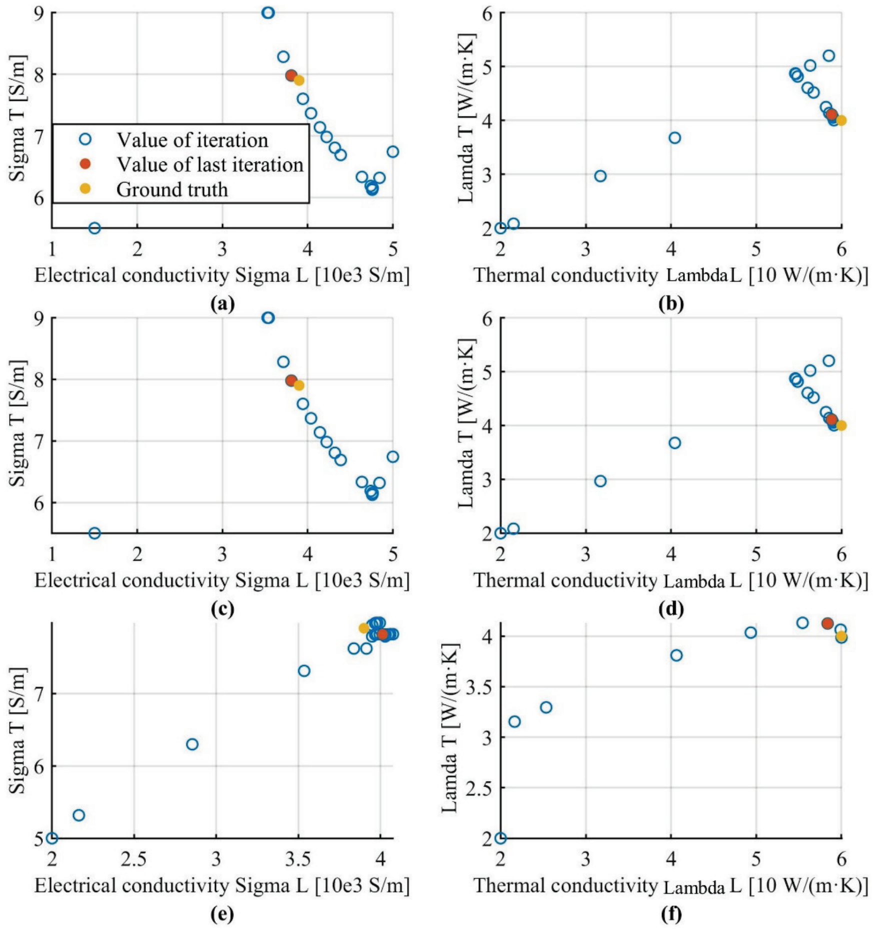

Figure 6-9 Intermediate values of conductivity estimation

(a) estimation of electrical conductivity using 200 ms heating stage in sample 1; (b) thermal conductivity estimation using the electrical conductivity of (a) in sample 1; (c) 50 ms of the heating stage for electrical conductivity estimation using sample 1; (d) thermal conductivity estimation using the electrical conductivity of (c) in sample 1; (e) 50 ms of the heating stage for electrical conductivity estimation using sample 2; (f) thermal conductivity estimation using the electrical conductivity of (e) in sample 2

Table 6-2 Estimation of thermal conductivity

Sample	$\boldsymbol{\lambda_L}$ $\mathbf{W/(m \cdot K)}$	**Error**	$\boldsymbol{\lambda_T}$ $\mathbf{W/(m \cdot K)}$	**Error**
Sample 1 (50 ms)	58.18	3.03%	4.25	6.25%
Sample 1 (200 ms)	58.84	1.93%	4.11	2.75%
Sample 2	58.70	2.10%	4.12	3.00%
Ground truth	60.00	-	4.00	-

Table 6-3 Estimation of electrical conductivity

Sample	σ_L $\mathbf{S/m}$	**Error**	σ_T $\mathbf{S/m}$	**Error**
Sample 1 (50 ms)	37752.00	3.20%	7.70	2.53%
Sample 1 (200 ms)	38090.00	2.30%	7.97	0.80%
Sample 2	40132.00	2.90%	7.82	1.01%
Ground truth	39000.00	-	7.90	-

6.4.3 Inversion analysis of orientations of multi-layer CFRP using sample 2

In this section, the validated forward model is used for the reconstruction of the four-layer sample (SUT2). The convergence plot is shown in Figure 6-10(a). Since the forward model is computationally expensive, the maximum iteration number was set to 200 as a tradeoff between efficiency and speed. The convergence plot shows the objective value calculated by Eq. (6.6). It is shown in Figure 6-10(a) that it takes 28 iterations for searching the orientation of the second layer, 72 for the third layer, and at least 100 iterations are needed for the fourth layer, which is due to the diffusive nature of eddy currents and thermal waves. In Figure 6-10(b), the optimisation process for each layer during the calculation is presented. In Figure 6-10(b), the large variance between experimental data and starting data [0.00, 0.00, 0.00, 0.00] is observed. The second layer orientation, which is supposed to be 45.00^0 Has been optimized successfully. Due to the diffusive nature of thermal waves, the orientation of layer three is obtained as -43.6^0 compared with the true value of -45.00^0. The orientation of the last layer was calculated as 4.3^0, which shows the largest error compared with that of the second and third layers.

The spatial thermal distribution during the iteration for the second layer and third layer are shown in Figure 6-12. It is observed that the change of orientation in the third layer from -21.60 to -42.60 enables the increase of first layer maximum temperature by 0.50 [degC]. It is also observed that in the first two layers, the temperature increases along with depth increases. This is because low electrical conductivity of through-thickness direction produces a high skin depth of the eddy current induced in the material. Therefore, the eddy current density is related more to the electrical conductivity of the layer, which is a function of orientation rather than the depth of the layer in the first two layers.

The surface thermal distribution of the reconstructed profile [0.0, 45.00, -42.60, 4.3] and experimental profile are shown in Figure 6-11. The change of thermal distribution at different time intervals are observed from 0° dominance at 40 ms to 45.00° dominance at 100 ms, which indicates the fact that the segmentation of layers can be conducted by segmentation of time. It is also observed that the thermal distribution of SUT2 between experiment and simulation shown in Figure 6-14 is less similar than that of the SUT1 sample shown in Figure 6-6. This is due to the fact that in a thicker sample with more layers, there is a more significant effect of diffusive thermal waves in/from each layer, which can be considered better by implementing a more accurate interface modelling in the reconstruction algorithm.

The final reconstruction profile at different depths at 200 ms is presented in Figure 6-13. It is observed that the first layer at 0 mm depth presents a super-positioned pattern with $0^{\circ}$and 45°influence. The layer at 0.90 mm is influenced more by $45^{\circ}$and less by 0°. The layer at 1.80 mm is equally influenced by $45^{\circ}$and -42.6°, showing asymmetric heating pattern with respect to the y-axis. The layer at 2.7 mm is influenced more by -42.6° and layer at 3.6 mm is influenced by 0°.

To further validate the proposed approach for layer reconstruction, the state-of-art orientation feature extraction techniques RT [303] was applied to the experimental data using the obtained/reconstructed orientations [0.0, 45.00, -42.6, 4.3]. Since the first and the fourth layers have the same orientations, only the first three orientations are used for feature extraction. It is shown in Figure 6-14(a) that the intensity of each orientation representing each layer decreases when depth increases, which proves that the reconstructed orientation for each layer is correct. Furthermore, it is observed that the derivatives of the features show different peak time as the depth increases, which also indicates the deeper the layer is, the later the peak time is.

The quantitative comparison between the proposed approach and RT is presented in Table 6-4. However, because of the overlapping of the first layer and fourth layer, it is challenging for RT to quantify different layers with the same orientations. In Table II, it is observed that when the depth increases, both methods show larger errors. The reconstruction method proves its stability and accuracy with only 2.4 and 4.3 difference compared with ground truth, while RT shows larger error than proposed methods already from layer two and the largest error of 10° difference at the fourth layer.

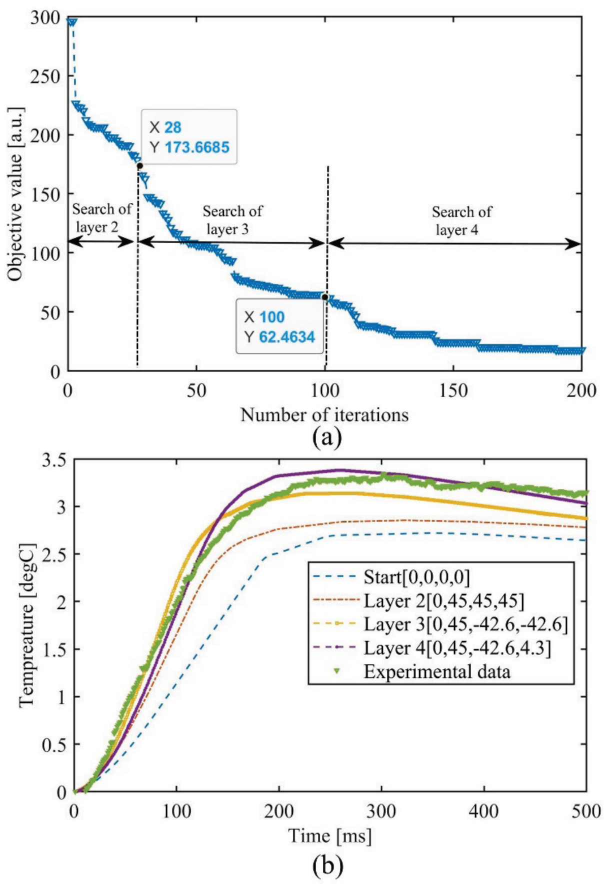

Figure 6-10 Convergence plot of orientation reconstruction

(a) convergence error during all iterations, (b) convergence of transient temperature response of each layer

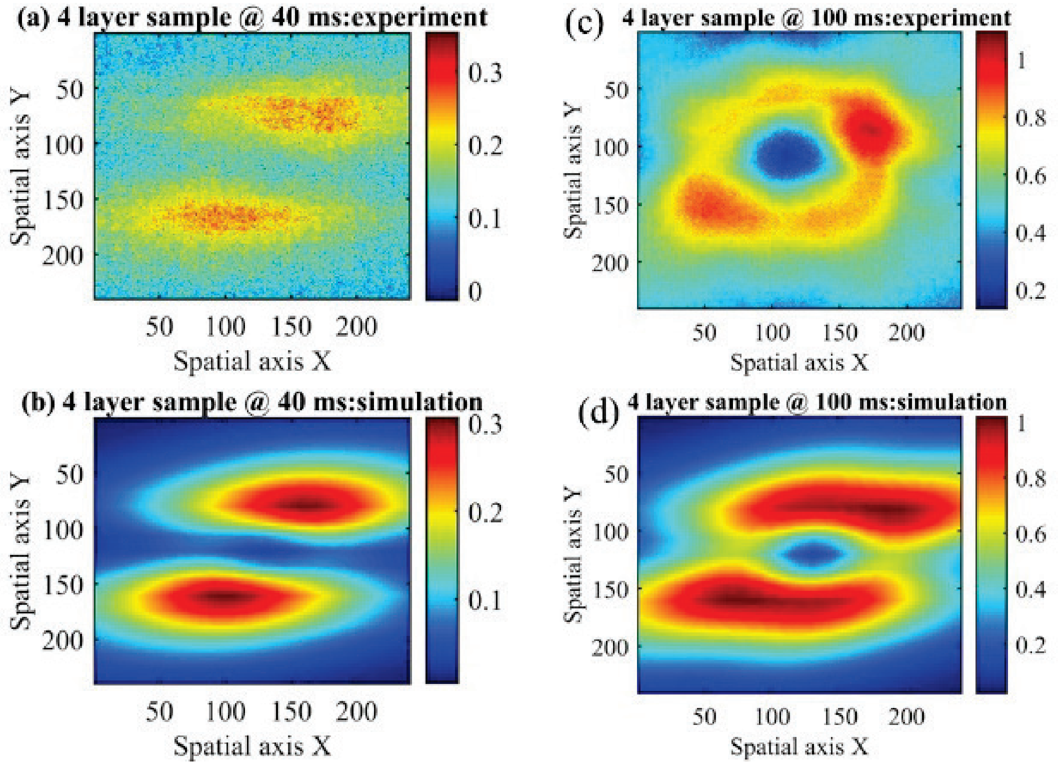

Figure 6-11 Comparison of reconstructed profile on the first layer of sample 2

(a) experimental data at 40 ms, (b) reconstructed data at 40 ms, (c) experimental data at 100ms, (d) reconstructed data at 100ms

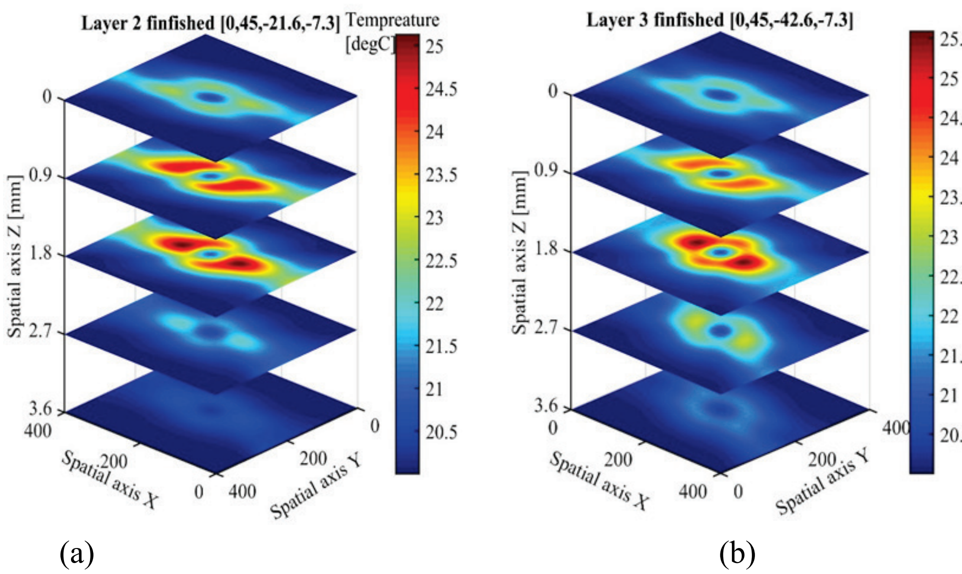

Figure 6-12 3D Reconstruction profile: (a) orientation of layer two is found, (b) orientation of layer three is found

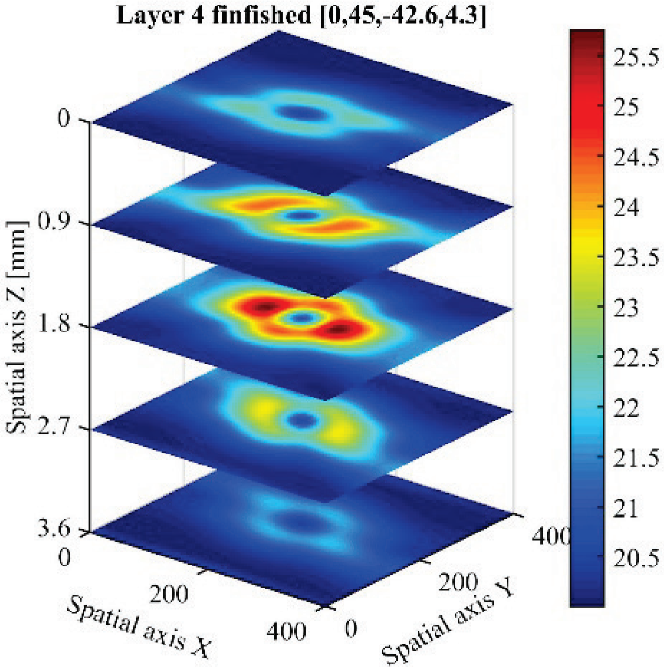

Figure 6-13 Final reconstruction profile of the four-layer sample

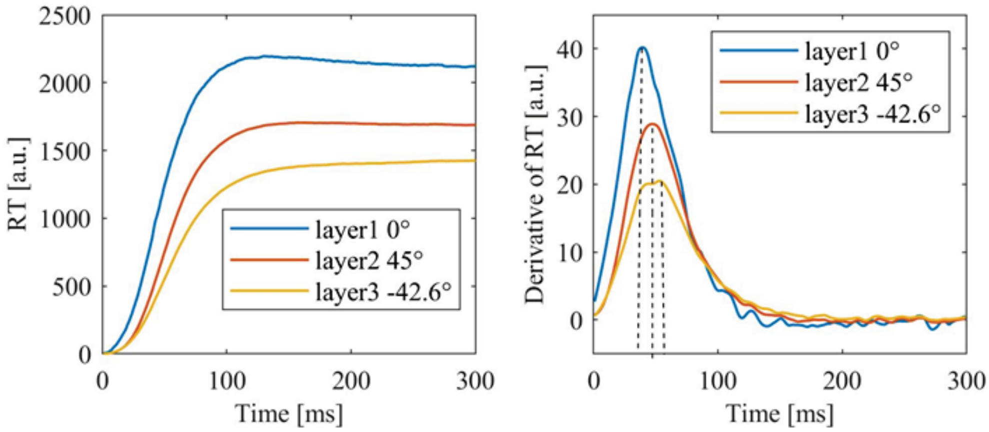

(a) (b)

Figure 6-14 Segmentation of time using random transform based on orientations from reconstruction for experimental data

(a) Random transform of each orientation vs. time, (b) Derivatives of random transform of each orientation vs. time.

Table 6-4 Comparison of error by inverse reconstruction and random transform

Ground truth	*Reconstruction*	*Error*	*Random transform*	*Error*
0.0	0.0	0.0	0.0	0.0

45.0	45.0	0.0	50.0	5.0
-45.0	-42.6	2.4	-40.0	5.0
0.0	4.3	4.3	10.0	10.0

6.5 Chapter summary

The chapter tackles with the inverse problem of ECPT for composites by reconstructing the fibre orientation, which represents the conductivity of each CFRP layer. Firstly, the multilayer anisotropic CFRP is modeled by FEM integrated with interface modelling for induction heating. Then, experiments were conducted by the ECPT system on dedicatedly designed samples with layers of different orientations. Electrical and thermal conductivity in fibre direction was estimated by approximating forward calculation and experimental data in heating and cooling stage responses, respectively. After the model was validated with experimental results and conductivity along the fibre axis was estimated, the iterative minimization of response from simulation and experiment is used to reconstruct fibre orientation in each layer.

Conclusions can be drawn as follows:

(1) Forward calculations of FEM and model of layer interface based on the sample and experimental parameters are validated by proposed time reverse reconstruction techniques and experimental data and can characterise and provide layer information at different depths. The model of layer interface can be applied for evaluation and characterisation of multilayer CFPR;

(2) The ECPT transient responses have been exploited for estimation of electrical and thermal conductivity in fibre direction using heating and cooling stage response, and the estimated values are within 6.25% error limit;

(3) The diffusive nature of thermal waves leads to larger error in reconstruction when the number of layers increased;

(4) The orientations obtained from inverse reconstruction were validated and compared by feature-based radon transform technique. It is shown that the deeper the layer, the later the peak time of the derivative is, which proves that the time of flight of thermal waves can be used to reconstruct the fibre orientations. Parameter-based

inverse reconstruction demonstrates better accuracy than the feature-based approach in terms of estimation of layer orientation

Chapter 7 Conclusions and Future Work

This chapter summarizes the whole work of the thesis and provides the conclusion of using the ECPT system for multi-layer CFRP QNDE. The contribution of each chapter 5,6 and 7 are linked and illustrated with the published journal in my Ph.D. study. Based on the current outcome, opportunities are outlined to illustrate the future path of multi-physics sensing for CFRP.

7.1 Conclusion

The thesis develops the methodology of ECPT and ECPuCT for CFRP QNDE using feature-based and reconstruction based approaches on CFRP, which are increasingly used in the aerospace industry in recent years. The thesis firstly presents the literature review, including the state-of-art of NDT techniques for CFRP and detailed discussion of eddy current and eddy current pulsed thermography in terms of modelling approaches, experimental systems, and post-processing techniques. The challenges and identify problems for further application of eddy current pulsed thermography is illustrated. The electromagnetic heating theory basis of multi-layer CFRP is detailed described from the coupling between Maxwell's equations and thermal diffusion to the volumetric heating nature of CFRP and the proposed solution for simulating multi-layer CFRP using FEM modelling. The implementation of the improvement of ECPT using the pulse compression approach is further discussed. Besides, the QNDE approaches, including feature-based and reconstruction based algorithms, are comprehensively presented. Three case studies are implemented for <u>delamination QNDE</u>, <u>debonding QNDE</u>, <u>conductivity estimation, and orientation inverse reconstruction</u> using the proposed approaches: 1) investigation of delamination with different depths in terms of detection, quantification using proposed crossing point feature and ECPuCT system; 2) investigation of debonding with different electrical and thermal properties using sliding K-PCA approaches, impulse response based features and ECPuCT system; 3) investigation of electrical and conductivity estimation, layer orientation reconstruction using ECPT system and reconstruction approaches. A summary of the outcome for individual investigation is listed as follows.

7.1.1 State-of-art of eddy current and eddy current pulsed thermography for CFRP QNDE

Carbon fibre reinforced plastics (CFRP) materials have become increasingly popular among conventional well studied engineered materials. Due to the lack of appropriate NDT&E applications of CFRP when it began to be massively produced and used in the early 21st century, the undetected defects of aerospace components pose a threat to aircraft structural integrity. To illustrate the challenges and opportunities for NDT&E of CFRP, the literature review parts firstly summarizes the significant defects in CFRP, including delamination, debonding, and impact damage. The evolution process of these defects from the fibre scale to the ply scale is reviewed. Based on the identified defects and failures, different NDT&E techniques, including phased array guided wave, active thermography, and eddy current techniques, are reviewed with its pros and cons listed. Besides, the comprehensive review of eddy current based NDT for CFRP is conducted in terms of simulation and modelling, experimental system, feature extraction methods, and the applications in the field. At the end of chapter 2, challenges and problems of multi-physics sensing are identified, including:1)Multi-layer modelling and simulation for CFRP; 2)The current ECPT system has limitations when non-uniform heating pattern affects the signature of the defect and failure; 3)The detection and evaluation of subsurface defect in CFRPs can be improved by the combination of pulse compression techniques for enhancing the detectability of subsurface defects of ECPT system; 4)The feature-based QNDE approaches have limitations when the sample has a single parameter to be estimated.

7.1.2 Feature-based QNDE for delamination in CFRP using ECPuCT

In chapter 4, to explore the capability of feature-based QNDE approach with the proposed ECPuCT for characterising delamination with different depths in CFRP laminates, different features including crossing point, skewness, and kurtosis were compared and validated. The proposed features were verified through experimental studies. This chapter concludes that 1) The K-PCA method can well extract the meaningful pattern in the impulse response behavior as time elapses, helping in locating the delamination areas effectively. 2) The proposed crossing point feature is extracted based on the crossing point of impulse response from defective and non-defective areas previously discriminated by the K-PCA method. This feature has a monotonic trend in both transmission and reflection modes for delamination depths. The feature performance in terms of linearity is better in reflection mode than in transmission mode. 3) The behavior of skewness and kurtosis feature of the impulse response illustrates the same monotonic relationship with delamination depths in transmission mode as well. Compared with other features' performance in reflection mode, the feature of the crossing point demonstrates more robustness against texture to ensure the stability in reflection mode.

7.1.3 Feature-based QNDE for debonding in CFRP using ECPuCT system

In chapter 5, the debonding of the multi-layer CFRP structure is evaluated to investigate the ECPuCT system's capability for electrical and thermal properties' quantification. Three processing steps have been applied: (1) the removal of non-uniform heating through PLS; (2) sliding Kernel Principal Component Analysis for determination of the best time interval to reveal information about the contamination layer; (3) classification of contamination properties at the specific time using proposed features. The summary is as follows:1) PLS can remove the non-uniform heating pattern and achieve better results of perfect bond subtraction; 2) After the removal of non-uniform heating patterns, sliding K-PCA features and the norm of the principal component can be applied for the detection of contamination layer in heating and cooling stages; 3) The debonding (contamination) proprieties can be classified using the derivatives of impulse response at a specific time. The results indicate that the release agent contamination has minimum influence on the electrical and thermal properties of the adhesive layer compared with brass film and release film. The release agent contamination affects the thermal properties of the adhesive epoxy layer more than the electrical properties.

7.1.4 Reconstruction based QNDE approach for multi-layer CFRP

The feature-based approach has limitations when there is no multi-defect sample, where the relationship between features and defect parameters can be obtained. Thus, in chapter 6, to overcome the issue, the work proposed the strategy of reconstruction based approach to estimate the electrical and thermal conductivity and the orientations of multi-layer CFRP. Firstly, the multilayer anisotropic CFRP is modeled by FEM integrated with interface modelling for induction heating. Then, experiments were conducted by the ECPT system on dedicatedly designed samples with layers of different orientations. Electrical and thermal conductivity in fibre direction was estimated by approximating forward calculation and experimental data in heating and cooling stage responses, respectively. After the model was validated with experimental results and conductivity along the fibre axis was estimated, the iterative minimization of response from simulation and experiment is used to reconstruct fibre orientation in each layer. The conclusions are as follws:1) Forward calculations of FEM and model of layer interface based on the sample and experimental parameters are validated; 2)The ECPT transient responses have been exploited for estimation of electrical and thermal conductivity in fibre direction using heating and cooling stage response, and the estimated values are within 6.25% error limit;3) The diffusive nature of thermal waves leads to larger error in reconstruction when the number of layers increased;

7.2 Main contribution

The main contribution of the work can be divided into four major parts:

(1) A thorough literature review of multi-physics sensing for multi-layer CFRP is carried out. The challenges in the field of simulation and modelling in terms of multi-layer modelling, the experimental system in terms of non-uniform heating patterns resulting in low SNR, and feature-based QNDE techniques limited by multi-parameters evaluation of eddy current pulsed thermography have been discussed.

(2) The combination of the pulse compression approach with the current eddy current pulsed thermography system leads the world's first ECPuCT(eddy current pulse compression thermography) system. With multiple pulse excitation and more energy delivered to the sample, the impulse response obtained by the system can be used for defect location and qualification with better accuracy. Based on the ECPuCT system, the quantitative evaluation of CFRP is extended to the evaluation of delamination and debonding in multi-layer CFRP.

The second contribution is parts of work published in :

Yi, Q., Tian, G. Y., Malekmohammadi, H., Zhu, J., Laureti, S., & Ricci, M. (2019). New features for delamination depth evaluation in carbon fibre reinforced plastic materials using eddy current pulse-compression thermography. NDT & E International, 102, 264-273.

Yi, Q., Malekmohammadi, H., Tian, G. Y., Laureti, S., & Ricci, M. (2019). Quantitative Evaluation of Crack Depths on Thin Aluminum Plate Using Eddy Current Pulse-

Compression Thermography. IEEE Transactions on Industrial Informatics, 16(6), 3963-3973.

(3) The proposal of a feature-based QNDE framework is applied for a quantitative evaluation approach for delamination and debonding in the multi-layer CFRP structure. The feature-based approach includes the kernel principal component analysis for defect location and PLS for non-uniform, crossing point, skewness, and kurtosis for quantification of defect properties. The framework of the feature-based QNDE approach shows promising capability for depth evaluation, electrical and thermal properties quantification, orientation extraction, defect sizing, which serve as guidance for multi-physics sensing, and QNDE.

The third contribution is part of work published in:

Yi, Q., Tian, G. Y., Malekmohammadi, H., Zhu, J., Laureti, S., & Ricci, M. (2019). New features for delamination depth evaluation in carbon fibre reinforced plastic materials using eddy current pulse-compression thermography. NDT & E International, 102, 264-273.

Yi, Q., Tian, G. Y., Yilmaz, B., Malekmohammadi, H., Laureti, S., Ricci, M., & Jasiuniene, E. (2019). Evaluation of debonding in CFRP-epoxy adhesive single-lap joints using eddy current pulse-compression thermography. Composites Part B: Engineering, 178, 107461.

(4) The proposal of reconstruction-based approaches to tackle with multi-parameter estimation in CFRP structure to overcome the challenges of the feature-based approach. The two-step inversion for multi-layer CFRP, including electrical and thermal conductivity estimation and layer orientation reconstruction, has proved its effectiveness and accuracy compared with feature-based approaches. The framework can guide the reconstruction of a comprehensive profile of investigated structure through optimisation between simulation and experiment.

The fourth contribution is part of the work in:

Inverse reconstruction of fiber orientation in multi-layer CFRP using forward FEM and eddy current pulsed thermography (NDT&E international:minor revision).

(5) The well-established framework for QNDE of CFRP using ECPT and ECPuCT is illustrated in Figure 7-1. The framework provides guidance for the QNDE study approach against the different targets, whether it is detection and location of the defect using K-PCA and PLST for extracting the defect signature or estimating the global

parameters such as electrical and thermal conductivity. Researchers in the community can quickly find the solution for their purpose.

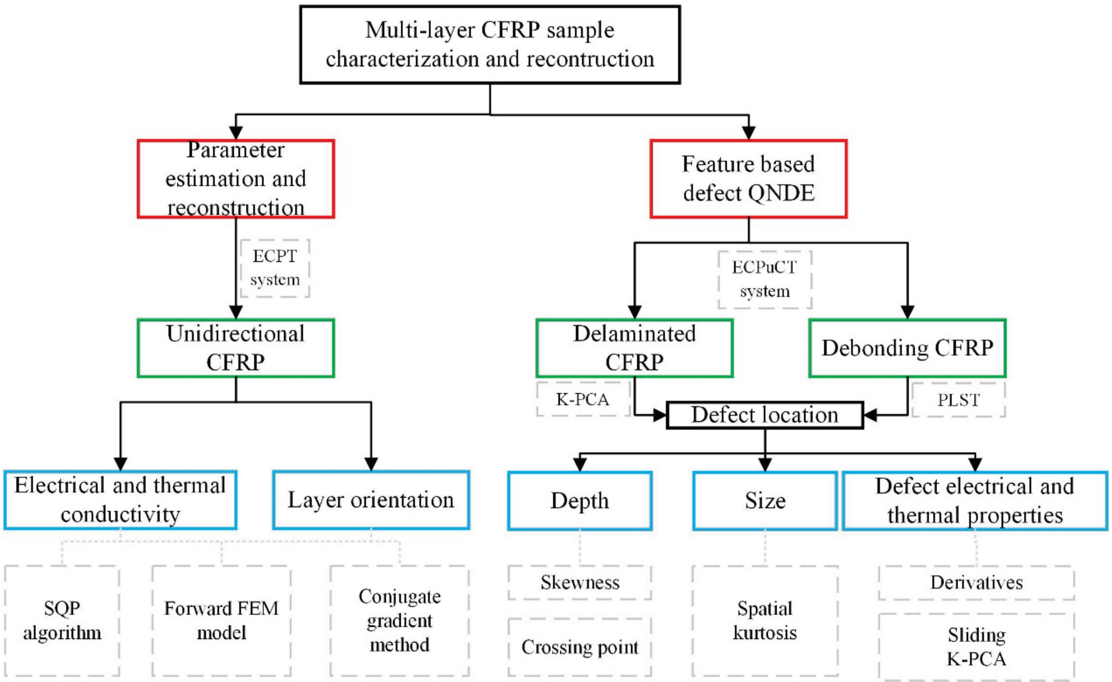

Figure 7-1 Framework for CFRP QNDE using ECPT and ECPuCT

7.3 Future work

The thesis demonstrated the capability of the ECPT system for multi-layer CFRP structure with promising directions of defect location and quantification. There are still several challenges to be tackled for future opportunities.

(1) Feature extraction, selection, and fusion for CFRP QNDE

In this work, although several features have been applied to the quantification of the different parameters of CFRP structure. The contribution of individual features to certain defects is not thoroughly investigated. In the future, using correlation analysis for quantification, the weight of each feature can further enhance the understanding of multi-physics sensing of the ECPT system. Additionally, with the contribution of each feature obtained, the feature fusion approach based on the sum of individual features can be conducted to enhance the system's detectability further.

(2) Improvement of ECPuCT system's with optimized digital coding excitation

The current ECPuCT system only applies seven digit barker codes for modulating the excitation. However, for different materials with different thermal conductivity, it is crucial to maintain the relatively large thermal diffusion depth for achieving reasonable subsurface detectability. Thus, it is required in the future to design different coded excitation,e.g.pulse width, number of pulses, different codes to adapt to the material with different electrical and thermal conductivity.

(3) Reconstruction of local defect and failure using reconstruction based QNDE

In this work, the reconstruction of parameters, including conductivity tensor and fibre orientation of CFRP structure, are limited on a global scale. However, the possible failures and defects are usually on a local scale, which poses the challenges for defect inverse reconstruction. In the future, it is suggested to extend the reconstruction approach for local defect reconstruction based on the interaction between the global model and the local model.

Reference

[1] Yi Q, Tian G, Malekmohammadi H, Zhu J, Laureti S, Ricci M. New features for delamination depth evaluation in carbon fiber reinforced plastic materials using eddy current pulse-compression thermography. NDT & E International. 2019;102:264-73.

[2] Chong AYB, Salski B, Theodorakeas P, Hatziioannidis I, Kappatos V, Selcuk C, et al. Inspection of carbon-fiber-reinforced polymer composites using radio frequency inductive sensors and ultrasonic techniques. 6th International Symposium on NDT in Aerospace2014.

[3] Dwivedi SK, Vishwakarma M, Soni A. Advances and researches on non destructive testing: A review. Materials Today: Proceedings. 2018;5:3690-8.

[4] NDTonAIR. H2020 Marie Skłodowska-Curie European Training Network. 2017.

[5] Riedel DCU, Nickel DIJ. Applications of Natural Fiber Composites for Constructive Parts in Aerospace, Automobiles, and Other Areas: Wiley-VCH Verlag GmbH & Co. KGaA; 2005.

[6] Soutis C. Fibre reinforced composites in aircraft construction. Progress in Aerospace Sciences. 2005;41:143-51.

[7] Lubin G. Handbook of composites: Springer Science & Business Media; 2013.

[8] Liu Y, Du H, Liu L, Leng J. Shape memory polymers and their composites in aerospace applications: a review. Smart Materials & Structures. 2014;23:23001-22(22).

[9] Soutis C, Irving P. Polymer Composites in the Aerospace Industry. 2015.

[10] Sun Z, Anru WU. Application of Advanced Composite in Aircraft Structures. Materials Review. 2015.

[11] Kostopoulos V, Masouras A, Baltopoulos A, Vavouliotis A, Sotiriadis G, Pambaguian L. A critical review of nanotechnologies for composite aerospace structures. Ceas Space Journal. 2017;9:35-57.

[12] Rudd CD, Long AC, Kendall K, Mangin C. Liquid moulding technologies: Resin transfer moulding, structural reaction injection moulding and related processing techniques: Elsevier; 1997.

[13] Heuer H, Schulze M, Pooch M, Gäbler S, Nocke A, Bardl G, et al. Review on quality assurance along the CFRP value chain–non-destructive testing of fabrics, preforms and CFRP by HF radio wave techniques. Composites Part B: Engineering. 2015;77:494-501.

[14] Talreja R. Manufacturing defects in composites and their effects on performance. Polymer Composites in the Aerospace Industry: Elsevier; 2014. p. 99-113.

[15] Bouloudenine A, Feliachi M, Latreche MEH. Development of circular arrayed eddy current sensor for detecting fibers orientation and in-plane fiber waviness in unidirectional CFRP. NDT & E International. 2017;92:30-7.

[16] Wang J, Potter K, Etches J. Experimental investigation and characterisation techniques of compressive fatigue failure of composites with fibre waviness at ply drops. Composite Structures. 2013;100:398-403.

[17] Sutcliffe M, Lemanski S, Scott A. Measurement of fibre waviness in industrial composite components. Composites Science and Technology. 2012;72:2016-23.

[18] Pain D, Drinkwater BW. Detection of fibre waviness using ultrasonic array scattering data. Journal of Nondestructive Evaluation. 2013;32:215-27.

[19] Bardl G, Nocke A, Cherif C, Pooch M, Schulze M, Heuer H, et al. Automated detection of yarn orientation in 3D-draped carbon fiber fabrics and preforms from eddy current data. Composites Part B: Engineering. 2016;96:312-24.

[20] Rakow JF, Pettinger AM. Failure analysis of composite structures in aircraft accidents. ISASI Annual Air Safety Seminar Cancun2006. p. 11-4.

[21] Aldave IJ, Bosom PV, González LV, De Santiago IL, Vollheim B, Krausz L, et al. Review of thermal imaging systems in composite defect detection. Infrared Physics & Technology. 2013;61:167-75.

[22] Park B, An Y-K, Sohn H. Visualization of hidden delamination and debonding in composites through noncontact laser ultrasonic scanning. Composites science and technology. 2014;100:10-8.

[23] Palumbo D, Tamborrino R, Galietti U, Aversa P, Tati A, Luprano V. Ultrasonic analysis and lock-in thermography for debonding evaluation of composite adhesive joints. NDT & E International. 2016;78:1-9.

[24] La Malfa Ribolla E, Rezaee Hajidehi M, Rizzo P, Fileccia Scimemi G, Spada A, Giambanco G. Ultrasonic inspection for the detection of debonding in CFRP-reinforced concrete. Structure and Infrastructure Engineering. 2018;14:807-16.

[25] Yang F, Cantwell W. Impact damage initiation in composite materials. Composites Science and Technology. 2010;70:336-42.

[26] Hollaway LC. A review of the present and future utilisation of FRP composites in the civil infrastructure with reference to their important in-service properties. Construction and Building Materials. 2010;24:2419-45.

[27] Rogge MD, Leckey CAC. Characterization of impact damage in composite laminates using guided wavefield imaging and local wavenumber domain analysis. Ultrasonics. 2013;53:1217-26.

[28] Shi Y, Swait T, Soutis C. Modelling damage evolution in composite laminates subjected to low velocity impact. Composite Structures. 2012;94:2902-13.

[29] He Y, Tian G, Pan M, Chen D. Impact evaluation in carbon fiber reinforced plastic (CFRP) laminates using eddy current pulsed thermography. Composite Structures. 2014;109:1-7.

[30] Zhou Y, Wang Y, Jeelani S, Xia Y. Experimental study on tensile behavior of carbon fiber and carbon fiber reinforced aluminum at different strain rate. Applied Composite Materials. 2007;14:17-31.

[31] Yu B, Blanc R, Soutis C, Withers P. Evolution of damage during the fatigue of 3D woven glass-fibre reinforced composites subjected to tension–tension loading observed by time-lapse X-ray tomography. Composites Part A: Applied Science and Manufacturing. 2016;82:279-90.

[32] Yokozeki T, Aoki T, Ogasawara T, Ishikawa T. Effects of layup angle and ply thickness on matrix crack interaction in contiguous plies of composite laminates. Composites Part A: Applied Science and Manufacturing. 2005;36:1229-35.

[33] Jolly MR, Prabhakar A, Sturzu B, Hollstein K, Singh R, Thomas S, et al. Review of non-destructive testing (NDT) techniques and their applicability to thick walled composites. Procedia CIRP. 2015;38:129-36.

[34] Katunin A, Wronkowicz-Katunin A, Dragan K. Impact damage evaluation in composite structures based on fusion of results of ultrasonic testing and X-ray computed tomography. Sensors. 2020;20:1867.

[35] Duchene P, Chaki S, Ayadi A, Krawczak P. A review of non-destructive techniques used for mechanical damage assessment in polymer composites. Journal of materials science. 2018;53:7915-38.

[36] Borum KK. Evaluation of the quality of thick fibre composites using immersion and air-coupled ultrasonic techniques. 9 European conference on non-destructive testing: German Society for Non-Destructive Testing; 2006.

[37] Kimpara I, Takehana M, Suzuki T. Analysis of thickness-direction ultrasonic wave propagation of fiberglass reinforced plastics laminates. In: ICCM/2; Proceedings of the Second International Conference on Composite Materials, Toronto, Canada, April 16-20, 1978(A79-16981 05-24) Warrendale, Pa, Metallurgical Society of AIME, 1978, p 1104-1122 Research sponsored by the Japan Craft Inspection Organization1978. p. 1104-22.

[38] Frankle RS, Rose DN. Flexible ultrasonic array system for inspecting thick composite structures. Nondestructive Evaluation of Aging Maritime Applications: International Society for Optics and Photonics; 1995. p. 51-60.

[39] Li C, Pain D, Wilcox PD, Drinkwater BW. Imaging composite material using ultrasonic arrays. NDT & E International. 2013;53:8-17.

[40] Hsu DK, Barnard DJ. Inspecting composites with airborne ultrasound: through thick and thin. AIP Conference Proceedings: AIP; 2006. p. 991-8.

[41] Revel GM, Pandarese G, Cavuto A. Advanced ultrasonic non-destructive testing for damage detection on thick and curved composite elements for constructions. Journal of Sandwich Structures & Materials. 2013;15:5-24.

[42] Caminero M, García-Moreno I, Rodríguez G, Chacón J. Internal damage evaluation of composite structures using phased array ultrasonic technique: Impact damage assessment in CFRP and 3D printed reinforced composites. Composites Part B: Engineering. 2019;165:131-42.

[43] Ashir M, Nocke A, Bulavinov A, Pinchuk R, Cherif C. Sampling phased array technology for the detection of voids in carbon fiber-reinforced plastics. The Journal of The Textile Institute. 2019;110:1703-9.

[44] Blandford BM, Jack DA. High resolution depth and area measurements of low velocity impact damage in carbon fiber laminates via an ultrasonic technique. Composites Part B: Engineering. 2020;188:107843.

[45] Hong M, Wang Q, Su Z, Zhou L. Real-time signal processing of guided waves acquired on high-speed trains for health monitoring of bogie systems. Recent Advances in Structural Integrity Analysis—Proceedings of the International Congress (APCF/SIF-2014):(APCFS/SIF 2014)2015. p. 188.

[46] Ramadas C, Hood A, Khan I, Balasubramaniam K, Joshi M. Transmission and reflection of the fundamental Lamb modes in a metallic plate with a semi-infinite horizontal crack. Ultrasonics. 2013;53:773-81.

[47] Cho Y. Estimation of ultrasonic guided wave mode conversion in a plate with thickness variation. IEEE transactions on ultrasonics, ferroelectrics, and frequency control. 2000;47:591-603.

[48] Böhm R, Hufenbach W. Experimentally based strategy for damage analysis of textile-reinforced composites under static loading. Composites science and technology. 2010;70:1330-7.

[49] Toyama N, Yashiro S, Takatsubo J, Okabe T. Stiffness evaluation and damage identification in composite beam under tension using Lamb waves. Acta materialia. 2005;53:4389-97.

[50] Su Z, Ye L, Lu Y. Guided Lamb waves for identification of damage in composite structures: A review. Journal of sound and vibration. 2006;295:753-80.

[51] Ramadas C, Padiyar J, Balasubramaniam K, Joshi M, Krishnamurthy CV. Lamb wave based ultrasonic imaging of interface delamination in a composite T-joint. NDT & E International. 2011;44:523-30.

[52] Rheinfurth M, Schmidt F, Döring D, Solodov I, Busse G, Horst P. Air-coupled guided waves combined with thermography for monitoring fatigue in biaxially loaded composite tubes. Composites science and technology. 2011;71:600-8.

[53] Chan H, Masserey B, Fromme P. High frequency guided ultrasonic waves for hidden fatigue crack growth monitoring in multi-layer model aerospace structures. Smart Materials and Structures. 2015;24:025037.

[54] Kim Y, Gaul T, Köhler B. Improved SH0 guided wave transducers based on piezoelectric fiber patches. Sensors. 2019;19:2990.

[55] Raghavan A, Cesnik CE. Guided-wave signal processing using chirplet matching pursuits and mode correlation for structural health monitoring. Smart Materials and Structures. 2007;16:355.

[56] Li J, Lu Y, Guan R, Qu W. Guided waves for debonding identification in CFRP-reinforced concrete beams. Construction and Building Materials. 2017;131:388-99.

[57] Ohtsu M, Aggelis D. Innovative AE and NDT techniques for on-site measurement of concrete and masonry structures. RILEM State Art Rep. 2016;20:89-103.

[58] Cuadra J, Vanniamparambil PA, Hazeli K, Bartoli I, Kontsos A. Damage quantification in polymer composites using a hybrid NDT approach. Composites Science and Technology. 2013;83:11-21.

[59] Sarasini F, Santulli C. Non-destructive testing (NDT) of natural fibre composites: acoustic emission technique. Natural Fibre Composites: Elsevier; 2014. p. 273-302.

[60] Gomez Munoz CQ, Garcia Marquez FP. A new fault location approach for acoustic emission techniques in wind turbines. Energies. 2016;9:40.

[61] Kordatos E, Aggelis D, Matikas T. Monitoring mechanical damage in structural materials using complimentary NDE techniques based on thermography and acoustic emission. Composites Part B: Engineering. 2012;43:2676-86.

[62] Ono K, Gallego A. Research and applications of AE on advanced composites. J Acoust Emiss. 2012;30:180-229.

[63] Gao L, Zai F, Su S, Wang H, Chen P, Liu L. Study and application of acoustic emission testing in fault diagnosis of low-speed heavy-duty gears. Sensors. 2011;11:599-611.

[64] Huang J. Non-destructive evaluation (NDE) of composites: acoustic emission (AE). Non-Destructive Evaluation (NDE) of Polymer Matrix Composites: Elsevier; 2013. p. 12-32.

[65] Whitlow T, Jones E, Przybyla C. In-situ damage monitoring of a SiC/SiC ceramic matrix composite using acoustic emission and digital image correlation. Composite Structures. 2016;158:245-51.

[66] He K, Li X. Time–frequency feature extraction of acoustic emission signals in aluminum alloy mig welding process based on SST and PCA. IEEE Access. 2019;7:113988-98.

[67] Zhao G, Zhang L, Tang C, Hao W, Luo Y. Clustering of AE signals collected during torsional tests of 3D braiding composite shafts using PCA and FCM. Composites Part B: Engineering. 2019;161:547-54.

[68] Zhou W, Zhao W-z, Zhang Y-n, Ding Z-j. Cluster analysis of acoustic emission signals and deformation measurement for delaminated glass fiber epoxy composites. Composite Structures. 2018;195:349-58.

[69] Kharrat M, Placet V, Ramasso E, Boubakar M. Influence of damage accumulation under fatigue loading on the AE-based health assessment of composite materials: Wave distortion and AE-features evolution as a function of damage level. Composites Part A: Applied Science and Manufacturing. 2018;109:615-27.

[70] Xu D, Liu P, Chen Z, Leng J, Jiao L. Achieving robust damage mode identification of adhesive composite joints for wind turbine blade using acoustic emission and machine learning. Composite Structures. 2020;236:111840.

[71] Zhao L, Kang L, Yao S. Research and application of acoustic emission signal processing technology. IEEE Access. 2018;7:984-93.

[72] Świt G, Adamczak A, Krampikowska A. Time-frequency analysis of acoustic emission signals generated by the Glass Fibre Reinforced Polymer Composites during the tensile test. IOP Conf Ser Mater Sci Eng2017. p. 1-8.

[73] Pearson MR, Eaton M, Featherston C, Pullin R, Holford K. Improved acoustic emission source location during fatigue and impact events in metallic and composite structures. Structural Health Monitoring. 2017;16:382-99.

[74] Al-Jumaili SK, Holford KM, Eaton MJ, Pullin R. Parameter Correction Technique (PCT): A novel method for acoustic emission characterisation in large-scale composites. Composites Part B: Engineering. 2015;75:336-44.

[75] Alam S, Loukili A, Grondin F, Rozière E. Use of the digital image correlation and acoustic emission technique to study the effect of structural size on cracking of reinforced concrete. Engineering Fracture Mechanics. 2015;143:17-31.

[76] Cox B, Yang Q. In quest of virtual tests for structural composites. science. 2006;314:1102-7.

[77] Tan KT, Watanabe N, Iwahori Y. X-ray radiography and micro-computed tomography examination of damage characteristics in stitched composites subjected to impact loading. Composites Part B: Engineering. 2011;42:874-84.

[78] Gholizadeh S. A review of non-destructive testing methods of composite materials. Procedia structural integrity. 2016;1:50-7.

[79] Senck S, Scheerer M, Revol V, Plank B, Hannesschläger C, Gusenbauer C, et al. Microcrack characterization in loaded CFRP laminates using quantitative two-and three-dimensional X-ray dark-field imaging. Composites Part A: Applied Science and Manufacturing. 2018;115:206-14.

[80] Bowkett M, Thanapalan K. Comparative analysis of failure detection methods of composites materials' systems. Systems Science & Control Engineering. 2017;5:168-77.

[81] du Plessis A, Boshoff WP. A review of X-ray computed tomography of concrete and asphalt construction materials. Construction and Building Materials. 2019;199:637-51.

[82] Alam MF, Haque A, Ranjith PG. A study of the particle-level fabric and morphology of granular soils under one-dimensional compression using insitu X-ray CT imaging. Materials. 2018;11:919.

[83] Di Lecce D, Marangon V, Du W, Brett DJ, Shearing PR, Hassoun J. The role of synthesis pathway on the microstructural characteristics of sulfur-carbon composites: X-ray imaging and electrochemistry in lithium battery. Journal of Power Sources. 2020;472:228424.

[84] Sencu R, Yang Z, Wang Y, Withers P, Rau C, Parson A, et al. Generation of micro-scale finite element models from synchrotron X-ray CT images for multidirectional carbon fibre reinforced composites. Composites Part A: Applied Science and Manufacturing. 2016;91:85-95.

[85] Iizuka K, Ueda M, Takahashi T, Yoshimura A, Nakayama M. Development of a three-dimensional finite element model for a unidirectional carbon fiber reinforced plastic based on X-ray computed tomography images and the numerical simulation on compression. Advanced Composite Materials. 2019;28:73-85.

[86] Pei S, Wang K, Li J, Li Y, Zeng D, Su X, et al. Mechanical properties prediction of injection molded short/long carbon fiber reinforced polymer composites using micro X-ray computed tomography. Composites Part A: Applied Science and Manufacturing. 2020;130:105732.

[87] Schöberl E, Mavrogordato M, Sinclair I, Spearing S. Fibre direction strain measurement in a composite ply under pure bending using Digital Volume Correlation and Micro-focus Computed Tomography. Journal of Composite Materials. 2020;54:1889-912.

[88] Garcea S, Wang Y, Withers P. X-ray computed tomography of polymer composites. Composites Science and Technology. 2018;156:305-19.

[89] Peng Y, Wu Y, Li S, Wang K, Yao S, Liu Z, et al. Tailorable rigidity and energy-absorption capability of 3D printed continuous carbon fiber reinforced polyamide composites. Composites Science and Technology. 2020:108337.

[90] Brombal L, Golosio B, Arfelli F, Bonazza D, Contillo A, Delogu P, et al. Monochromatic breast computed tomography with synchrotron radiation: phase-contrast and phase-retrieved image comparison and full-volume reconstruction. Journal of Medical Imaging. 2018;6:031402.

[91] Schöberl E, Breite C, Melnikov A, Swolfs Y, Mavrogordato M, Sinclair I, et al. Fibre-direction strain measurement in a composite ply under quasi-static tensile loading using Digital Volume Correlation and in situ Synchrotron Radiation Computed Tomography. Composites Part A: Applied Science and Manufacturing. 2020:105935.

[92] Wang Y, Mikkelsen LP, Pyka G, Withers PJ. Time-lapse helical X-ray computed tomography (CT) study of tensile fatigue damage formation in composites for wind turbine blades. Materials. 2018;11:2340.

[93] Stein J, Bradley RS, Yu B, Soutis C, Withers PJ. A Three Dimensional Damage Characterisation of Composites Loaded in Tension-Tension Fatigue: A Laboratory X-ray Computed Tomography Investigation. Proc of iCT conference2014. p. 67-74.

[94] Wang Y. Damage Mechanisms Associated with Kink-Band Formation in Unidirectional Fibre Composites: The University of Manchester (United Kingdom); 2016.

[95] Rolland H, Saintier N, Robert G. Damage mechanisms in short glass fibre reinforced thermoplastic during in situ microtomography tensile tests. Composites Part B: Engineering. 2016;90:365-77.

[96] Yu B, Bradley R, Soutis C, Withers P. A comparison of different approaches for imaging cracks in composites by X-ray microtomography. Philosophical Transactions of the Royal Society A: Mathematical, Physical and Engineering Sciences. 2016;374:20160037.

[97] Yu B, Bradley R, Soutis C, Hogg P, Withers P. 2D and 3D imaging of fatigue failure mechanisms of 3D woven composites. Composites Part A: Applied Science and Manufacturing. 2015;77:37-49.

[98] Jespersen KM, Zangenberg J, Lowe T, Withers PJ, Mikkelsen LP. Fatigue damage assessment of uni-directional non-crimp fabric reinforced polyester composite using X-ray computed tomography. Composites Science and Technology. 2016;136:94-103.

[99] Czabaj MW, Riccio ML, Whitacre WW. Numerical reconstruction of graphite/epoxy composite microstructure based on sub-micron resolution X-ray computed tomography. Composites Science and Technology. 2014;105:174-82.

[100] Yang Z, Ren W, Sharma R, McDonald S, Mostafavi M, Vertyagina Y, et al. In-situ X-ray computed tomography characterisation of 3D fracture evolution and image-based numerical homogenisation of concrete. Cement and Concrete Composites. 2017;75:74-83.

[101] Ayadi A, Nouri H, Guessasma S, Roger F. Large-scale X-ray microtomography analysis of fiber orientation in weld line of short glass fiber reinforced thermoplastic and related elasticity behavior. Macromolecular Materials and Engineering. 2016;301:907-21.

[102] Zhao C, Fezzaa K, Cunningham RW, Wen H, De Carlo F, Chen L, et al. Real-time monitoring of laser powder bed fusion process using high-speed X-ray imaging and diffraction. Scientific reports. 2017;7:1-11.

[103] Cawley P. Inspection of composites–current status and challenges. proceedings of 9th ECNDT, Berlin. 2006.

[104] Dapeng C, Naiming WU, Zhang Z. Defect recognition in thermosonic imaging. Chinese Journal of Aeronautics. 2012;25:657-62.

[105] Pickering S, Almond D. Matched excitation energy comparison of the pulse and lock-in thermography NDE techniques. NDT & E International. 2008;41:501-9.

[106] Sarker M, Hadigheh SA, Dias-da-Costa D. A Performance-Based Characterisation of CFRP Composite Deterioration using Active Infrared Thermography. Composite Structures. 2020:112134.

[107] Rajic N. Principal component thermography for flaw contrast enhancement and flaw depth characterisation in composite structures. Composite Structures. 2002;58:521-8.

[108] Vavilov V. Determining Limits of thermal NDT of thick graphite/epoxy composites. 9th European Conference on Nondestructive Testing, Berlin, Germany2006. p. 25-9.

[109] Toubal L, Karama M, Lorrain B. Damage evolution and infrared thermography in woven composite laminates under fatigue loading. International journal of Fatigue. 2006;28:1867-72.

[110] Harizi W, Chaki S, Bourse G, Ourak M. Mechanical damage assessment of Polymer–Matrix Composites using active infrared thermography. Composites Part B: Engineering. 2014;66:204-9.

[111] Mac VH, Huh J, Doan NS, Shin G, Lee BY. Thermography-Based Deterioration Detection in Concrete Bridge Girders Strengthened with Carbon Fiber-Reinforced Polymer. Sensors. 2020;20:3263.

[112] Fruehmann RK, Dulieu-Barton JM, Quinn S. Assessment of fatigue damage evolution in woven composite materials using infra-red techniques. Composites science and technology. 2010;70:937-46.

[113] Cinzia T, Carosena M, Maria CG. Porosity distribution in composite structures with infrared thermography. Journal of Composites. 2013;2013.

[114] Chrysafi AP, Athanasopoulos N, Siakavellas NJ. Damage detection on composite materials with active thermography and digital image processing. International Journal of Thermal Sciences. 2017;116:242-53.

[115] Yang R, He Y. Optically and non-optically excited thermography for composites: A review. Infrared Physics & Technology. 2016;75:26-50.

[116] Tabatabaei N, Mandelis A, Amaechi BT. Thermophotonic radar imaging: An emissivity-normalized modality with advantages over phase lock-in thermography. Applied Physics Letters. 2011;98:163706.

[117] Toscano C, Meola C, Carlomagno GM. Porosity distribution in composite structures with infrared thermography. Journal of Composites. 2013;2013.

[118] Zhao H, Zhou Z, Fan J, Li G, Sun G. Application of lock-in thermography for the inspection of disbonds in titanium alloy honeycomb sandwich structure. Infrared Physics & Technology. 2017;81:69-78.

[119] Ranjit S, Choi M, Kim W. Quantification of defects depth in glass fiber reinforced plastic plate by infrared lock-in thermography. Journal of Mechanical Science and Technology. 2016;30:1111-8.

[120] Balageas DL, Roche J-M. Common tools for quantitative time-resolved pulse and step-heating thermography–part I: theoretical basis. Quantitative InfraRed Thermography Journal. 2014;11:43-56.

[121] Xu Y, Hwang S, Wang Q, Kim D, Luo C, Yang J, et al. Laser active thermography for debonding detection in FRP retrofitted concrete structures. NDT & E International. 2020:102285.

[122] Ley O, Godinez-Azcuaga V. Line scanning thermography and its application inspecting aerospace composites. 5th International Symposium on NDT in Aerospace2013. p. 13-5.

[123] Fedala Y, Streza M, Sepulveda F, Roger J-P, Tessier G, Boué C. Infrared lock-in thermography crack localization on metallic surfaces for industrial diagnosis. Journal of Nondestructive Evaluation. 2014;33:335-41.

[124] Fernandes H, Zhang H, Figueiredo A, Malheiros F, Ignacio LH, Sfarra S, et al. Machine learning and infrared thermography for fiber orientation assessment on randomly-oriented strands parts. Sensors. 2018;18:288.

[125] Ciampa F, Mahmoodi P, Pinto F, Meo M. Recent advances in active infrared thermography for non-destructive testing of aerospace components. Sensors. 2018;18:609.

[126] Doshvarpassand S, Wu C, Wang X. An overview of corrosion defect characterization using active infrared thermography. Infrared Physics & Technology. 2019;96:366-89.

[127] Oswald-Tranta B. Comparative study of thermal contrast and contrast in thermal signal derivatives in pulse thermography. Ndt & E International. 2017;91:36-46.

[128] Balageas DL, Roche J-M, Leroy F-H, Liu W-M, Gorbach AM. The thermographic signal reconstruction method: a powerful tool for the enhancement of transient thermographic images. Biocybernetics and biomedical engineering. 2015;35:1-9.

[129] Oswald-Tranta B. Time and frequency behaviour in TSR and PPT evaluation for flash thermography. Quantitative InfraRed Thermography Journal. 2017;14:164-84.

[130] Shepard SM, Beemer MF. Advances in thermographic signal reconstruction. Thermosense: thermal infrared applications XXXVII: International Society for Optics and Photonics; 2015. p. 94850R.

[131] Balageas D, Chapuis B, Deban G, Passilly F. Improvement of the detection of defects by pulse thermography thanks to the TSR approach in the case of a smart composite repair patch. Quantitative InfraRed Thermography Journal. 2010;7:167-87.

[132] Beemer MF, Shepard SM. Aspect ratio considerations for flat bottom hole defects in active thermography. Quantitative InfraRed Thermography Journal. 2018;15:1-16.

[133] Roche J-M, Passilly F, Balageas D. A TSR-based quantitative processing procedure to synthesize thermal D-scans of real-life damage in composite structures. Journal of Nondestructive Evaluation. 2015;34:41.

[134] Yi Q, Malekmohammadi H, Tian GY, Laureti S, Ricci M. Quantitative Evaluation of Crack Depths on Thin Aluminum Plate Using Eddy Current Pulse-Compression Thermography. IEEE Transactions on Industrial Informatics. 2019;16:3963-73.

[135] YK Ng LU, FC Ng, LSJ Sim, E. Statistical analysis of healthy and malignant breast thermography. Journal of medical engineering & technology. 2001;25:253-63.

[136] Zeng Z, Zhou J, Tao N, Feng L, Zhang C. Absolute peak slope time based thickness measurement using pulsed thermography. Infrared Physics & Technology. 2012;55:200-4.

[137] Zeng Z, Li C, Tao N, Feng L, Zhang C. Depth prediction of non-air interface defect using pulsed thermography. Ndt & E International. 2012;48:39-45.

[138] Zhao Y, Mehnen J, Sirikham A, Roy R. A novel defect depth measurement method based on Nonlinear System Identification for pulsed thermographic inspection. Mechanical Systems and Signal Processing. 2017;85:382-95.

[139] Sirikham A, Zhao Y, Mehnen J. Determination of thermal wave reflection coefficient to better estimate defect depth using pulsed thermography. Infrared Physics & Technology. 2017;86:1-10.

[140] Madruga FJ, Ibarra-Castanedo C, Conde OM, López-Higuera JM, Maldague X. Infrared thermography processing based on higher-order statistics. Ndt & E International. 2010;43:661-6.

[141] Sfarra S, Theodorakeas P, Avdelidis N, Koui M. Thermographic, ultrasonic and optical methods: A new dimension in veneered wood diagnostics. Russian Journal of Nondestructive Testing. 2013;49:234-50.

[142] Chen X, Tian G, Ding S, Wu J. Investigation of Skewness Feature for Evaluation of Defects Using Eddy Current Pulsed Thermography. IEEE Sensors Journal. 2019;19:12118-25.

[143] Zhu J, Withers PJ, Wu J, Liu F, Yi Q, Wang Z, et al. Characterization of Rolling Contact Fatigue Cracks in Rails by Eddy Current Pulsed Thermography. IEEE Transactions on Industrial Informatics. 2020.

[144] Xu C, Zhou N, Xie J, Gong X, Chen G, Song G. Investigation on eddy current pulsed thermography to detect hidden cracks on corroded metal surface. Ndt & E International. 2016;84:27-35.

[145] Yi Q, Marindra AMJ, Zhu J, Ba A. Detection of Unknown Defects in CFRP Using Eddy Current Pulsed Thermography and Microwave NDT. 2019.

[146] Bai L, Gao B, Tian S, Cheng Y, Chen Y, Tian GY, et al. A comparative study of principal component analysis and independent component analysis in eddy current pulsed thermography data processing. Review of Scientific Instruments. 2013;84:104901.

[147] de Oliveira BC, Fröhlich HB, Barrera ES, Baldo CR, G Jr AA, Schmitt R. Impact damage characterization in CFRP plates using PCA and MEEMD decomposition methods in optical lock-in thermography phase images. Optical measurement systems for industrial inspection XI: International Society for Optics and Photonics; 2019. p. 110562N.

[148] Yousefi B, Sfarra S, Ibarra-Castanedo C, Avdelidis NP, Maldague XP. Thermography data fusion and nonnegative matrix factorization for the evaluation of cultural heritage objects and buildings. Journal of Thermal Analysis and Calorimetry. 2019;136:943-55.

[149] Edis E, Flores-Colen I, de Brito J. Quasi-quantitative infrared thermographic detection of moisture variation in facades with adhered ceramic cladding using principal component analysis. Building and Environment. 2015;94:97-108.

[150] Lu X, Yi Q, Tian G. A comparison of feature extraction techniques for delamination of CFRP using Eddy current pulse-compression thermography. IEEE Sensors Journal. 2020.

[151] Garg I, Panda P, Roy K. A low effort approach to structured cnn design using pca. IEEE Access. 2019;8:1347-60.

[152] Noori R, Karbassi A, Sabahi MS. Evaluation of PCA and Gamma test techniques on ANN operation for weekly solid waste prediction. Journal of Environmental Management. 2010;91:767-71.

[153] Liang T, Ren W, Tian GY, Elradi M, Gao Y. Low energy impact damage detection in CFRP using eddy current pulsed thermography. Composite Structures. 2016;143:352-61.

[154] Cheng L, Gao B, Tian GY, Woo WL, Berthiau G. Impact damage detection and identification using eddy current pulsed thermography through integration of PCA and ICA. IEEE Sensors Journal. 2014;14:1655-63.

[155] He Y, Du B, Huang S. Noncontact electromagnetic induction excited infrared thermography for photovoltaic cells and modules inspection. IEEE Transactions on Industrial Informatics. 2018;14:5585-93.

[156] Madhavi V, Thomas CB. Multi-view breast thermogram analysis by fusing texture features. Quantitative InfraRed Thermography Journal. 2019;16:111-28.

[157] Raghavendra U, Rajendra Acharya U, Ng E, Tan J-H, Gudigar A. An integrated index for breast cancer identification using histogram of oriented gradient and kernel locality preserving projection features extracted from thermograms. Quantitative InfraRed Thermography Journal. 2016;13:195-209.

[158] Wu J-Y, Sfarra S, Yao Y. Sparse principal component thermography for subsurface defect detection in composite products. IEEE Transactions on Industrial Informatics. 2018;14:5594-600.

[159] Mika S, Schölkopf B, Smola AJ, Müller K-R, Scholz M, Rätsch G. Kernel PCA and de-noising in feature spaces. Advances in neural information processing systems1999. p. 536-42.

[160] Wu H, Zheng K, Sfarra S, Liu Y, Yao Y. Multiview Learning for Subsurface Defect Detection in Composite Products: A Challenge on Thermographic Data Analysis. IEEE Transactions on Industrial Informatics. 2020;16:5996-6003.

[161] Meier J, Tsalicoglou I, Mennicke R. The future of NDT with wireless sensors, AI and IoT. APCNDT Conf Proc ID273/39622017.

[162] Sambath S, Nagaraj P, Selvakumar N. Automatic defect classification in ultrasonic NDT using artificial intelligence. Journal of Nondestructive Evaluation. 2011;30:20-8.

[163] Marchetti M, Boucher V, Dumoulin J, Colomb M. Retrieving visibility distance in fog combining infrared thermography, Principal Components Analysis and Partial Least-Square regression. Infrared Physics & Technology. 2015;71:289-97.

[164] Wang J, Zhao C. Visual defect recognition and location for pulsed thermography images based on defect-background contrast analysis. 2018 33rd Youth Academic Annual Conference of Chinese Association of Automation (YAC): IEEE; 2018. p. 1106-11.

[165] Liu Y, Liu K, Gao Z, Yao Y, Sfarra S, Zhang H, et al. Non-destructive defect evaluation of polymer composites via thermographic data analysis: A manifold learning method. Infrared Physics & Technology. 2019;97:300-8.

[166] Raja NSM, Fernandes S, Dey N, Satapathy SC, Rajinikanth V. Contrast enhanced medical MRI evaluation using Tsallis entropy and region growing segmentation. Journal of Ambient Intelligence and Humanized Computing. 2018:1-12.

[167] Feng Q, Gao B, Lu P, Woo WL, Yang Y, Fan Y, et al. Automatic seeded region growing for thermography debonding detection of CFRP. Ndt & E International. 2018;99:36-49.

[168] Cheng Y, Yin C, Zhang H, Huang X, Xue T, Chen K, et al. Method for separating out a defect image from a thermogram sequence based on feature extraction and multi-objective optimisation. Google Patents; 2019.

[169] Zheng K, Chang Y-S, Wang K-H, Yao Y. Thermographic clustering analysis for defect detection in CFRP structures. Polymer Testing. 2016;49:73-81.

[170] Luo Q, Gao B, Woo WL, Yang Y. Temporal and spatial deep learning network for infrared thermal defect detection. Ndt & E International. 2019;108:102164.

[171] Richter R, Maierhofer C, Kreutzbruck M. Numerical method of active thermography for the reconstruction of back wall geometry. Ndt & E International. 2013;54:189-97.

[172] Lugin S, Netzelmann U. A defect shape reconstruction algorithm for pulsed thermography. NDT & E International. 2007;40:220-8.

[173] Lopez F, de Paulo Nicolau V, Ibarra-Castanedo C, Maldague X. Thermal–numerical model and computational simulation of pulsed thermography inspection of carbon fiber-reinforced composites. International Journal of Thermal Sciences. 2014;86:325-40.

[174] Marcuzzi F, Marinetti S. Efficient reconstruction of corrosion profiles by infrared thermography. Journal of Physics: Conference Series: IOP Publishing; 2008. p. 012033.

[175] Wysocka-Fotek O, Oliferuk W, Maj M. Reconstruction of size and depth of simulated defects in austenitic steel plate using pulsed infrared thermography. Infrared Physics & Technology. 2012;55:363-7.

[176] Bu C, Tang Q, Liu Y, Yu F, Mei C, Zhao Y. Quantitative detection of thermal barrier coating thickness based on simulated annealing algorithm using pulsed infrared thermography technology. Applied Thermal Engineering. 2016;99:751-5.

[177] Junyan L, Fei W, Yang L, Yang W. Inverse methodology for identification the thermal diffusivity and subsurface defect of CFRP composite by lock-in thermographic phase (LITP) profile reconstruction. Composite Structures. 2016;138:214-26.

[178] Higuera M, Perales J, Rapún M-L, Vega J. Solving inverse geometry heat conduction problems by postprocessing steady thermograms. International Journal of Heat and Mass Transfer. 2019;143:118490.

[179] Zlobina I, Bekrenev N. The influence of electromagnatic field microwave on physical and mechanical characteristics of CFRP (carbon fiber reinforced polymer) structural. Materials Science Forum: Trans Tech Publ; 2016. p. 101-6.

[180] James R, Faisal Haider M, Giurgiutiu V, Lilienthal D. A simulative and experimental approach toward Eddy current nondestructive evaluation of manufacturing flaws and operational damage in CFRP composites. Journal of

Nondestructive Evaluation, Diagnostics and Prognostics of Engineering Systems. 2020;3.

[181] Li Z, Haigh A, Soutis C, Gibson A, Wang P. A review of microwave testing of glass fibre-reinforced polymer composites. Nondestructive Testing and Evaluation. 2019;34:429-58.

[182] Navagato MD, Narayanan RM. Microwave imaging of multilayered structures using ultrawideband noise signals. NDT & E International. 2019;104:19-33.

[183] Kharkovsky S, McClanahan A, Zoughi R, Palmer DD. Microwave dielectric-loaded rectangular waveguide resonator for depth evaluation of shallow flaws in metals. IEEE Transactions on Instrumentation and Measurement. 2011;60:3923-30.

[184] Li Z, Meng Z. A review of the radio frequency non-destructive testing for carbon-fibre composites. Measurement Science Review. 2016;16:68-76.

[185] Chizh M, Zhuravlev A, Razevig V, Ivashov S. Detection of water inclusions in honeycomb composite products by a holographic radar. 2019 IEEE International Conference on Microwaves, Antennas, Communications and Electronic Systems (COMCAS): IEEE; 2019. p. 1-5.

[186] Sutthaweekul R, Tian GY, Buhari MD. Detection of impact damage and fibre texture on CFRP using open-ended waveguide probe. 2016 13th International Conference on Electrical Engineering/Electronics, Computer, Telecommunications and Information Technology (ECTI-CON): IEEE; 2016. p. 1-6.

[187] Gäbler S, Heuer H, Heinrich G. Measuring and imaging permittivity of insulators using high-frequency eddy-current devices. IEEE Transactions on Instrumentation and Measurement. 2015;64:2227-38.

[188] Ren W, Liu J, Tian GY, Gao B, Cheng L, Yang H. Quantitative non-destructive evaluation method for impact damage using eddy current pulsed thermography. Composites Part B: Engineering. 2013;54:169-79.

[189] He Y, Tian G, Pan M, Chen D. Non-destructive testing of low-energy impact in CFRP laminates and interior defects in honeycomb sandwich using scanning pulsed eddy current. Composites Part B: Engineering. 2014;59:196-203.

[190] Stott CA, Underhill PR, Babbar VK, Krause TW. Pulsed eddy current detection of cracks in multilayer aluminum lap joints. IEEE Sensors Journal. 2015;15:956-62.

[191] Pokrass M, Burshtein Z, Gvishi R, Nathan M. Saturable absorption of multi-walled carbon nanotubes/hybrid-glass composites. Optical Materials Express. 2012;2:825-38.

[192] Li X. Eddy current techniques for non-destructive testing of carbon fibre reinforced plastic (CFRP). 2012.

[193] Woolston W. Digital eddy current system.

[194] Soutis C. Carbon fiber reinforced plastics in aircraft construction. Materials Science and Engineering: A. 2005;412:171-6.

[195] Cacciola M, Calcagno S, Megali G, Pellicano D, Versaci M, Morabito FC. Eddy current modeling in composite materials. PIERS Online. 2009;5:591-5.

[196] Cheng J, Ji H, Qiu J, Takagi T, Uchimoto T, Hu N. Role of interlaminar interface on bulk conductivity and electrical anisotropy of CFRP laminates measured by eddy current method. NDT & E International. 2014;68:1-12.

[197] Wilson J, Tian GY, Abidin IZ, Yang S, Almond D. Pulsed eddy current thermography: system development and evaluation. Insight-Non-Destructive Testing and Condition Monitoring. 2010;52:87-90.

[198] Abidin IZ, Tian GY, Wilson J, Yang S, Almond D. Quantitative evaluation of angular defects by pulsed eddy current thermography. Ndt & E International. 2010;43:537-46.

[199] Tashan J, Al-Mahaidi R. Investigation of the parameters that influence the accuracy of bond defect detection in CFRP bonded specimens using IR thermography. Composite Structures. 2012;94:519-31.

[200] Oswald-Tranta B, Shepard SM. Comparison of pulse phase and thermographic signal reconstruction processing methods. Thermosense: Thermal Infrared Applications XXXV: International Society for Optics and Photonics; 2013. p. 87050S.

[201] Wilson J, Tian GY, Abidin IZ, Yang S, Almond D. Modelling and evaluation of eddy current stimulated thermography. Nondestructive Testing and Evaluation. 2010;25:205-18.

[202] Netzelmann U, Walle G. Induction thermography as a tool for reliable detection of surface defects in forged components. 17th World Conference on Nondestructive Testing, Shanghai, China, Oct2008. p. 25-8.

[203] Tian GY, Wilson J, Cheng L, Almond DP, Kostson E, Weekes B. Pulsed eddy current thermography and applications. New Developments in Sensing Technology for Structural Health Monitoring: Springer; 2011. p. 205-31.

[204] Gbenga EE. Using non-destructive testing for the manufacturing of composites for effective cost saving: A case study of a commercial Prepreg CFC. International Journal of Materials Engineering. 2016;6:28-38.

[205] Peng Y, Huang S, He Y, Guo X. Eddy Current Pulsed Thermography for Noncontact Nondestructive Inspection of Motor Winding Defects. IEEE Sensors Journal. 2019;20:2625-34.

[206] Doirat V, Bensaid S, Fouladgar J, Berthiau G, Lefevre A. Magnetic response of anisotropic metal fiber material using homogeneous technique in ECNDT. IEEE Transactions on Magnetics. 2007;43:1777-80.

[207] Zaoui A, Menana H, Feliachi M, Berthiau G. Inverse problem in nondestructive testing using arrayed eddy current sensors. Sensors. 2010;10:8696-704.

[208] Bui HK, Wasselynck G, Trichet D, Berthiau G. Degenerated hexahedral Whitney elements for electromagnetic fields computation in multi-layer anisotropic thin regions. IEEE Transactions on Magnetics. 2016;52:1-4.

[209] Caire F, Prémel D, Granet G. Semi-analytical computation of a quasi-static field induced by an eddy current probe in a conductor with a rough surface. The European Physical Journal-Applied Physics. 2013;64.

[210] Oswald-Tranta B, Walle G, Oswald J. A semi-analytical model for the temperature distribution of thermo inductive heating. Padova, Italy: QIRT. 2006.

[211] Caire F, Prémel D, Granet G. Fast computation of the fields diffracted by a multi-layered conductor with non-parallel rough interfaces. Application to eddy-current non-destructive testing simulation. IEEE Transactions on Magnetics. 2015;51:1-4.

[212] Cheng J, Ji H, Qiu J, Takagi T, Uchimoto T, Hu N. Novel electromagnetic modeling approach of carbon fiber-reinforced polymer laminate for calculation of eddy currents and eddy current testing signals. Journal of Composite Materials. 2015;49:617-31.

[213] Xu X, Ji H, Qiu J, Cheng J, Wu Y, Takagi T. Interlaminar contact resistivity and its influence on eddy currents in carbon fiber reinforced polymer laminates. NDT & E International. 2018;94:79-91.

[214] Menana H, Feliachi M. An integro-differential model for 3-D eddy current computation in carbon fiber reinforced polymer composites. IEEE Transactions on Magnetics. 2011;47:756-63.

[215] Menana H, Féliachi M. 3-D eddy current computation in carbon-fiber reinforced composites. IEEE Transactions on Magnetics. 2009;45:1008-11.

[216] Cheng J, Qiu J, Takagi T, Uchimoto T, Hu N. Numerical analysis of correlation between fibre orientation and eddy current testing signals of carbon-fibre reinforced polymer composites. International Journal of Applied Electromagnetics and Mechanics. 2012;39:251-9.

[217] Park JB, Hwang TK, Kim HG, Doh YD. Experimental and numerical study of the electrical anisotropy in unidirectional carbon-fiber-reinforced polymer composites. Smart materials and structures. 2006;16:57.

[218] Grimberg R, Savin A, Steigmann R, Bruma A. Eddy current examination of carbon fibres in carbon-epoxy composites and Kevlar. International Journal of Materials and Product Technology. 2006;27:221-8.

[219] Menana H, Féliachi M. Modeling the response of a rotating eddy current sensor for the characterization of carbon fiber reinforced composites. The European Physical Journal-Applied Physics. 2010;52.

[220] Fang Y, Wu L, Zhang J. Excitation of plane waves for FDTD analysis of anisotropic layered media. IEEE Antennas and Wireless Propagation Letters. 2009;8:414-7.

[221] De Rosa IM, Sarasini F, Sarto MS, Tamburrano A. EMC impact of advanced carbon fiber/carbon nanotube reinforced composites for next-generation aerospace applications. IEEE Transactions on Electromagnetic Compatibility. 2008;50:556-63.

[222] Roberts TM, Sabbagh HA, Sabbagh LD. Electromagnetic interactions with an anisotropic slab. IEEE Transactions on Magnetics. 1988;24:3193-200.

[223] Bowler JR, Sabbagh LD, Sabbagh HA. A theoretical and computational model of eddy-current probes incorporating volume integral and conjugate gradient methods. IEEE Transactions on Magnetics. 1989;25:2650-64.

[224] Burke SK. Eddy-current induction in a uniaxially anisotropic plate. Journal of applied physics. 1990;68:3080-90.

[225] Chebbi H, Prémel D. The fast computation of eddy current distribution and probe response in homogenized composite material based on semi-analytical approach. The European Physical Journal Applied Physics. 2020;89:10901.

[226] Ratsakou A. Modélisation multi-physique de méthodes d'inspection par thermographie et imagerie rapide. 2020.

[227] Chandezon J, Raoult G, Maystre D. A new theoretical method for diffraction gratings and its numerical application. Journal of Optics. 1980;11:235.

[228] Caire F, Prémel D, Granet G. Semi-analytical computation of a quasi-static field induced by a 3D eddy current probe scanning a 2D layered conductor with parallel rough interfaces. International Journal of Numerical Modelling: Electronic Networks, Devices and Fields. 2014;27:600-13.

[229] Prémel D, Granet G. Development of the curvilinear coordinate method for the computation of quasi-static fields induced by an eddy current probe scanning a 3D conductor of complex shape characterized by an arbitrary 2D surface. International Journal of Numerical Modelling: Electronic Networks, Devices and Fields.

[230] Prémel D, Granet G. Fast computation of the response of any 3D Eddy Current probe scanning a 3D stratified conductor characterized by a set of arbitrary interfaces

of complex shape. International Journal of Applied Electromagnetics and Mechanics. 2019;59:1239-45.

[231] Cotter NPK, Preist TW, Sambles JR. Scattering-matrix approach to multilayer diffraction. JOSA A. 1995;12:1097-103.

[232] Li L. Formulation and comparison of two recursive matrix algorithms for modeling layered diffraction gratings. JOSA A. 1996;13:1024-35.

[233] Takagi T, Sugiura T, Miyata K, Norimatsu S, Okamura K, Miya K. Iterative solution technique for 3-D eddy current analysis using T-method. IEEE Transactions on Magnetics. 1988;24:2682-4.

[234] Albanese R, Rubinacci G. Integral formulation for 3D eddy-current computation using edge elements. IEE Proceedings A (Physical Science, Measurement and Instrumentation, Management and Education, Reviews). 1988;135:457-62.

[235] Takagi T, Hashimoto M, Arita S, Norimatsu S, Sugiura T, Miya K. Experimental verification of 3d eddy current analysis code using t-method. IEEE Transactions on Magnetics. 1990;26:474-7.

[236] Zeng Z, Udpa L, Udpa SS, Chan MSC. Reduced magnetic vector potential formulation in the finite element analysis of eddy current nondestructive testing. IEEE transactions on magnetics. 2009;45:964-7.

[237] Zeng Z, Udpa L, Udpa SS. Finite-element model for simulation of ferrite-core eddy-current probe. IEEE Transactions on Magnetics. 2010;46:905-9.

[238] Puszkarz AK, Usupov A. The study of footwear thermal insulation using thermography and the finite volume method. International Journal of Thermophysics. 2019;40:45.

[239] Ba A, Yilmaz B, Bui HK, Jasiuniene E, BERTHIAU G. Development of multi-physics multi-scale modelling platform for CFRP composites using inductive thermography techniques. AeroNDT 2018: 10th international symposium on NDT in aerospace2018. p. 1-8.

[240] Senghor FD, Wasselynck G, Bui HK, Branchu S, Trichet D, Berthiau G. Electrical conductivity tensor modeling of stratified woven-fabric carbon fiber

reinforced polymer composite materials. IEEE Transactions on Magnetics. 2017;53:1-4.

[241] Bui HK, Wasselynck G, Trichet D, Ramdane B, Berthiau G, Fouladgar J. 3-D modeling of thermo inductive non destructive testing method applied to multilayer composite. IEEE transactions on magnetics. 2013;49:1949-52.

[242] Bui H, Senghor F, Wasselynck G, Trichet D, Fouladgar J, Lee K, et al. Characterization of Electrical Conductivity of Anisotropic CFRP Materials by Means of Induction Thermography Technique. IEEE Transactions on Magnetics. 2017;54:1-4.

[243] Villière M, Lecointe D, Sobotka V, Boyard N, Delaunay D. Experimental determination and modeling of thermal conductivity tensor of carbon/epoxy composite. Composites Part A: Applied Science and Manufacturing. 2013;46:60-8.

[244] Bui HK, Senghor FD, Wasselynck G, Trichet D, Fouladgar J, Lee K, et al. Characterization of Electrical Conductivity of Anisotropic CFRP Materials by means of Induction Thermography Technique. IEEE Transactions on Magnetics. 2017.

[245] Bui H, Berthiau G, Trichet D, Wasselynck G. Inductive thermography nondestructive testing applied to carbon composite materials: multiphysics and multiscale modeling. 2015.

[246] Wu D, Cheng F, Yang F, He W. Non-destructive testing of carbon-fiber-reinforced plastics with a PCB-based TR probe. Composite Structures. 2020;240:112080.

[247] Mook G, Lange R, Koeser O. Non-destructive characterisation of carbon-fibre-reinforced plastics by means of eddy-currents. Composites science and technology. 2001;61:865-73.

[248] Heuer H, Schulze M, Pooch M. High resolution radio frequency inspection of carbon fiber composites. Microwave, Radar and Wireless Communications (MIKON), 2016 21st International Conference on: IEEE; 2016. p. 1-4.

[249] Heuer H, Schulze MH. Eddy current testing of carbon fiber materials by high resolution directional sensors. Smart Materials, Structures and NDT in Aerospace, NDT in Canada. 2011;2011.

[250] Hughes R, Fan Y, Dixon S. Near electrical resonance signal enhancement (NERSE) in eddy-current crack detection. NDT & E International. 2014;66:82-9.

[251] Ryosi A, Valentino M, Peluso G, Pepe G. Analysis of low-velocity impact damage in reinforced carbon fiber composites by HTS-SQUID magnetometers. IEEE transactions on applied superconductivity. 2001;11:1172-5.

[252] Hatsukade Y, Kasai N, Takashima H, Ishiyama A. Non-contact SQUID-NDT method using a ferrite core for carbon-fibre composites. Superconductor science and technology. 2002;15:1728.

[253] Cheng J, Qiu J, Ji H, Wang E, Takagi T, Uchimoto T. Application of low frequency ECT method in noncontact detection and visualization of CFRP material. Composites Part B: Engineering. 2017;110:141-52.

[254] Clauzon T, Thollon F, Nicolas A. Flaws characterization with pulsed eddy currents NDT. IEEE transactions on Magnetics. 1999;35:1873-6.

[255] Shu L, Songling H, Wei Z, Peng Y. Improved immunity to lift-off effect in pulsed eddy current testing with two-stage differential probes. Russian journal of nondestructive testing. 2008;44:138-44.

[256] Pirani A, Ricci M, Specogna R, Tamburrino A, Trevisan F. Multi-frequency identification of defects in conducting media. Inverse Problems. 2008;24:035011.

[257] Tian GY, Yin A, Gao B, Zhang J, Shaw B. Eddy current pulsed thermography for fatigue evaluation of gear. AIP Conference Proceedings: AIP; 2014. p. 1652-62.

[258] Yi Q, Tian G, Chebbi H, Prémel D. Investigation of layer interface model of multi-layer structure using semi-analytical and FEM analysis for eddy current pulsed thermography. 2020 IEEE International Instrumentation and Measurement Technology Conference (I2MTC): IEEE; 2020. p. 1-5.

[259] Tian GY, Sophian A, Taylor D, Rudlin J. Multiple sensors on pulsed eddy-current detection for 3-D subsurface crack assessment. IEEE Sensors Journal. 2005;5:90-6.

[260] Tian GY, Sophian A. Reduction of lift-off effects for pulsed eddy current NDT. NDT & E International. 2005;38:319-24.

[261] He Y, Luo F, Pan M, Weng F, Hu X, Gao J, et al. Pulsed eddy current technique for defect detection in aircraft riveted structures. NDT & E International. 2010;43:176-81.

[262] Gao B, Bai L, Woo WL, Tian G. Thermography pattern analysis and separation. Applied Physics Letters. 2014;104:251902.

[263] Marinetti S, Grinzato E, Bison PG, Bozzi E, Chimenti M, Pieri G, et al. Statistical analysis of IR thermographic sequences by PCA. Infrared Physics & Technology. 2004;46:85-91.

[264] Costache GN, Corcoran P, Puslecki P. Combining PCA-based datasets without retraining of the basis vector set. Pattern Recognition Letters. 2009;30:1441-7.

[265] He Y, Pan M, Luo F. Defect characterisation based on heat diffusion using induction thermography testing. Review of scientific instruments. 2012;83:104702.

[266] Yang H, Gao B, Tian G, Ren W, Woo WL. Transient-spatial pattern mining of eddy current pulsed thermography using wavelet transform. Chinese Journal of Mechanical Engineering. 2014;27:768-78.

[267] Pan M, He Y, Tian G, Chen D, Luo F. Defect characterisation using pulsed eddy current thermography under transmission mode and NDT applications. Ndt & E International. 2012;52:28-36.

[268] Oswald-Tranta B, Sorger M, O'Leary PL. Thermographic crack detection and failure classification. Journal of Electronic Imaging. 2010;19:031204.

[269] Oswald-Tranta B, Sorger M, O’Leary P. Motion deblurring of infrared images from a microbolometer camera. Infrared Physics & Technology. 2010;53:274-9.

[270] Oswald-Tranta B, Sorger M. Localizing surface cracks with inductive thermographical inspection: from measurement to image processing. Quantitative InfraRed Thermography Journal. 2011;8:149-64.

[271] Yin A, Gao B, Yun Tian G, Woo WL, Li K. Physical interpretation and separation of eddy current pulsed thermography. Journal of Applied Physics. 2013;113:064101.

[272] Gao B, Bai L, Woo WL, Tian GY, Cheng Y. Automatic defect identification of eddy current pulsed thermography using single channel blind source separation. IEEE Transactions on Instrumentation and Measurement. 2014;63:913-22.

[273] Gao B, Yin A, Tian G, Woo WL. Thermography spatial-transient-stage mathematical tensor construction and material property variation track. International Journal of Thermal Sciences. 2014;85:112-22.

[274] Yang R, He Y. Eddy current pulsed phase thermography considering volumetric induction heating for delamination evaluation in carbon fiber reinforced polymers. Applied Physics Letters. 2015;106:234103.

[275] Yang R, He Y. Pulsed inductive thermal wave radar (PI-TWR) using cross correlation matched filtering in eddy current thermography. Infrared Physics & Technology. 2015;71:469-74.

[276] Goidescu C, Welemane H, Garnier C, Fazzini M, Brault R, Péronnet E, et al. Damage investigation in CFRP composites using full-field measurement techniques: combination of digital image stereo-correlation, infrared thermography and X-ray tomography. Composites Part B: Engineering. 2013;48:95-105.

[277] Schulze MH, Heuer H, Küttner M, Meyendorf N. High-resolution eddy current sensor system for quality assessment of carbon fiber materials. Microsystem technologies. 2010;16:791-7.

[278] He Y, Yang R. Eddy current volume heating thermography and phase analysis for imaging characterization of interface delamination in CFRP. IEEE Transactions on Industrial Informatics. 2015;11:1287-97.

[279] Cheng L, Tian GY. Transient thermal behavior of eddy-current pulsed thermography for nondestructive evaluation of composites. IEEE Transactions on Instrumentation and Measurement. 2013;62:1215-22.

[280] Bonavolonta C, Peluso G, Pepe GP, Valentino M. Detection of early stage damage in carbon fiber reinforced polymers for aeronautical applications using an HTS SQUID magnetometer. The European Physical Journal B-Condensed Matter and Complex Systems. 2004;42:491-6.

[281] Koyama K, Hoshikawa H, Hirano T. Investigation of impact damage of carbon fiber rainforced plastic (CFRP) by eddy current non-destructive testing. International Workshop Smart Materials, Structures & NDT in Aerospace2011. p. 2-4.

[282] Cheng L, Tian GY. Surface crack detection for carbon fiber reinforced plastic (CFRP) materials using pulsed eddy current thermography. IEEE Sensors Journal. 2011;11:3261-8.

[283] Yi Q, Tian G, Yilmaz B, Malekmohammadi H, Laureti S, Ricci M, et al. Evaluation of debonding in CFRP-epoxy adhesive single-lap joints using eddy current pulse-compression thermography. Composites Part B: Engineering. 2019;178:107461.

[284] Cheng L, Tian GY. Comparison of nondestructive testing methods on detection of delaminations in composites. Journal of sensors. 2012;2012.

[285] Yang R, He Y. Polymer-matrix composites carbon fibre characterisation and damage inspection using selectively heating thermography (SeHT) through electromagnetic induction. Composite Structures. 2016;140:590-601.

[286] Yilmaz B, Ba A, Jasiuniene E, Bui HK, Berthiau G. Comparison of different non-destructive testing techniques for bonding quality evaluation. 2019 IEEE 5th International Workshop on Metrology for AeroSpace (MetroAeroSpace): IEEE; 2019. p. 92-7.

[287] Koyama K, Hoshikawa H, Hirano T. Investigation of impact damage of carbon fiber reinforced plastic (CFRP) by eddy current nondestructive testing. Smart Materials, Structures & NDT in Aerospace: International Workshop2011. p. 2-4.

[288] Zhang H, Che F, Lin T, Zhao W. Modeling, Analysis, Design, and Tests for Electronics Packaging Beyond Moore: Woodhead Publishing; 2019.

[289] Zimnoch M, Oliferuk W, Maj M. Estimation of defect depth in steel plate using lock-in IR thermography. acta mechanica et automatica. 2010;4:106-9.

[290] Tian GY, Gao Y, Li K, Wang Y, Gao B, He Y. Eddy current pulsed thermography with different excitation configurations for metallic material and defect characterization. Sensors. 2016;16:843.

[291] Gao Y, Tian GY, Wang P, Wang H, Gao B, Woo WL, et al. Electromagnetic pulsed thermography for natural cracks inspection. Scientific reports. 2017;7:42073.

[292] Lin Y, Gigliotti M, Lafarie-Frenot MC, Bai J, Marchand D, Mellier D. Experimental study to assess the effect of carbon nanotube addition on the through-thickness electrical conductivity of CFRP laminates for aircraft applications. Composites Part B: Engineering. 2015;76:31-7.

[293] Selvakumaran L, Lubineau G. Electrical behavior of laminated composites with intralaminar degradation: a comprehensive micro-meso homogenization procedure. Composite Structures. 2014;109:178-88.

[294] Barakati A, Zhupanska O. Mechanical response of electrically conductive laminated composite plates in the presence of an electromagnetic field. Composite Structures. 2014;113:298-307.

[295] Prémel D, Granet G. Development of the curvilinear coordinate method for the computation of quasi-static fields induced by an eddy current probe scanning a 3D conductor of complex shape characterized by an arbitrary 2D surface. International Journal of Numerical Modelling: Electronic Networks, Devices and Fields. 2018;31:e2219.

[296] Prémel D, Granet G. Fast computation of the response of any 3D Eddy Current probe scanning a 3D stratified conductor characterized by a set of arbitrary interfaces of complex shape. International Journal of Applied Electromagnetics and Mechanics. 2019:1-7.

[297] CHEBBI H, PRÉMEL D. Semi-analytical modeling of eddy current inspection of stratified and homogenized composite materials.

[298] Wasselynck G, Trichet D, Fouladgar J. Determination of the electrical conductivity tensor of a CFRP composite using a 3-D percolation model. IEEE Transactions on Magnetics. 2013;49:1825-8.

[299] Arora V, Siddiqui JA, Mulaveesala R, Muniyappa A. Pulse compression approach to nonstationary infrared thermal wave imaging for nondestructive testing of carbon fiber reinforced polymers. IEEE Sensors Journal. 2015;15:663-4.

[300] Laureti S, Silipigni G, Senni L, Tomasello R, Burrascano P, Ricci M. Comparative study between linear and non-linear frequency-modulated pulse-compression thermography. Applied optics. 2018;57:D32-D9.

[301] Laureti S, Sfarra S, Malekmohammadi H, Burrascano P, Hutchins D, Senni L, et al. The use of pulse-compression thermography for detecting defects in paintings. Ndt & E International. 2018;98:147-54.

[302] Hutchins D, Burrascano P, Davis L, Laureti S, Ricci M. Coded waveforms for optimised air-coupled ultrasonic nondestructive evaluation. Ultrasonics. 2014;54:1745-59.

[303] Hughes R, Drinkwater B, Smith R. Characterisation of carbon fibre-reinforced polymer composites through radon-transform analysis of complex eddy-current data. Composites Part B: Engineering. 2018;148:252-9.

[304] Mouritz A, Leong K, Herszberg I. A review of the effect of stitching on the in-plane mechanical properties of fibre-reinforced polymer composites. Composites Part A: applied science and manufacturing. 1997;28:979-91.

[305] Silipigni G, Burrascano P, Hutchins DA, Laureti S, Petrucci R, Senni L, et al. Optimisation of the pulse-compression technique applied to the infrared thermography nondestructive evaluation. NDT & E International. 2017;87:100-10.

[306] Ding S, Tian G, Dobmann G, Wang P. Analysis of domain wall dynamics based on skewness of magnetic Barkhausen noise for applied stress determination. Journal of Magnetism and Magnetic Materials. 2017;421:225-9.

[307] Subhani S, Suresh B, Ghali V. Empirical mode decomposition approach for defect detection in non-stationary thermal wave imaging. Ndt & E International. 2016;81:39-45.

[308] Cheng L. Eddy current pulsed thermography for non-destructive evaluation of carbon fibre reinforced plastic for wind turbine blades: Newcastle University; 2013.

[309] Lopez F, Ibarra-Castanedo C, de Paulo Nicolau V, Maldague X. Optimisation of pulsed thermography inspection by partial least-squares regression. NDT & E International. 2014;66:128-38.

[310] Yılmaz B, Jasiūnienė E. Advanced ultrasonic NDT for weak bond detection in composite-adhesive bonded structures. International Journal of Adhesion and Adhesives. 2020;102:102675.

[311] Yin A, Gao B, Yun Tian G, Woo W, Li K. Physical interpretation and separation of eddy current pulsed thermography. Journal of applied physics. 2013;113:064101.

[312] Ishikawa M, Hatta H, Habuka Y, Fukui R, Utsunomiya S. Detecting deeper defects using pulse phase thermography. Infrared Physics & Technology. 2013;57:42-9.

[313] Laureti S, Malekmohammadi H, Rizwan MK, Burrascano P, Sfarra S, Mostacci M, et al. Looking Through Paintings by Combining Hyper-Spectral Imaging and Pulse-Compression Thermography. Sensors. 2019;19:4335.

[314] Yi Q, Malekmohammadi H, Tian GY, Laureti S, Ricci M. Quantitative Evaluation of Crack Depths on Thin Aluminum Plate using Eddy Current Pulse-Compression Thermography. IEEE Transactions on Industrial Informatics. 2019.

[315] Ding S, Tian G, Sutthaweekul R. Non-destructive hardness prediction for 18CrNiMo7-6 steel based on feature selection and fusion of Magnetic Barkhausen Noise. NDT & E International. 2019;107:102138.